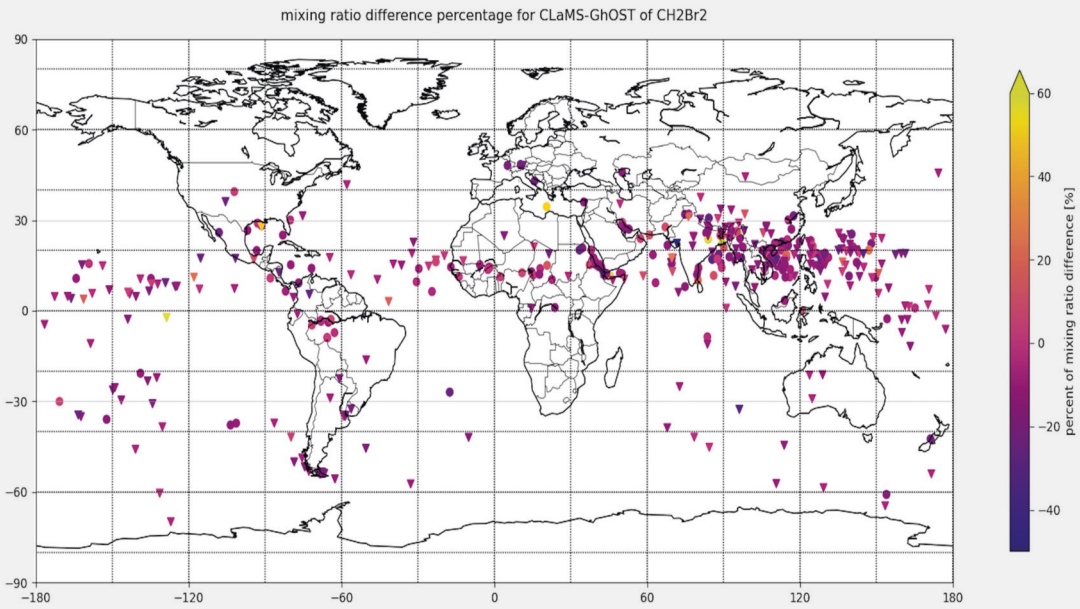

Investigation of Lower Boundary Conditions of Brominated Very Short-lived Species (VSLS)

Siyuan Zheng

Energie & Umwelt / Energy & Environment
Band / Volume 637
ISBN 978-3-95806-770-7

Mitglied der Helmholtz-Gemeinschaft

JÜLICH
Forschungszentrum

Schriften des Forschungszentrums Jülich
Reihe Energie & Umwelt / Energy & Environment Band / Volume 637

Forschungszentrum Jülich GmbH
Institut für Energie- und Klimaforschung (IEK)
Stratosphäre (IEK-7)

Investigation of Lower Boundary Conditions of Brominated Very Short-lived Species (VSLS)

Siyuan Zheng

Schriften des Forschungszentrums Jülich
Reihe Energie & Umwelt / Energy & Environment Band / Volume 637

ISSN 1866-1793 ISBN 978-3-95806-770-7

Bibliografische Information der Deutschen Nationalbibliothek.
Die Deutsche Nationalbibliothek verzeichnet diese Publikation in der Deutschen Nationalbibliografie; detaillierte Bibliografische Daten sind im Internet über http://dnb.d-nb.de abrufbar.

Herausgeber und Vertrieb:	Forschungszentrum Jülich GmbH Zentralbibliothek, Verlag 52425 Jülich Tel.: +49 2461 61-5368 Fax: +49 2461 61-6103 zb-publikation@fz-juelich.de www.fz-juelich.de/zb
Umschlaggestaltung:	Grafische Medien, Forschungszentrum Jülich GmbH
Druck:	Grafische Medien, Forschungszentrum Jülich GmbH
Copyright:	Forschungszentrum Jülich 2024

Schriften des Forschungszentrums Jülich
Reihe Energie & Umwelt / Energy & Environment, Band / Volume 637

D 468 (Diss. Wuppertal, Univ., 2024)

ISSN 1866-1793
ISBN 978-3-95806-770-7

Vollständig frei verfügbar über das Publikationsportal des Forschungszentrums Jülich (JuSER) unter www.fz-juelich.de/zb/openaccess.

This is an Open Access publication distributed under the terms of the Creative Commons Attribution License 4.0, which permits unrestricted use, distribution, and reproduction in any medium, provided the original work is properly cited.

Abstract

Photochemical reactions with the reactive halogen atoms Cl and Br mostly cause stratospheric ozone depletion. The chlorine- and bromine-containing very short-lived species (VSLS), which have an atmospheric lifetime of less than six months, play an essential role in stratospheric total bromine loading. However, there is considerable uncertainty about the geographical distribution of their sources, and therefore, it is challenging to reproduce the observations. In order to describe the stratospheric or regional abundance of bromine from VSLS, it is of great importance to quantify the lower boundary conditions of these species.

In order to increase our understanding of the role of brominated species in the stratosphere, the Chemical Lagrangian Model of the Stratosphere (CLaMS) has been used to investigate the global surface mixing ratio and lower boundary conditions for the simulation in this thesis. The simulation uses a 'top-down' approach, where atmospheric measurements from aircraft are used in combination with models to quantify and refine the lower boundary emissions. Firstly, for the representation of tropospheric bromine chemistry, the scheme incorporates bromine-containing species and related chemical decomposition reactions into CLaMS, which include photolysis and reactions with Cl, $O(^1D)$, and OH. Using a box model, this chemistry scheme was successfully tested and transferred to the more comprehensive global 3D chemical transport model, MESSy-CLaMS. Secondly, for the representation of tropospheric bromine chemistry, a parameterization for the washout of the inorganic bromine species HBr and HOBr in the troposphere by cloud uptake was incorporated. To enhance the representation of the transport scheme, additional tropospheric mixing and vertical transport by convection were adopted employing the MESSy-CLaMS 2.0 version. Finally, to investigate the lower boundary conditions of the two most significant bromine VSLS, $CHBr_3$ and CH_2Br_2, the CLaMS model constructed the zonal symmetric seasonal dependent lower boundary, the seasonal and monthly dependent regionally resolved lower boundary map. The simulation results and

observations from the HALO aircraft of the SouthTRAC campaign were compared in detail to assess the reliability of the lower boundary conditions.

The findings of this thesis reveal that the simulation incorporating a monthly global lower boundary, featuring notable seasonal and zonal variations, exhibits enhanced concordance with observations obtained during the SouthTRAC campaign. However, the elevated mixing ratio of $CHBr_3$ and CH_2Br_2 in the upper atmosphere was not confirmed by climatological upper tropospheric and stratospheric data, presumably due to slow upward transport. Moreover, the exceedingly high values detected in specific regions at the estimated lower boundary are likely attributed to the limited available observations from the SouthTRAC campaign. This underscores the necessity for additional observations during spring and summer, as well as observation data from higher latitudes in the Northern Hemisphere, to comprehensively construct the lower boundary distribution of $CHBr_3$ and CH_2Br_2.

Contents

1 Motivation **1**

2 Introduction **7**

2.1 Structure of atmosphere 7

2.2 Upper troposphere and lower stratosphere (UTLS) 10

2.2.1 Transport in the tropical tropopause layer (TTL) 11

2.2.2 Tracer-tracer correlations 13

2.3 Bromine very short-lived species (VSLS) 14

2.3.1 Source of bromine-containing VSLSs 16

2.3.2 Brominated VSLS loading in the stratosphere 20

3 Data and method **25**

3.1 Chemical Lagrangian Model of the Stratosphere (CLaMS) 26

3.1.1 CLaMS model version 1.0 26

3.1.2 CLaMS model version 2.0 29

3.2 Observational data 30

3.2.1 Southern Hemisphere Transport, Dynamics, and Chemistry (South-TRAC) data 30

3.2.2 A climatology of brominated species 31

4 Preparation of the global simulation with VSLS chemistry **33**

4.1 Incorporation of bromine-containing species and reactions 33

4.2 Classical CLaMS box model simulation 35

4.3 Transfer to MESSy-CLaMS 39
4.4 Global 3D MESSy-CLaMS 40

5 Incorporation of scavenging parameterization and additional convection processes 43
5.1 HBr and HOBr scavenging 44
5.2 MESSy-CLaMS 2.0 48

6 Optimization of the VSLS lower boundary 60
6.1 Zonally symmetric boundary with seasonal dependence 60
6.1.1 Investigation using surface origin tracers 68
6.1.2 Age of air selection 73
6.2 Regionally resolved boundary with seasonal dependence 78
6.2.1 Backward trajectory analysis including convection 81
6.2.2 Construction of a regionally resolved boundary 86
6.3 Regionally resolved boundary with monthly dependence 95

7 Summary and outlook 108

List of figures 111

List of tables 115

List of abbreviations 116

Bibliography 118

A Incorporated washout reactions 134

B Surface origin tracers contribution in MESSy CLaMS 1.0 135

C Seasonal lower boundary map adapted from climatology 137

D Distribution of air parcels at lower boundary in different months 141

E Monthly dependent regionally resolved lower boundary maps 147

F Comparison with altitude-latitude cross section between climatology data and simulation with a zonally symmetric seasonal lower boundary 156

Chapter 1

Motivation

It is known that stratospheric ozone plays a critical role in the Earth system as it affects human health and the global ecosystem. Consequently, the depletion of the ozone layer, particularly in polar regions (e.g., the ozone hole), has generated significant concerns over the last few decades (Solomon, 1999; Barnes et al., 2019; Langematz, 2019; Engel et al., 2019). The changes of stratospheric ozone, first observed in the 1980s, alter the solar ultraviolet (UV) radiation conditions on the surface and change the global climate system (includes both the temperature distribution and the circulation) (Barnes et al., 2019, 2022; Polvani et al., 2020).

For example, the poleward shift of the jet stream, coupled with the expansion of the tropics and the Southern Hemisphere's storm tracks due to the Antarctic ozone hole, has led to significant changes to the midsummer surface climate (Gillett and Thompson, 2003; Laube et al., 2022). Ozone is destroyed by catalytic chemical processes that involve reactive gases containing hydrogen and nitrogen, as well as chlorine and bromine compounds, which are known as ozone-depleting substances (ODS) (Langematz, 2019). Their chemical and dynamic transport processes in the atmosphere mainly control the spatial and temporal distribution of stratospheric ozone.

The long-lived human-produced halogen-containing ODS (lifetime longer than six months), such as halons, chlorofluorocarbons (CFCs), carbon tetrachloride (CCl_4), methyl bromide (CH_3Br), methyl chloroform (CH_3CCl_3) and hydrochlorofluorocarbons (HCFCs),

are typically well mixed in the troposphere. These compounds were effectively controlled and eliminated mainly through the 'Montreal Protocol on Substances that Deplete the Ozone Layer', which was signed in 1987 and underwent periodic adjustments and amendments every few years (the most recent being the Kigali Amendment in 2016), resulting in a successful reduction in the global anthropogenic emissions of these substances (Engel et al., 2019). In recent decades, the focus has turned to ODS with very short lifetimes (local lifetimes of no more than six months), including both organic and inorganic halogenated source gases (SGs) as well as product gases (PGs), which have significantly contributed to global halogen loading and ozone depletion (Hossaini et al., 2019; Dowdell et al., 1994; Koenig et al., 2020; Saiz-Lopez et al., 2015). These halogen-containing VSLS also release highly reactive halogen radicals—chlorine (Cl) and bromine (Br)—and are not subject to control under the Montreal Protocol.

Brominated VSLSs, which are several times more efficient in destroying ozone than chlorinated VSLSs, contribute to both the stratospheric bromine budget and global ozone depletion (Engel et al., 2019; Aschmann and Sinnhuber, 2013). The brominated VSLSs, which include bromoform ($CHBr_3$), dibromomethane (CH_2Br_2), and further polyhalogenated VSLS: bromo-chloromethane (CH_2BrCl), dibromo-chloromethane ($CHBr_2Cl$) and bromo-dichloromethane ($CHBrCl_2$), are predominantly naturally-emitted and they potentially carry a relatively substantial amount of reactive bromine into the stratosphere (Hossaini et al., 2012; Brinckmann et al., 2012; Warwick et al., 2006). However, due to their very short lifetime, high temporal and geographical variability, and the absence of enough seasonal and spatial coverage of observational data, constraining the magnitude and distribution of these bromine VSLS emissions inventories is challenging (Laube et al., 2022). In this case, numerous studies have conducted research on the global geographical distribution maps of the halogenated VSLS for different seasons and different hemispheres, also for different evaluation of emission scenarios (Pisso et al., 2010; Brioude et al., 2010).

Excluding methyl bromide (CH_3Br), the most abundant bromine-containing VSLS are CH_2Br_2 and $CHBr_3$, which together contribute relatively large amounts of bromine to the

stratosphere (Hossaini et al., 2010; Carpenter, 2014). In previous studies, various brominated VSLS emission sources and inventory distributions have been explored through 'top-down' approaches, which utilize atmospheric measurements with models to quantify and refine surface source distributions, and 'bottom-up' methodologies, where the surface source conditions are estimated by considering all recognized sources and offering a best-estimated calculation for their emissions (Warwick et al., 2006; Aschmann, 2009; Ordóñez et al., 2012; Ziska et al., 2013). For example, utilizing the CAM-Chem model, Ordóñez demonstrates the seasonal and spatial distribution of global oceanic emissions, with weighted VSLS emissions in tropical regions, constant oceanic fluxes over the ocean, higher emission fluxes in coastal areas and no fluxes at high latitudes where the sea-ice interface is located (Ordóñez et al., 2012). Ziska et al. (2013) estimated the global climatological flux between ocean and atmosphere based on the calculated global concentration maps of the surface ocean and atmosphere using the 'bottom-up' methodology.

Considering the very short lifetime of the brominated VSLS, the estimation of lower boundary mixing ratios using the 'bottom-up' method through reconciled combined data from diverse activities by individual regions and time introduces uncertainty, and potentially leads to inaccuracies in specific areas. Conversely, the top-down approach for brominated VSLS relies on modeling and comparing them with measured atmospheric mixing ratios, the uncertainties of which stem from the geographical scope of the available measurements. The simulations in this thesis employ the three-dimensional (3D) Chemistry Lagrangian Model of the Stratosphere (CLaMS) and observational data from the GhOST experiment. The experiment was operated by the University of Frankfurt and involved measurements collected aboard the HALO aircraft during the SouthTRAC campaign in South America. The CLaMS simulations follow the 'top-down' principle, employing lower boundary conditions in mixing ratios over different time scales. The lower boundary condition used in the CLaMS model is the initial state of the surface distribution of the different species sources. The refinement of the lower boundary estimation was achieved by incorporating surface origin tracers (Section 6.1.1) and conducting back-

trajectory calculations, which involved multiple adjustments.

Given that the lower boundary conditions establish the initial state of various species at the surface and exert a significant impact on the atmospheric composition via chemical and transport processes, they play a critical role in interpreting observations, ensuring accurate forecasts, and simulating atmospheric behavior. The objective of this thesis is to attribute and enhance the comprehension of the global lower boundary distributions of brominated VSLS. Therefore

• First, an extended chemistry scheme, including $CHBr_3$, CH_2Br_2,CH_3Br, CH_2BrCl, $CHBr_2Cl$, $CHBrCl_2$, H1211, H2402 and H1301, has been incorporated and verified in the CLaMS model.

• Further, the simulations of CLaMS 2.0 with additional tropospheric mixing and vertical convection also incorporated the inorganic bromine (HBr and HOBr) sink parameterization.

• Then, the seasonal dependent zonally symmetric lower boundary conditions in mixing ratios were derived from climatology data.

• Based on these results and the assessment of the campaign data, the updated global seasonal and monthly dependent regionally resolved lower boundary is determined.

This thesis consists of six chapters. The introduction part in Chapter 2 shows the scientific background of the research, including the atmospheric structure and dynamics in the upper troposphere and lower stratosphere (UTLS). Furthermore, the source and loading of the brominated VSLSs are explained in detail. Chapter 3 introduces our modeling setup and the observational data. Chapter 4 focuses on the initialization of simulation, which includes the incorporation of bromine species and related reactions, the box model test, and the first 3D simulation in MESSy-CLaMS. Chapter 5 explains the parameterization for the washout of the inorganic bromine HBr and HOBr, and the new updated model version MESSy-CLaMS 2.0 is introduced. In Chapter 6, three lower boundary conditions at different time and spatial scales are compared in the simulation and the simulated atmospheric mixing ratios are validated with observational and climatological data. Finally,

the results are summarized in Chapter 7.

Chapter 2

Introduction

This chapter introduces the scientific background of the atmosphere. It describes the dynamic processes in the upper troposphere and lower stratosphere (UTLS) and the trace gas correlations used in this study. The source and loading of brominated very short-lived species (VSLS) are also described.

2.1 Structure of atmosphere

The atmosphere is a complex and interconnected system that is composed of various trace gases and aerosols. Its composition and dynamics are essential to the Earth's ecosystem and the basis of life. The atmosphere protects all the life on Earth by providing oxygen for breathing, preventing intense ultraviolet (UV) radiation, containing warmth for the Earth, and lessening the extreme variation of temperature on different spatial and temporal scales. The chemical composition of the atmosphere, along with many necessary physical, chemical, and biochemical processes can influence atmospheric behavior and subsequently impact the Earth system.

The primary composition of Earth's atmosphere consists of molecular nitrogen (N_2) and oxygen (O_2), which account for 78% and 21% by volume, respectively. Other relatively minor components, including argon (Ar), water vapor (H_2O), carbon dioxide (CO_2), ozone (O_3), and other constituents incorporate the remaining 1% of the atmosphere. These H_2O, CO_2 and O_3 exhibit high variability over different time and spaces. Despite

their small proportion, species like H_2O and O_3 play a significant role in retaining the equilibrium of energy on Earth by affecting the radiation process (Salby, 1996).

With increasing altitude, the atmosphere includes the troposphere, stratosphere, mesosphere, thermosphere, and exosphere as depicted in Figure 2.1. Among these layers, the troposphere and stratosphere are the two most relevant for brominated VSLS, each with different temperature gradients and specific phenomena.

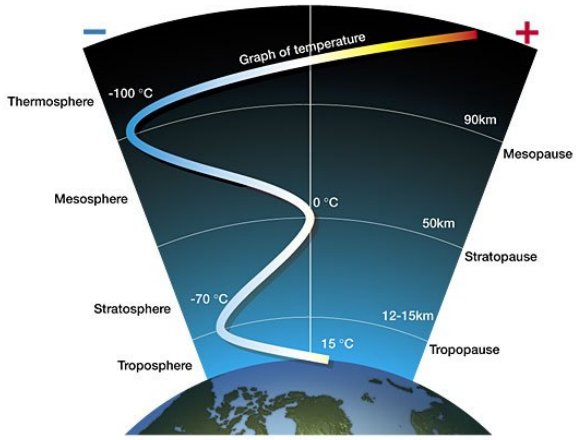

Figure 2.1: Five basic layers of atmosphere according to temperature changes (Sinha, 2023).

The troposphere is closest to the ground, and its thickness varies with latitude and season. The mean thickness of this layer is about 8-9 km in high-latitude regions, 10-12 km in mid-latitude areas, and reaches 17-18 km across low-latitude zones. The boundary layer in the lower troposphere is where the heat, mass, and momentum exchange occurs between the Earth's surface and the atmosphere. Lower boundary conditions usually serve as input to the atmospheric model, and may be formulated in two different ways, either as emission flux or as mixing ratios. The emission flux of gases represents emissions per unit area emitted into the atmosphere from surface sources. It is worth noting that in this thesis, the lower boundary in the CLaMS model is set as a mixing ratio, which describes the concentration distribution of these gases on the surface. The surface emit-

ted gases include natural/biogenic sources and anthropogenic emissions originating from surface transport to the upper troposphere and stratosphere, thereby participating in the global atmospheric circulation. The comprehensive process of transport encompasses the gases released from the surface and removed from the atmosphere. The troposphere employs three primary mechanisms to remove these contaminants: dry deposition, wet deposition, and chemical reactions. A wet deposition involves two processes for reducing aerosols and trace gases: rainout, characterized by the condensation of cloud droplets (in-cloud scavenging), and washout (below-cloud scavenging), which is the removal of substances by water particles beneath the cloud (Tang et al., 2006; Mohanakumar, 2008; Dépée et al., 2019; Kajino and Aikawa, 2015).

The boundary between the troposphere and stratosphere is known as the 'tropopause'. The region near the tropopause plays a crucial role in atmospheric transport, as halogenated compounds can be lifted here via deep convection before ultimately entering the stratosphere (Sinnhuber and Folkins, 2006). Despite the rarity of weather events, the region near tropopause has strong interactions between radiative, dynamic, and chemical processes (Mohanakumar, 2008). Above lies the atmosphere's subsequent prominent layer, the stratosphere, which extends beyond the tropopause to altitudes of about 50 km (1 hpa). The stratosphere is characterized by stable atmospheric conditions, while below is the troposphere, where turbulence is prevalent. The predominant factor affecting the temperature in the stratosphere is ozone (O_3), which originates from the photolytic decomposition of oxygen (O_2) molecules through exposure to solar ultraviolet (UV) radiation, followed by the subsequent bonding of a free oxygen atom with another O_2 molecule. Essential functions of the stratospheric ozone layer include absorbing and blocking ultraviolet (UV) radiation from reaching the Earth's surface and converting solar energy into heat. Ozone is catalytically destroyed in the stratosphere mainly through nitrogen oxides (NO_x) and hydroxides (HO_x) chemistry. Nonetheless, naturally occurring compounds such as chloroform ($CHCl_3$) and bromoform ($CHBr_3$), along with anthropogenic halogen compounds like chlorofluorocarbons (CFCs) and brominated halons, potentially release active chlorine and bromine atoms, serving as catalysts for the reduc-

tion of ozone in the upper stratosphere. The efficient catalytic chemical process involving bromine and chlorine within the stratospheric ozone layer has led to ozone depletion, exemplified by the formation of the Antarctic ozone hole (Farman et al., 1985). Most of the halogen-containing ozone-depleting substances (ODS) are controlled by the 'Montreal Protocol' and the following amendments, leading to the recovery of ozone in recent years (e.g. Chipperfield et al., 2017). However, there is growing concern about the increasing levels of short-lived halogen-containing species, which contribute to stratospheric ozone depletion and are not covered by the 'Montreal Protocol'.

2.2 Upper troposphere and lower stratosphere (UTLS)

The upper troposphere and lower stratosphere (UTLS) represent a critical atmospheric coupling layer where air and atmospheric components undergo exchange between the troposphere and the stratosphere. The bi-directional exchange across the tropopause between the troposphere and the stratosphere significantly influences the chemistry of both regions. Notably, the UTLS, situated beneath the ozone layer, exhibits the coldest air temperatures within the lower atmosphere, and aircraft observations are usually sampled in this region. The intricate characteristics of this region emerge from the interplay of dynamics, radiation, chemistry and microphysics. The chemical composition of UTLS is influenced by the emissions in the lower boundary layer and the subsequent atmospheric transport mechanisms. As highlighted by Riese et al. (2012), changes in thermal structure and chemical composition within this region significantly impact the global radiative balance and are crucial to the climate system. For example, the bromine released from very short-lived substances (VSLSs) in the lowermost stratosphere region could affect ozone abundance and distribution, leading to notable changes in radiative effects (Hossaini et al., 2015; Jesswein et al., 2022).

2.2.1 Transport in the tropical tropopause layer (TTL)

It is acknowledged that the majority of atmospheric air is transported from the surface to the stratosphere and then moves poleward through tropical regions via a variety of transport pathways (Holton et al., 1995; Mohanakumar, 2008). Therefore, the tropical tropopause layer (TTL), constituting the transition region between the troposphere and stratosphere in the tropics, plays a crucial role as the gateway to the stratosphere. This region is crucial for maintaining radiative balance, transferring energy from the troposphere to the stratosphere, and facilitating chemical exchanges of water vapor, ozone, and other atmospheric trace gases, such as very short-lived substances (VSLSs) (Fueglistaler et al., 2009).

The tropical tropopause layer has an upper boundary around 18.5 km, 70 hPa and a lower limit of 14 km, 150 hPa. It is horizontally constrained by the underlying subtropical jets, as illustrated in Figure 2.2 (Fueglistaler et al., 2009). Within the TTL, predominant transport processes encompass large-scale vertical motion, deep convection, some small-scale vertical mixing, descent, as well as horizontal advection. This region plays a crucial role as the primary transport pathway for gases to reach the lower stratosphere. For example, the VSLSs, whose decomposition matches the timescales of the high-reaching convection and ascent process in this region, are transported into the stratosphere through the TTL region (Gettelman et al., 2009). These transport mechanisms can determine the climatological structure and annual variability of the TTL, and the chemical composition of the atmosphere (Poshyvailo, 2020; Gettelman and Birner, 2007).

As shown in Figure 2.2, the air transport from the upper troposphere (10.5 km) to the tropical tropopause layer (TTL) is mainly by large-scale updrafts, which are dominated by outflows around 200 hPa and rapidly decay in the TTL region with increasing height. Several of them could enter into the TTL region and cross the level of zero clear sky radiative heating (Q=0). Air from the lower troposphere can be transported fast to the middle-upper troposphere at around 10 km, and then above 10 km, air gently ascents upward into the stratosphere mainly driven by diabatic heating (Narayana Rao et al.,

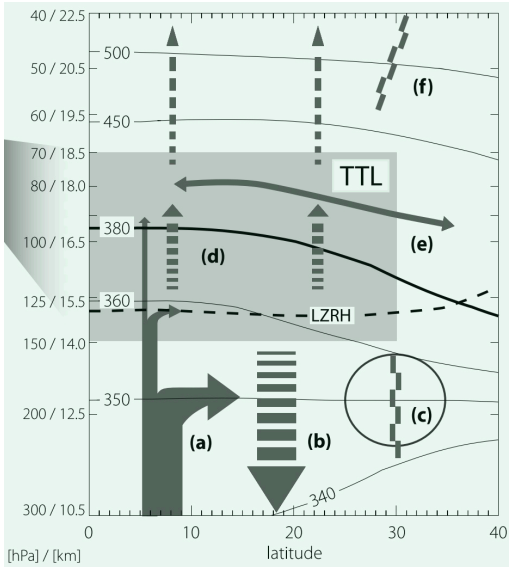

Figure 2.2: Tropical tropopause layer's dynamics transport process. The arrow shows the circulation; letter **a** means the vertical convection and letter **b** is the radiative cooling. The letter **c** indicates the subtropical jets, as the transport barrier between the troposphere and stratosphere. The letter **d** demonstrates radiative heating, and the letter **e** is the rapid meridional transport of tracers and mixing. The letter **f** indicates the edge of the 'tropical pipe' (Fueglistaler et al., 2009).

2008). This vertical transport of tropospheric air across the TTL region can affect the stratospheric chemistry (such as the concentration of water vapor and very short-lived substances (VSLS)) (Ploeger et al., 2010).

Overshooting deep convection has the ability to directly transport air rapidly to the lower stratosphere, effectively change the composition of trace gases, and mix air from the upper boundary layer and stratospheric downdraft in the TTL (Frey et al., 2015). Another way for air to reach the lower stratosphere is through quasi-isotropic advective transport between TTL and mid-latitudes, where air crosses the subtropical jet barrier, which has its highest permeability during the monsoon circulation (Vogel et al., 2015). In addition, the subtropical jet stream can also function as an efficient transport barrier for meridional transport, which can redistribute trace gases at middle and high latitudes, with the southern hemisphere typically having a stronger transport barrier than the northern hemisphere during the same season (Holton et al., 1995; Haynes and Shuckburgh,

2000; Konopka et al., 2007). The pronounced influence of deep convection and isentropic mixing from the mid-latitude lowermost stratosphere on the Tropical Tropopause Layer (TTL) strongly affects the concentration of trace gases entering the stratosphere, thereby impacting the radiative balance (heating or cooling) of the TTL (Sargent et al., 2014). Tropospheric convection and stratospheric circulation can determine the vertical exchange between the troposphere and the stratosphere. The trace gases, including water vapor, ozone, carbon dioxide, and very short-lived substances, can be carried into the stratosphere and contribute significantly to the radiative balance of the TTL. This, in turn, controls the strength and direction of the upward motion within this critical atmospheric layer (Gettelman et al., 2004).

Regarding the brominated and chlorinated VSLSs, the transport from the surface to the stratosphere includes two main pathways. On very short timescales, the deep convection lifts the trace gases towards the TTL region and then transports them to the stratosphere. On a longer timescale, the Brewer-Dobson circulation (BDC), which is a global slow circulation pattern driven by stratospheric wave drag, slowly moves the tropospheric air upward through the TTL. In the stratosphere, the BDC is directed upward and poleward, and air masses sink at the middle and high latitudes (Holton et al., 1995; Mohanakumar, 2008). The amount of these trace gases that enter the stratosphere varies according to changes in the stratospheric circulation, the annual cycle of TTL temperature, and strong convective activities (Aschmann et al., 2011; Mohanakumar, 2008).

2.2.2 Tracer-tracer correlations

The most abundant trace gases in the stratosphere and troposphere mainly include water vapor (H_2O), ozone (O_3), methane (CH_4), and carbon dioxide (CO_2). The abundance of these trace gases varies with altitude throughout the stratosphere, with observed mixing ratios in parts per million by volume (ppmv) (Grooß and Russell, 2005). The trace gases used by the tracer-tracer correlation method have different photochemical lifetimes in the atmosphere, but in some cases they show similar behaviour. Notably, the mixing ratios derived from observations often show a compact relationship, enabling the mea-

sured concentration of one to predict the concentration of the other, which is a technique called the tracer-tracer correlation method. The tracer-tracer correlation techniques have been widely used, particularly in estimating chemical O_3 loss from the observational data (Tilmes et al., 2004; Müller et al., 1997). For the ozone-tracer correlation techniques, tracers like CH_4, HF and N_2O were used as long-lived tracers, and considered O_3 as the short-lived compounds. For example, Hegglin and Shepherd (2007) reviewed the characteristics of diabatic descent and horizontal mixing using the seasonal cycle of the O_3-N_2O correlations in the stratosphere, as well as for polar ozone loss in different altitudes and hemispheres. This method was also applied to the chemistry-climate model (CCM) to investigate the effects of internal mixing and mixing over the vortex edge on chemical ozone loss (Lemmen et al., 2006). In addition, the tracer-tracer correlation method can also be used to quantify the dynamic process in the atmosphere. For example, using correlations between the tropospheric tracer CO and stratospheric tracer O_3, Hoor et al. (2002) discovered that the lowest stratospheric mixed layer exhibits significant seasonal variations. The correlations between O_3 and H_2O can also be used to distinguish the tropical tropopause transition layer from the surrounding stratosphere and troposphere (Pan et al., 2014). In this thesis, the correlation between N_2O and short-lived bromine-containing species are used to obtain the initialization and lower boundary mixing values for brominated VSLSs model simulation.

2.3 Bromine very short-lived species (VSLS)

Ozone-depleting substances (ODSs), particularly chlorine- and bromine-containing gases, when present in the stratosphere can transform into reactive halogen gases. The reactive halogen gases can react to form chlorine monoxide (ClO), bromine monoxide (BrO), as well as chlorine and bromine atoms (Cl and Br). These exceptionally reactive halogen atoms participate in catalytic ozone-depleting reactions, contributing to the efficient destruction of ozone.

Throughout the stratosphere, the catalytic ozone depletion cycles encompass multiple independent reactions. The atoms Cl or Br serve as catalysts, as shown in equation

2.1, initially engaging with O_3 to produce O_2 and ClO or BrO. Subsequently, ClO or BrO can further react with O to regenerate Cl or Br along with O_2. Furthermore, in the late winter and early spring of the polar regions, as shown in equation 2.2, ClO may react with another ClO or with BrO and, when exposed to sunlight, break apart, yielding Br and Cl gases. These Br and Cl product gases again play a crucial role in the destruction of O_3. Since the Br and Cl continually react and regenerate during each completion of the reaction cycle, a single Br and Cl atom can destroy a substantial number of ozone molecules, underscoring that even a small quantity of reactive halogen gases has a significant impact on the ozone layer.

$$\begin{aligned} \mathrm{Cl} + \mathrm{O_3} &\rightarrow \mathrm{ClO} + \mathrm{O_2} \qquad & \mathrm{Br} + \mathrm{O_3} &\rightarrow \mathrm{BrO} + \mathrm{O_2} \\ \mathrm{ClO} + \mathrm{O} &\rightarrow \mathrm{Cl} + \mathrm{O_2} \qquad & \mathrm{BrO} + \mathrm{O} &\rightarrow \mathrm{Br} + \mathrm{O_2} \end{aligned} \tag{2.1}$$

$$\begin{aligned} \mathrm{ClO} + \mathrm{ClO} &\rightarrow (\mathrm{ClO})_2 \qquad & \mathrm{ClO} + \mathrm{BrO} &\rightarrow \mathrm{Cl} + \mathrm{Br} + \mathrm{O_2} \\ (\mathrm{ClO})_2 + \mathrm{sunlight} &\rightarrow \mathrm{ClOO} + \mathrm{Cl} \qquad & \mathrm{ClO} + \mathrm{BrO} &\rightarrow \mathrm{BrCl} + \mathrm{O_2} \\ \mathrm{ClOO} &\rightarrow \mathrm{Cl} + \mathrm{O_2} \qquad & \mathrm{BrCl} + \mathrm{sunlight} &\rightarrow \mathrm{Br} + \mathrm{Cl} \\ 2(\mathrm{Cl} + \mathrm{O_3} &\rightarrow \mathrm{ClO} + \mathrm{O_2}) \qquad & \mathrm{Cl} + \mathrm{O_3} &\rightarrow \mathrm{ClO} + \mathrm{O_2} \\ & & \mathrm{Br} + \mathrm{O_3} &\rightarrow \mathrm{BrO} + \mathrm{O_2} \end{aligned} \tag{2.2}$$

In addition to the well-known long-lived substances such as chlorofluorocarbons (CFCs), hydrochlorofluorocarbons (HCFCs), and halons, there is a growing interest in halogen-containing very short-lived substances (VSLS), which were not regulated by the Montreal Protocol (Laube et al., 2008; Rhew, 2011; Falk et al., 2017). VSLS are defined as trace gases with a local lifetime of less than six months and are primarily composed of brominated, chlorinated, and iodinated species. It's important to note that bromine, in particular, is significantly more efficient than chlorine in catalyzing the global total ozone loss cycle in the stratosphere, by a factor of over 60 times. This means even less abundant bromine plays a substantial role in the chemistry of the global ozone layer (Hossaini et al.,

2012). This section concentrates on the very short-lived bromine species associated with their natural and anthropogenic emission sources as well as the processes involved in regulating their concentrations in the stratosphere.

2.3.1 Source of bromine-containing VSLSs

The brominated species contributing to stratospheric ozone depletion include the long-lived ozone-depleting substances (ODSs) and the very short-lived substances (VSLSs). As shown in Figure 2.3, the long-lived brominated ODSs, including halons and CH_3Br, have largely anthropogenic sources from their past accumulated emissions and current by-product formation, and just a small portion of CH_3Br originates naturally from oceanic and terrestrial ecosystems. The brominated very short-lived substances (VSLSs) include dibromomethane (CH_2Br_2), bromoform ($CHBr_3$), as well as three polyhalogenated species: bromochloromethane (CH_2BrCl), dibromochloromethane ($CHBr_2Cl$), and dichlorobromomethane ($CHBrCl_2$). These compounds, originating from both natural and human sources, are predominantly generated through oceanic emissions, with smaller anthropogenic contributions stemming from coastal power plants and ships (Laube et al., 2022). For example, the anthropogenic sources from water-related disinfection contribute a minor fraction to total bromine (the concentration of all bromine summed up by bromine-containing species according to their bromine atoms) on global scales (Quack and Wallace, 2003), and therefore not be considered here. The natural ocean emission of bromine VSLS is primarily produced by algae and phytoplankton. Of course, due to different species of macroalgae and varying chemical processes, the source regions of the various VSLSs may not be exactly the same. For example, the tropical ocean, which includes macroalgae and phytoplanktons, might be the dominant source for CH_2Br_2 (Yokouchi et al., 2018).

These bromine VSLSs are thought to be the uncertain part of quantifying the amount of stratospheric bromine. Since nearly all of the long-lived brominated species eventually transport to the stratosphere and release Br there, which depletes O_3, the different locations of emissions and troposphere-stratosphere transport patterns have only a minor

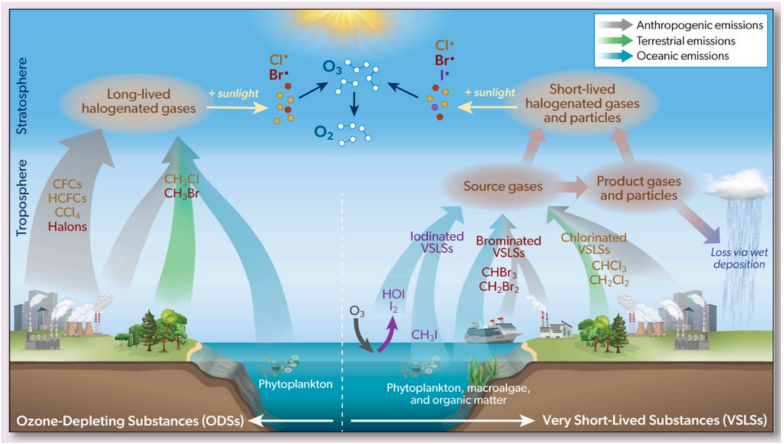

Figure 2.3: Schematic of long-lived ozone-depleting substances (ODSs) and halogenated very short-lived substances (VSLSs). Box 1-3 from Laube et al. (2022)

impact on stratospheric ozone. On the contrary, brominated very short-lived substances (VSLS) exhibit a variable local lifetime within the troposphere and undergo rapid chemical degradation. Their lifetime spans from 2-3 weeks to several months due to processes involving photolysis and interactions with OH and Cl radicals. Hence, a notable influence of bromine-containing VSLSs on stratospheric ozone depletion hinges on the interaction among different source distributions and the atmospheric transport patterns (Laube et al., 2022). However, due to their short lifetime in the troposphere, these brominated VSLS show high temporal and geographical variability, with significant differences in observed concentrations at different sites. Particularly the polyhalogenated species, have low tropospheric concentrations and very little observational data in the stratosphere, leading to difficulty in making accurate predictions regarding their global atmospheric distribution.

The two most dominant bromine-containing VSLSs in both atmosphere and ocean are thought to be dibromomethane (CH_2Br_2) and bromoform ($CHBr_3$), which mass emission fluxes together contribute more than 90% to global total very short-lived bromocarbon flux (Ordóñez et al., 2012), making a great contribution to stratospheric bromine loading and therefore ozone chemistry cycle. The global emissions of $CHBr_3$ and CH_2Br_2 have seasonal variability, with high concentrations in summer and low concentrations in winter. There is also an inter-hemispheric difference for both $CHBr_3$ and CH_2Br_2, with the North-

ern hemisphere contributing more to these emissions than the Southern hemisphere in mid- and high latitudes (Ordóñez et al., 2012).

The estimation of global bromine VSLS lower boundary for CH_2Br_2 and $CHBr_3$ usually uses two different methods, 'bottom-up' and 'top-down'. The 'bottom-up' approach gets all known possible best estimated sources of emissions from various activities on a regional and temporal basis through government reporting, culminating in a global emissions inventory and calculating how the atmosphere is responding using model-based calculations. Conversely, with a 'top-down' approach, emissions are derived from atmospheric measurements at certain locations. Models are subsequently utilized to extrapolate to lower boundary conditions, facilitating a comparison between the simulation results and actual observations. According to the deviation, the lower boundary conditions or initialization were successively adapted such that the deviation decreased and the model better represented the observations. In this thesis, the 'top-down' method is used to derive surface lower boundary.

Due to differences in data accuracy and coverage, air-sea exchange parameterization choices, and model assumptions, global emissions estimated using the 'bottom-up' approach vary widely and have high uncertainty. For example, according to Carpenter and Liss (2000), the mass flow estimate for the total annual worldwide emission of $CHBr_3$ was 220 Gg. The sea-to-air flux for the $CHBr_3$ was predicted to be 239–1758 Gg Br annually, which is three–four times more than earlier predictions (Quack and Wallace, 2003). In addition, Ziska et al. (2013) estimate a total global oceanic flux of 120/200 Gmol Br per year for $CHBr_3$ and 63/78 Gmol Br per year for CH_2Br_2 using robust fit/ordinary least squares regression techniques. These values are comparatively lower than other estimations due to the under-representation of an extreme event. While, according to new bottom-up approaches with machine learning methods, the estimates for the global oceanic emissions inventories for CH_2Br_2 and $CHBr_3$ are 54 and 385 Gg Br per year, respectively (Wang et al., 2019).

Numerous comprehensive studies have employed this approach for estimation, seeking to reproduce the concentrations derived from airborne measurements in the upper

troposphere and lower stratosphere. Particularly notable contributions in this realm have been made by researchers, including Warwick et al. (2006); Liang et al. (2010); Ordóñez et al. (2012). Warwick et al. (2006) used the prescribed surface emission scenarios to estimate the global emissions of $CHBr_3$ in a range of 400-595 Gg per year and 113 Gg per year for CH_2Br_2. Other estimates of the global oceanic Br mass flow for $CHBr_3$ and CH_2Br_2 are projected to be 425 Gg Br per year and 57 Gg Br per year, respectively, using a simple emission scheme. These estimates assume that 60% and 40%, respectively, of the emissions come from the open ocean and coastal areas (Liang et al., 2010). According to the estimation of Ordóñez et al. (2012), the global marine emission for $CHBr_3$ is 533 Gg annually and for CH_2Br_2 is 67.3 Gg per year.

Considering the transport circulation patterns, the highest concentration is generally thought to be in the tropical area, where strong upwelling occurs. For example, the higher concentration of bromocarbon emissions is shown to be located between 20°S-20°N by Warwick et al. (2006), and between 10°S-10°N by Liang et al. (2010). Within these tropical areas, the open ocean emerges as the primary source of bromine-containing VSLS, with both species being highly saturated in surface waters. Notably, the open tropical ocean, characterized by deep convection, contributes to the majority of $CHBr_3$ emissions into the upper troposphere (Warwick et al., 2006).

The tropical coastal region, rich in aquaculture, boasting high algal productivity, and facilitating rapid deep convective transport of surface emissions to the upper troposphere and lower stratosphere, is recognized as a substantial source of biogenic bromine VSLS emissions (Leedham Elvidge et al., 2013). For example, for the CH_2Br_2, the source of macroalgal emission was confined to the coastal region and weaker in the temperate zone (Yokouchi et al., 2018). Also for $CHBr_3$, the ocean is more biologically productive than the tropical averaged emissions. While the Maritime Continent, which is a coastline-rich and convectively active region, the emission for $CHBr_3$ is proved to be not stronger than other regions within tropics (Ashfold et al., 2014).

Overall, the open ocean (such as the Pacific Ocean) and narrow nearshore regions, the continental shelves, subtropical and tropical coastal waters (Quack and Wallace,

2003), the tropical upwelling area, such as the region near the equator and along ocean fronts (Butler et al., 2007), as well as some powerful localized sources, all have the potential to become significant sources contributing to the global bromine budget.

2.3.2 Brominated VSLS loading in the stratosphere

Total bromine loading in the stratosphere originates from both human activities and natural processes. As shown in Figure 2.4, the most abundant gases include various halons from anthropogenic contributions ($CBrF_3$ (H1301), $CBrClF_2$ (H1211) and other halons), very short-lived species (VSLS) from natural sources, and methyl bromine (CH_3Br) from both natural emissions and human activities. In 2010 and 2016, the total amount of bromine reaching the stratosphere decreased by 2.5 ppt and 3.2 ppt from their peak abundance of 22.1 ppt in 1999, respectively. This largest reduction in the amount of Br entering the stratosphere is seen in the abundance of methyl bromide (CH_3Br) attributed to human activities, because of the control by the Montreal Protocol. Historically, the very short-lived halogen species, such as $CHBr_3$, are not considered a great threat to stratospheric ozone depletion, due to their lower concentration and relatively short lifetime. However, due to reductions in anthropogenic emissions, the contribution of total stratospheric bromine is comparable to that from natural sources. At the same time, the amount of bromine loading from natural sources has remained fairly constant over the years. Consequently, the brominated VSLS, which are not controlled by the Montreal Protocol, have been identified as a further source for stratospheric total bromine loading (Laube et al., 2022; Dorf et al., 2006).

The transport of reactive bromine compounds into the stratosphere is shown in more detail in Figure 2.5. Direct measurements and inferred total bromine loading were conducted in the tropical tropopause (TTL) region and the extratropical UTLS region during the 2013 ATTREX campaign in the Eastern Pacific and the 2017 WISE campaign, respectively. These investigations unveiled elevated total bromine values, reaching up to 22.3 ppt and 21.6 ± 0.7 ppt, respectively (Laube et al., 2022). The total stratospheric bromine load consists of bromine-containing source gases (SG) and their degradation products

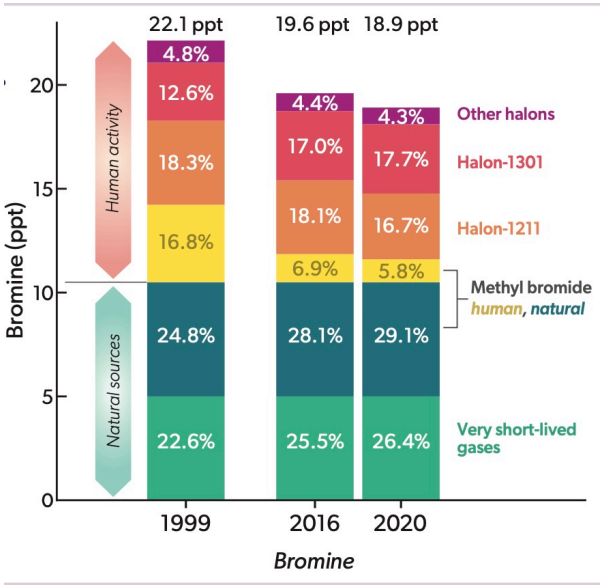

Figure 2.4: Bromine input to the stratosphere for 1999, 2016 and 2020 from different halons, CH_3Br and VSLSs. Refer to Figure 1-15 from Laube et al. (2022)

(PG). Massive quantities of organic and inorganic bromine-containing substances released into the upper troposphere and lower stratosphere (UTLS) by brominated very short-lived substances (VSLS) originate from the oceans. These biogenic brominated VSLS currently account for about 25% of the total stratospheric bromine load. Due to the different precision and accuracy of the estimation in different methods, the estimated additional contribution from natural brominated VSLS varies from 5 to 7 ppt (Barrera et al., 2020; Laube et al., 2022). A slight rise in stratospheric bromine will, particularly from the brominated VSLS, result in a significant drop in ozone (Salawitch et al., 2005). Therefore, research for the brominated VSLS loading in the stratosphere is vital for the long-term development of ozone in the 21st century (Barrera et al., 2020).

Owing to different lifetimes in the local troposphere, various brominated VSLS contribute differently to introducing both bromine containing product gas (PG) and source gas (SG) transported into the stratosphere. For example, with a lifetime of approximately 23 days, $CHBr_3$ primarily decomposes in the troposphere and mostly contributes as the PG injection, while CH_2Br_2, which has a longer lifetime of about 123 days, predominantly

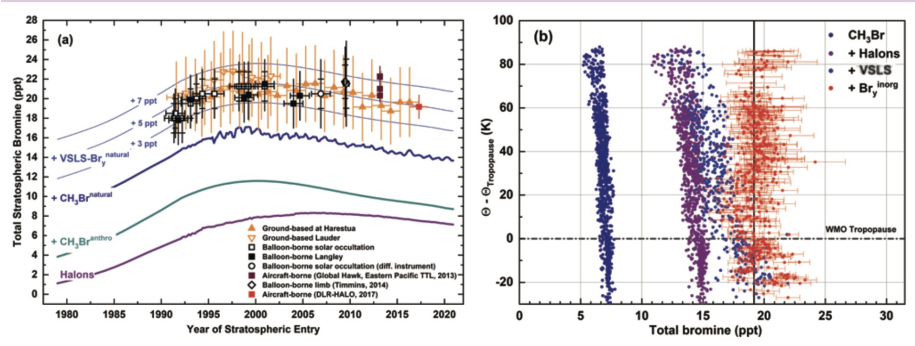

Figure 2.5: (**a**) Changes in stratospheric total bromine (the concentration of all bromine summed up by different bromine-containing species according to their bromine atoms) from 1980 to 2020. The stratospheric data were gathered through measurements of stratospheric BrO using balloon, airborne, and ground-based UV-visible techniques. These measurements originate from halon, CH_3Br (categorized into natural and anthropogenic fraction), and brominated Very Short-Lived Substances (VSLS). (**b**) Total bromine was the concentration of all bromine summed up by halons, CH_3Br, brominated VSLS and inorganic bromine (Br_y^{inorg}) according to their bromine atoms. The total bromine as a function of potential temperature distance from the WMO tropopause (θ - $\theta_{Tropopause}$) during the WISE campaign in 2017. Adapted from Figure 1-14 in Laube et al. (2022)

contributes as SG (Liang et al., 2010). Inorganic bromine compounds (Br_y^{inorg}), constituting the primary components of PG, are predominantly present as Br, BrO, HBr, HOBr and BrONO2. These substances are reactive and play a crucial role in catalytic ozone depletion cycles, as described in equations 2.1 and 2.2. The quantity of Br_y^{inorg} created by CHBr3 in the troposphere that transferred to the stratosphere is comparable to the amount of Br_y^{inorg} produced by CHBr3 in the stratosphere (Nielsen and Douglass, 2001). Since the majority of Br_y^{inorg} compounds, such as hydrogen bromide (HBr), hypobromous acid (HOBr), and bromine nitrate ($BrONO_2$), are believed to possess significant liquid sorption capacities and high uptake coefficients on ice particles (Aschmann and Sinnhuber, 2013), these soluble product gases undergo removal processes in the troposphere, including wet deposition, uptake on ice, and dehydration. During vertical transport in the tropics, ascending air masses arriving in the stratosphere through the TTL must be lifted above the level of zero radiative heating and effectively dehydrated, with soluble species in the air being removed by falling water droplets or ice particles and the final mixing ratio reaching roughly the saturation mixing ratio at the cold point. The different dehy-

dration mechanisms in the TTL and the chemical partitioning of Br_y^{inorg} in the TTL lead to variable rates of removal of soluble products from the TTL by rain or ice, resulting in different contributions of Br_y^{inorg} from brominated VSLS source gases to the stratospheric bromine load (Sinnhuber and Folkins, 2006). Some studies, however, indicate that the absorption and sedimentation of Br_y^{inorg} removal is not a particularly effective procedure since the dissolved inorganic species HBr and HOBr might release active radicals back into the gas phase by heterogeneous interaction with sulphuric acid (Aschmann et al., 2011; Montzka et al., 2011).

The most recent summary of the contribution of brominated VSLS to stratospheric bromine loading is in the World Meteorological Organization (WMO) Ozone Assessment. The total injection of product gases in the stratosphere could range from 0.4 to 4.2 ppt Br (Montzka et al., 2011). While about 2.7 ppt (1.4-4.6 ppt) of bromine was attributed to the source gases, including unmeasured species, at about 15 km altitude in the tropics and about 1.5 ppt (0.7-3.4 ppt) in the tropical cold-point tropopause at about 17 km height. Brominated VSLS inject 3–7 ppt of bromine into the stratosphere, of which 0.5–4.4 ppt Br is derived from SG injection and the remaining 1.8-4.2 ppt Br is derived from PG injection (Laube et al., 2022). In the Northern Hemisphere, the weighted average total bromine, including organic and inorganic bromine, is estimated to be 19.2±1.2 ppt, with a high bromine region in the lower stratosphere, where most of the air entering the region comes from the Asian monsoon and its adjacent tropics, with a weighted average total bromine of 20.9±0.8 ppt (Rotermund et al., 2021). The absolute value of the SG/PG injection mixing ratio is directly dependent on variable surface emissions and lower boundary conditions, as well as the intensification of convection relative to the lifetime of the individual, while the sensitivity of SG injection and PG injection to various contributing variables is different (Filus et al., 2020)

The overall contribution of VSLSs to stratospheric bromine loading depends strongly on the spatial and temporal variability of their sources, atmospheric transport pathways, removal and chemistry processes. In particular, in the TTL, the strength of the convective transport from the boundary layer is the primary load-influencing factor. The intensified

convection, especially during extreme events like El Niño, will lead to higher brominated VSLS reaching the UTLS region (Aschmann et al., 2011). In addition to the surface emission strength, the contribution of these brominated VSLS to the stratospheric load also depends on the surface emissions locations (such as in the West Pacific), their geographical distribution, and the seasonally variable boundary layer concentration, as well as on large-scale transport (Warwick et al., 2006; Aschmann, 2009; Filus et al., 2020). Previous studies have revealed that bromine injections into the stratosphere occur through a variety of different pathways rather than from a single source region (Rotermund et al., 2021; Navarro et al., 2015), which has been discussed in Section 2.3.1. In addition, the lifetime of different brominated VSLS also strongly affects the efficiency of emissions reaching the upper troposphere via atmospheric transport (Montzka et al., 2011). For example, since the chemical and removal lifetime of these individual brominated VSLS should be comparable to or shorter than the transit time through the tropical tropopause layer (TTL), the total sensitivity is lower for the longer-lived CH_2Br_2. Moreover, because of its longer lifetime, the photochemical degradation of CH_2Br_2 is just as significant as vertical transport (Aschmann and Sinnhuber, 2013). In the tropics, the degree of convection and large-scale vertical transport greatly affects the amount of the VSLS source gas injection, whereas the response of photolysis and destruction by OH radicals is comparatively minor. This is especially true for $CHBr_3$ injection.

Chapter 3

Data and method

In this thesis, the results of the Chemical Lagrangian Model of the Stratosphere (CLaMS) and aircraft observations are combined to explore the lower boundary conditions for brominated very short-lived substances (VSLS). This chapter provides an overview of the various versions of the CLaMS model utilized for simulation, as well as the datasets obtained from aircraft measurements that are employed in this study. The expanded chemistry scheme utilized for CLaMS simulation underwent initial testing in a box model mode before being adapted to a more complex global three-dimensional (3D) CLaMS model. Subsequently, an extended, long-term model simulation was carried out within the Modular Earth Submodel System (MESSy) environment, utilizing a series of base models collectively referred to as the MESSy-CLaMS model version 1.0. To address unresolved convection, the MESSy-CLaMS model was enhanced by Konopka et al. (2022) to improve convective transport, resulting in the updated MESSy-CLaMS model version 2.0. Furthermore, this thesis incorporates observational data obtained from the South-TRAC (Southern Hemisphere Transport, Dynamics, and Chemistry) campaign, along with subsequent climatology data, to augment and refine the simulation outcomes. The comparison of measured Southern Hemispheric brominated VSLS with CLaMS simulation results allows the global lower boundary conditions to be optimized.

3.1 Chemical Lagrangian Model of the Stratosphere (CLaMS)

CLaMS is a Lagrangian model developed at Forschungszentrum Jülich (e.g. McKenna et al. (2002a,b); Konopka et al. (2004, 2019)). Unlike an Eulerian model, which describes the fluid flow on a fixed grid, CLaMS uses a Lagrangian perspective in which the grid is moving with the flow. The moving and irregular grid in CLaMS is defined by 'air parcels' (APs), which denote the location and composition of individual air masses.

3.1.1 CLaMS model version 1.0

The CLaMS model, based on Lagrangian tracer transport, is composed of several modules that simulate complex atmospheric chemical and physical processes. The trajectory module (TRAJ) is used for calculating the transport of the air parcels; the chemistry module (CHEM) describes the chemical change of the employed trace gases; the mixing module (MIX) in CLaMS calculates the mixing of the air parcels with other neighboring air parcels. The overview of these modules used in CLaMS simulation is described below.

Trajectory module (TRAJ)

The advection of the air parcels is described by so-called trajectories that are determined using a fourth-order Runge-Kutta scheme, as described by McKenna et al. (2002b). There is also the possibility to calculate only the backward trajectory, which is also used in this thesis to investigate the possible sources and transport pathways of the observed air parcels. The calculations are driven by assimilated winds and temperatures from ERA5 meteorological reanalysis data (Hersbach et al., 2020). ERA5 is the fifth generation of global climate and weather reanalyses provided by the European Centre for Medium-Range Weather Forecasts (ECMWF) since 1940. The wind velocities are linearly interpolated from the adjacent grid point to the AP locations.

Mixing module (MIX)

Many Eulerian models don't explicitly simulate mixing, as it is implemented already by the immanent numerical diffusion. In contrast, within the Lagrangian model, it becomes necessary to explicitly incorporate mixing. This is particularly crucial for large tracer gradients. For instance, within the polar vortex, there are low concentrations of N_2O. If there is no mixing of air parcels during the breakdown of the vortex, it may lead to unrealistic concentrations of N_2O. This mixing scheme calculates the mixing of air parcels, strategically triggered in locations where substantial wind shear occurs (McKenna et al., 2002b). Incorporating mixing includes introducing new air parcels and merging existing ones, where the number of air parcels is not constant. This results in a more realistic portrayal of atmospheric transport.

Chemistry module (CHEM)

Most relevant to our thesis is the chemistry module (CHEM). The enhanced chemistry scheme in this thesis incorporated comprehensive reactions about bromine-containing species related to the stratosphere and brominated VSLS species. The newly incorporated species include bromoform ($CHBr_3$), dibromomethane (CH_2Br_2), bromochloromethane (CH_2BrCl), dibromochloromethane ($CHBr_2Cl$), dichlorobromomethane ($CHBrCl_2$), methyl bromide (CH_3Br), H1301 (CF_3Br), H2401 (CF_2BrCF_2Br) and H1211 (CF_2ClBr), where the relevant chemical reactions are described in more detail in chapter 4. The new chemistry scheme contains 59 chemical species and 176 reactions (45 photolytic reactions, 11 heterogeneous reactions, 105 bimolecular reactions, and 15 termolecular reactions) in the simulation. The relevant chemical rate coefficients [cm^3 s^{-1}] for bromine-containing VSLSs, and the photolysis rates [s^{-1}] calculated from absorption cross sections, were obtained from recommendations (Burkholder et al., 2015). This chemistry module calculates the change in the chemical composition of each air parcel simultaneously along its trajectory, and the chemical integrations are implemented by Carver et al. (1997) ASAD (A Self-contained Atmospheric Chemistry Code) package (McKenna et al., 2002a).

The initialization of the CLaMS chemical model follows the tracer-tracer correlation

method, as detailed in Section 2.2.2. The initialization values for CO, H_2O, HCl, and N_2O (above 400 K) were obtained from Microwave Limb Sounder (MLS) satellite observations. For O_3, HCl, H_2O, N_2O (below 400 K), and CH_4, the initializations were derived from multi-year simulations conducted by Konopka et al. (2004, 2007). Additionally, initialization values for NOy (NO, NO_2, NO_3, $2\times N_2O_5$, HNO_3, HO_2NO_2, $ClNO_2$, etc.), F11, F12 are correlated with N_2O from ACE-FTS data. While inorganic chlorine (Cly, including Cl, ClO, Cl_2O_2, HCl, Cl_2, $ClONO_2$, $ClNO_2$, HOCl, etc.) and inorganic bromine (Br_y^{inorg}, encompassing Br, HBr, HOBr, BrO, Br_2, $BrONO_2$, etc.) data are derived from correlations with N_2O in balloon data (Andreas Engel et al., personal communication). Minor species are derived from the Mainz 2D photochemical model simulation results (Grooß, 1996). Concerning brominated very short-lived substances (VSLS), CH_3Br, and halons, the initialization values in Section 4.4 are based on correlations with N_2O from the results of box model simulations. The initialization data in subsequent simulations were obtained from correlations with N_2O from Rotermund et al. (personal communication).

To conduct tests, CLaMS can also be employed in a box model mode, simulating one or more individual air parcels along their trajectories without mixing, facilitating the analysis of chemistry. The box model employed in this thesis is a zero-dimensional model that utilizes the chemistry module and prescribes artificial trajectories. The setup and specific simulation results of the conducted simple box model simulations will be elaborated in the subsequent Section 4.2.

This thesis investigates the lower boundary conditions simulated in the CLaMS model, integrated into both classical and Modular Earth Submodel System (MESSy) environments. MESSy consists of a modular interface structure connecting sub-models to a base model and facilitating data exchange among them within a unified executable. This framework offers a generalized interface structure, enabling novel possibilities for studying feedback mechanisms among diverse bio-geo-chemical processes (Jöckel et al., 2005). The MESSy-CLaMS model represents a slightly more intricate global three-dimensional (3D) version of the CLaMS model, integrating various sub-modules and flexible model configurations. The simulation first tests the new chemistry scheme in the CLaMS simple box

model. As the lower boundary file was not easy to construct in classic CLaMS, the simulation was then transferred to the MESSy-CLaMS version, which offered more options for constructing the boundaries.

3.1.2 CLaMS model version 2.0

In MESSy-CLaMS model version 1.0, only almost-isentropic deformations driven by horizontal strain and vertical shear are considered in the mixing scheme (Konopka et al., 2019). In contrast to the stably stratified stratosphere, the troposphere suffers from vertical instability in transport, which is not accounted for in MESSy-CLaMS model version 1.0. This omission results in an underestimation of a significant part of upward vertical transport (Konopka et al., 2019). To address this limitation and enhance the representation of upper-level convective transport in tropical regions, the simulations in this thesis were extended to the updated CLaMS module version 2.0.

CLaMS version 2.0, an improved model based on CLaMS 1.0 developed by Konopka et al. (2019, 2022), extended the tropospheric transport scheme by adding additional tropospheric mixing and vertical convection. This updated version, depicted in Figure 3.1, incorporates three distinct transport modes: isentropic mixing (as in CLaMS 1.0), tropospheric mixing, and unresolved convection updrafts. The enhanced upward transport caused by deep convection lifts air parcels from the lower boundary to the upper troposphere and even into the stratosphere.

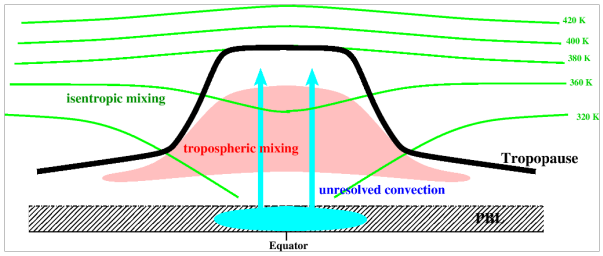

Figure 3.1: Update of tropospheric mixing and unresolved convective updrafts (Konopka et al., 2022).

In addition to the isentropic mixing, already applied in the CLaMS 1.0 version, the

other two insufficiently resolved transport mechanisms occur where the vertical stability is sufficiently low. The square of the dry and moist Brunt–Väisälä frequency (BVF) is used to quantify the instability condition regarding the potential temperature lapse rate. The tropospheric mixing is triggered where the lapse rates of the potential dry temperature is low; the additional updraft driven by convection (especially deep convection) happens in regions with conditionally unstable lapse rate of the moist potential temperatures. The equation for calculating the potential temperature driven by deep convection is derived from Konopka et al. (2019), with further details provided in Section 6.2.1.

The simulations in the MESSy-CLaMS 2.0 model enhance vertical convection, resulting in faster transport of air parcels and younger age of air. The added tropospheric mixing scheme enables air to mix also vertically. All of these improve the representation of the effect of lower boundary conditions on air parcels in the upper atmosphere.

3.2 Observational data

The aircraft observational data were used to evaluate the interpretation of model simulation results. The data used in this thesis contain measurement data from the SouthTRAC campaign and climatology data (UFra) derived by Jesswein et al. (2022).

3.2.1 Southern Hemisphere Transport, Dynamics, and Chemistry (SouthTRAC) data

Measurements of brominated VSLS were made using the Gas Chromatograph for Observational Studies using Tracers (GhOST), on board the High Altitude and Long Range Research Aircraft (HALO) in the framework of the SouthTRAC campaign. The SouthTRAC campaign covered three months from September to November 2019. During the campaign, HALO measured for 183 flight hours, reaching potential temperatures of up to 409 K. Figure 3.2 shows all transfer flights between Oberpfaffenhofen (Germany) (48°N, 11°E)) and South America. The other flights, shown in the right figure, all departed from Rio Grande (Argentina) (53°S, 67°W)). The flight tracks cover regions in the South-

ern Hemisphere, including the southern Pacific, southern Atlantic oceans and Antarctica (Jesswein et al., 2021).

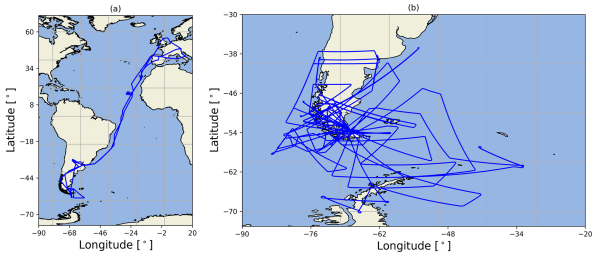

Figure 3.2: Flight tracks of the SouthTRAC campaign, the left figure are the transfer flight tracks, the right figure are the measurement flight tracks (Jesswein et al., 2021).

The GhOST instrument employed on HALO aircraft contains two chromatographic measurement channels. The first channel combines an isothermally operated gas chromatograph (GC) with an electron capture detector (ECD) (GhOST-ECD). The measured SF6 with a high time resolution of one minute is used in this thesis to determine the age of air. The second measurement channel in standard configuration couples a temperature-programmed GC with a quadrupole mass spectrometer (MS) (GhOST-MS) with a lower time resolution of six minutes (Jesswein et al., 2021). The GhOST-MS was operated in Electron Impact Ionisation (EI) mode for broader mass spectra in this SouthTRAC campaign to increase the number of measurable substances (Jesswein et al., 2022). The measured mixing ratio of bromine-containing species (including very short-lived and long-lived species) in the second channel was used to evaluate and optimize the simulation results. In addition, for better comparison with modeling results, the observational data in the latter chapters are linearly interpolated in time.

3.2.2 A climatology of brominated species

A climatology of bromide observations as part of the project was provided by Markus Jesswein and Andreas Engel from the University of Frankfurt (Jesswein et al., 2022), based on previous aircraft campaigns, the HIAPER Pole-to-Pole Observations (HIPPO) and Atmospheric Tomography (ATom) missions. The HIPPO mission measurements of

atmospheric concentrations were conducted by NSF/NCAR High-performance Instrumented Airborne Platform for Environmental Research (HIAPER) aircraft, covering regions approximately pole-to-pole from 85°N to Antarctica coastal area (65°S) over five missions (Jesswein et al., 2022). HIPPO-1 took place in January 2009, HIPPO-2 from October to November 2009, HIPPO-3 from March to April 2010, HIPPO-4 from Jun to July 2011, and HIPPO-5 from August to September 2011. The observed data were collected and analyzed from two Whole Air Samplers (WASs), the Advanced Whole Air Sampler (AWAS) and the NOAA Whole Air Sampler (NWAS).

The ATom mission payload on the NASA DC-8 aircraft occurred in four seasons from 2016 to 2018. The merged data sets are from ATom-1 (Jul-Aug 2016), ATom-2 (Jan-Feb 2017), ATom-3 (Sep-Oct 2017), and ATom-4 (Apr-May 2018). The flight range extends from north to south between the Greenland and the South Pacific, and from east to west between the Atlantic Ocean and Arctic (Jesswein et al., 2022). Data from ATom's mission include the WAS operated and analyzed by the University of California. The latest ATom mission added another WAS data from the NOAA/GML's Programmable Flask Package (PFP) and the data from NCAK Trace Organic Gas Analyzer (TOGA) instrument.

The climatology by Jesswein et al. (2022) combined all of the observations above for 4 different seasons and are binned in 10° latitude intervals from 90°S to 90°N. The vertical altitudes are binned into 16 bins, ranging from 280 K to 440 K theta. The results of the seasonal distribution of CH_2Br_2 and $CHBr_3$ from climatology are depicted in Figures F.1 and F.2.

Chapter 4

Preparation of the global simulation with VSLS chemistry

This chapter describes the preparation of the global model simulations with VSLS chemistry. First, the incorporation of the additional bromine-containing species into the chemistry scheme is presented in Section 4.1. Two test simulations with the updated chemistry scheme were carried out in the box model, shown in Section 4.2. Finally, the validated scheme was applied to the global three-dimensional (3D) mode of CLaMS in the MESSy environment, and the first simulation results are shown in Section 4.3.

4.1 Incorporation of bromine-containing species and reactions

In order to carry out the intended simulations, the CLaMS chemistry scheme had to be updated to include both the bromine-containing very short-lived and long-lived brominated species. Their related photolysis and photochemical reactions were incorporated into the CLaMS chemistry module.

The newly incorporated very short-lived brominated species include dibromomethane (CH_2Br_2), bromoform ($CHBr_3$), bromochloromethane (CH_2BrCl), dibromochloromethane ($CHBr_2Cl$) and dichlorobromomethane ($CHBrCl_2$). The long-lived species include methyl bromide (CH_3Br) and the three halons: H1211 (CF_2ClBr), H1301 (CF_3Br), and H2402

(CF_2BrCF_2Br).

Absorption cross sections are needed to determine the photolysis rate constants for these species' photolysis processes. Some of the absorption cross sections (unit cm^2 $molecule^{-1}$) are reported to be temperature-independent ($CHBr_2Cl$, CH_2BrCl and $CHBrCl_2$), while others are temperature-dependent (H1301, H2402, H1211, $CHBr_3$, CH_2Br_2 and CH_3Br), as recommended by Burkholder et al. (2015). As an example, Figure 4.1 shows the absorption cross section for temperature-dependent H2402 and $CHBr_3$ and temperature-independent CH_2BrCl at different wavelength.

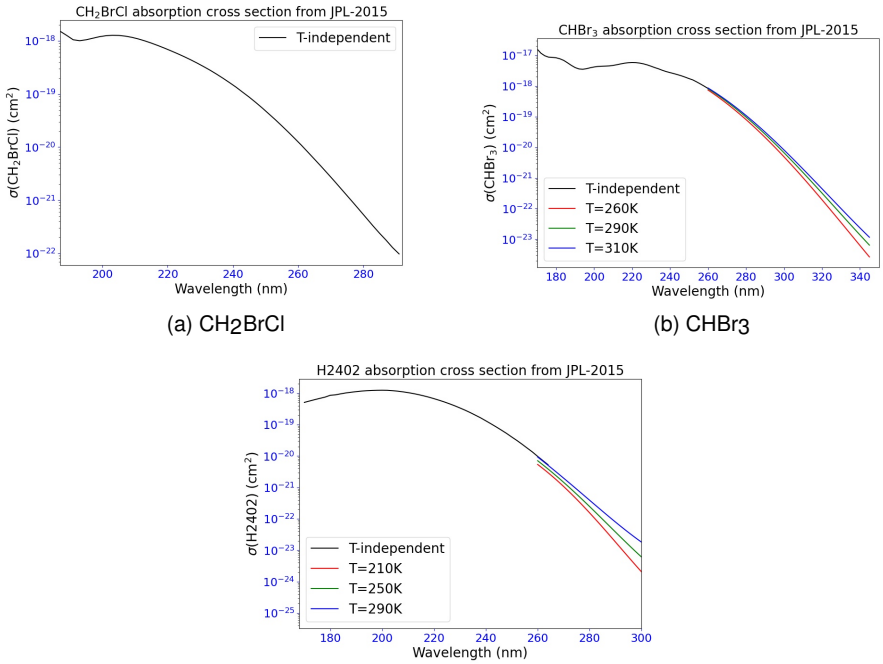

(a) CH_2BrCl (b) $CHBr_3$

(c) H2402

Figure 4.1: Absorption cross sections for temperature-dependent H2402 (long lifetime), $CHBr_3$(short lifetime) and temperature-independent CH_2BrCl. The X-axis is wavelength, Y-axis is the absorption cross section.

In addition to the photolysis reactions from Burkholder et al. (2015), the photochemical reactions were also incorporated. These reactions are summarized in Figure 4.2, including those with hydroxyl radical (OH), the first excited state of oxygen ($O(^1D)$) and

chlorine radical (Cl). Different species can react with different radical species. The reaction rates and absorption cross sections were also taken from JPL-2015 recommendation (Burkholder et al., 2015) for every species.

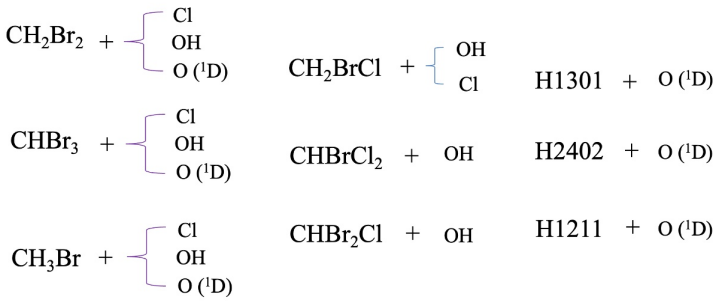

Figure 4.2: Incorporated chemical reactions for bromine-containing species with OH, Cl and O(^{1}D) separately.

4.2 Classical CLaMS box model simulation

First, test simulations with the CLaMS box model were performed to check if the bromine reactions were incorporated correctly. To replicate the species profile in the TTL, the simulations use a single air parcel ascending in the tropics. Then air parcels at constant pressure level (multiple latitudes) were used to determine local photochemical lifetimes.

The first CLaMS box model simulation, similar to the setup by Röckmann et al. (2004), uses a vertical velocity inferred from the water vapour 'tape-recorder' (Mote et al., 1996). In this setup, two single air parcel simulations were performed. In the first simulation, a single air parcel followed the typical Brewer-Dobson circulation velocity, ascending over four years from 300 hPa to 3 hPa. Similarly, in the second simulation, the air parcel ascended from 100 hPa to 1 hPa over the same four-year period.

The simulation result shows the single air parcel in the tropics at 15°N ascending slowly, with the mixing ratio decreasing as altitudes increase. For example, three typical species with different lifetimes, including the long-lived H1301, the medium-lived CH_2Br_2, and the very short-lived $CHBr_3$, have been chosen as examples to illustrate the results.

Their tropical profiles from 100 hPa to 5 hPa are shown in Figure 4.3a, Figure 4.3b and Figure 4.3c.

Similarly, the verification of simulation results is also described in terms of reaction rates and lifetime at different pressure levels. The three examples are shown in Figure 4.3. According to the different reaction rates at different altitude levels (Figure 4.3d, 4.3e, 4.3f), the photolysis reaction and the reaction with OH in the troposphere or lower region play the most crucial role in the depletion process. The other two reactions with O(^{1}D) and Cl radicals have a minor impact on the decomposition of the source gases. The latitude-dependent chemical lifetime at each altitude can be derived from the depletion rate. Take CH_2Br_2 as an example, the chemical lifetime is calculated by equation 4.1.

$$\tau_{\mathrm{CH_2Br_2}} = \frac{1}{J + b_{\mathrm{O(^1D)}} * [\mathrm{O(^1D)}] + b_{\mathrm{OH}} * [\mathrm{OH}] + b_{\mathrm{Cl}} * [\mathrm{Cl}]} \tag{4.1}$$

Where J is the photolysis rate, $b_{\mathrm{O(^1D)}}$, b_{OH}, b_{Cl} are the different reaction rates for reacting with O(^{1}D), OH, and Cl; [O(^{1}D)] is the concentration of O(^{1}D), [OH] is the concentration of OH, [Cl] is the concentration of Cl. Unlike the global average lifetime, the altitude-dependent lifetime at 15°N is the local lifetime. Three species as examples are shown in Figure 4.3g, 4.3h and 4.3i.

The second test simulation of the incorporated chemistry scheme used multiple air parcels, assuming all air parcels remaining at constant pressure levels, simulated at different latitudes. This simulation is chosen to determine local photochemical lifetime. The initialization data for VSLSs and halons were obtained from the WMO ozone assessment (Engel et al., 2018). 18 air parcels were simulated at two constant pressures (100 hPa and 300 hPa) for one year at latitudes between 85°S and 85°N. Similar to the first simulation, the multiple air parcels' latitude-dependent mean lifetime at 100 hPa and 300 hPa for each species is calculated, and the examples are shown in Figure 4.4.

The average lifetime of each species at the 100 hPa and 300 hPa levels is calculated based on latitude-dependent lifetimes, weighted by the total area of each latitude bin range, as illustrated in equation 4.2

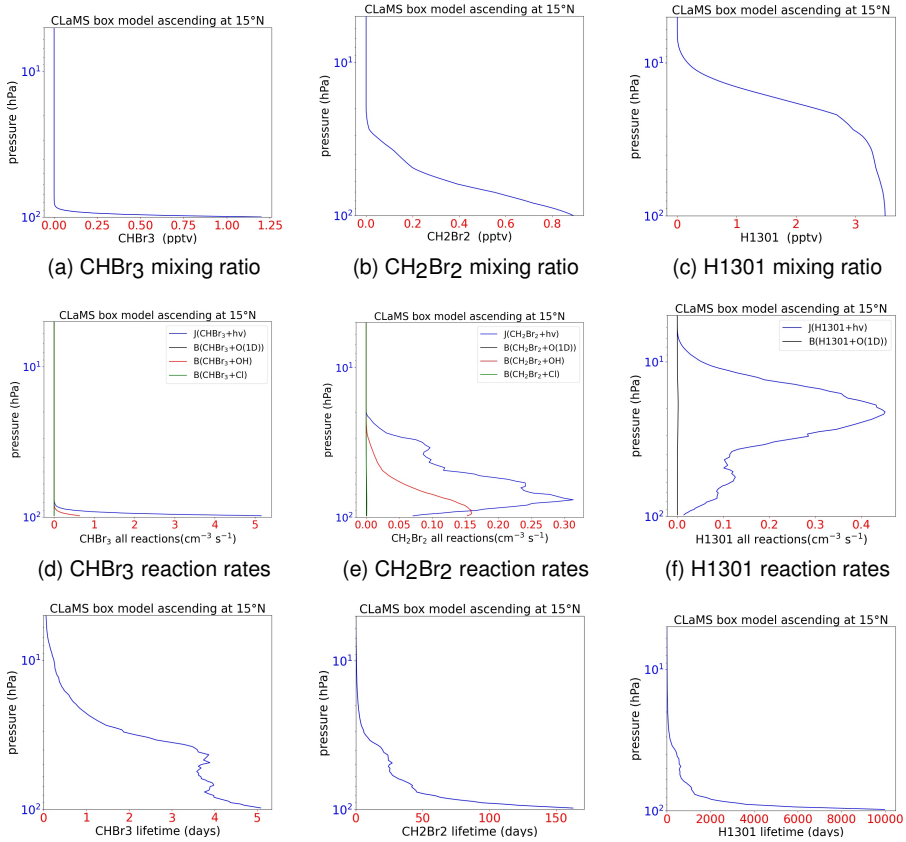

(a) $CHBr_3$ mixing ratio (b) CH_2Br_2 mixing ratio (c) H1301 mixing ratio

(d) $CHBr_3$ reaction rates (e) CH_2Br_2 reaction rates (f) H1301 reaction rates

(g) $CHBr_3$ lifetime (h) CH_2Br_2 lifetime (i) H1301 lifetime

Figure 4.3: Profiles for three species, including very short-lived $CHBr_3$, medium-lived CH_2Br_2 and long-lived H1301. The tropical mixing ratio profile for a single air parcel with different pressure (**a**-**c**). The photochemical reaction rates (**d**-**f**) for the reactions with OH (red line), with O(^{1}D) (black line), and with Cl (green line). The green line and black line are nearly zero and overlap with each other. Local lifetimes at different altitudes are presented in panels (**g**-**i**).

$$
\begin{aligned}
m[i] &= 365d/\ln(\mu_{max}/\mu_{min}) \\
wt[i] &= 0.5 \times (\sin(\mathrm{lat1}) - \sin(\mathrm{lat0})) \\
\tau_{mean} &= \frac{1}{\sum(wt[i]/m[i])}
\end{aligned}
\tag{4.2}
$$

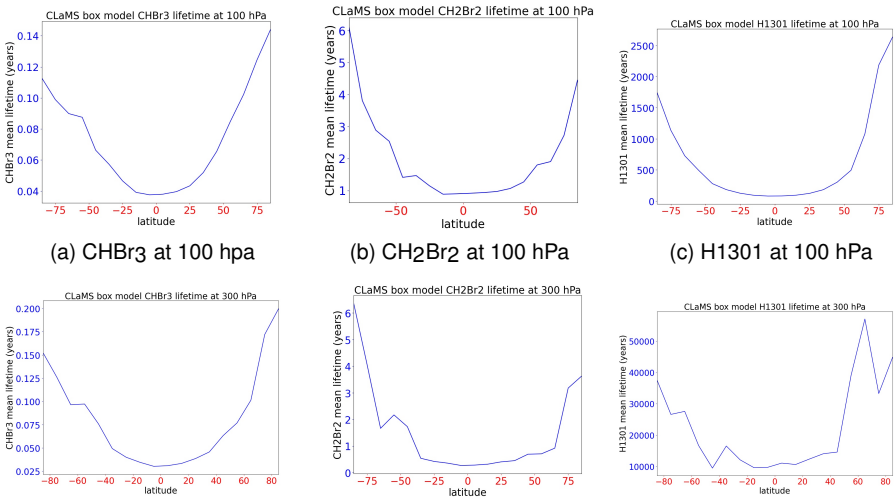

(a) $CHBr_3$ at 100 hpa (b) CH_2Br_2 at 100 hPa (c) H1301 at 100 hPa

(d) $CHBr_3$ at 300 hPa (e) CH_2Br_2 at 300 hPa (f) H1301 at 300 hPa

Figure 4.4: latitude-dependent lifetime for $CHBr_3$, CH_2Br_2 and H1301 under 100 hPa and 300 hPa pressure levels.

Here, μ means the volume mixing ratio for every species, while m[i] denotes the global lifetime for each species within every air parcel, totaling 18 air parcels. The latitudes range from 85°S to 85°N (at 10° intervals), where lat1 and lat0 denote the starting and ending latitudes for each latitude range. Additionally, wt[i] represents the area weight for each latitude bin, and τ signifies the latitudinal mean lifetime for each species.

Table 4.1 lists the global annually averaged atmospheric lifetimes obtained from the World Meteorological Organization (WMO) Ozone Assessment (2018; 2022), and the calculated latitudinally averaged local lifetimes. Within the table, a comparative analysis is presented between global lifetimes and local lifetimes at distinct pressure levels (100 hPa and 300 hPa). It is imperative to acknowledge that long-lived species exhibit a pronounced altitude dependence, making them incomparable to the global mean average. Consequently, direct comparisons between global lifetime and those on specific pressure levels, particularly for halons characterized by very long transport lifetime, are deemed inappropriate. Despite these differences, when examined at an order of magnitude scale, there are no obvious signs of implementation errors. Therefore, the newly incorporated chemistry scheme is appropriately justified by the classical CLaMS run.

Latitudinally averaged local lifetime and global mean lifetime (days)				
Species	100 hpa	300 hpa	WMO (2018)	WMO (2022)
$CHBr_3$	19	17	16 (8-23)	13 (8-23)
CH_2Br_2	439	173	150 (80-890)	147 (80–890)
CH_3Br	2275	853	292	292
CH_2BrCl	546	195	165 (89-1055)	162 (89–1050)
$CHBr_2Cl$	46	35	59 (28-225)	49 (28–225)
$CHBrCl_2$	41	34	66 (38-250)	66 (38–250)
H1211	5090	19202	5840	5840
H1301	53531	4899278	26280	26280
H2402	5404	27692	10220	10220

Table 4.1: The simulated latitudinally averaged local lifetime for all species under 100 hpa and 300 hpa, compared with global atmospheric mean lifetime from WMO ozone assessment (WMO 2018; 2022)

4.3 Transfer to MESSy-CLaMS

Following the validation of the implemented chemistry scheme in the classical CLaMS, the simulation transition from the box model to the more complex global 3D chemical transport model was performed in the MESSy environment (known as MESSy-CLaMS (Jöckel et al., 2005)). This adaptation offers increased flexibility in various aspects, such as the formulation of the lower boundary. Although these two CLaMS versions are coded differently, their common origin ensures a striking structural similarity. The same settings and incorporation were therefore repeated in the MESSy-CLaMS model and this transfer to MESSy was also tested by repeating the identical box model simulation from above (Section 4.2) over one year.

The comparison of simulation results between the classical and MESSy-CLaMS models is illustrated in Figure 4.5, using $CHBr_3$, $CHBr_2Cl$, and CH_2Br_2 as representative examples. These figures depict the depletion of mixing ratios for air parcels at 5°N and 100 hPa pressure level during the period from October 2010 to August 2011. It is evident that there are differences in the depletion of mixing ratios shown in the two distinct box

model simulations. This discrepancy likely arises from slight differences in the timing of calculating photolysis rates and chemistry between the MESSy-CLaMS model and the classical CLaMS model. Despite these variations, these results are similar (shown in red and blue lines in Figure 4.5), confirming that the incorporated chemistry scheme can effectively be employed in the complicated MESSy-CLaMS model. As the differences are acceptable, the following simulations are performed in the MESSy-CLaMS model.

4.4 Global 3D MESSy-CLaMS

The first global three-dimensional (3D) MESSy-CLaMS simulation with 1.3 million air parcels was performed, starting from May to November 2019 to cover the SouthTRAC period. The vertical range of the simulation is from the surface to 900 K potential temperature with 32 levels, with a horizontal resolution of around 100 km. The wind data used for the simulation were taken from the global climate and weather reanalysis data ERA5 produced by ECMWF. The initialization and lower boundary of the newly incorporated brominated species were based on tracer-tracer correlations with N_2O from the previous box model simulation results.

Figure 4.6 depicts the zonal mean distribution of $CHBr_3$ and CH_2Br_2 obtained from the MESSy-CLaMS model after a five-month simulation period. The lower tropospheric layer demonstrates a distribution of boundary mixing ratios for $CHBr_3$ and CH_2Br_2, with predominantly high mixing ratios concentrated in tropical regions. As altitude increases, there is a corresponding decrease in mixing ratios attributed to upward transport within the tropical pipe and chemical depletion in the atmosphere, followed by a downward transport to higher latitudes in both hemispheres. This distribution adheres to atmospheric air parcel transport patterns, providing evidence of the successful initial 3D simulation of the MESSy-CLaMS model. However, particularly for $CHBr_3$, a notable decrease is observed at higher altitudes around the tropopause region, where the mixing ratio are markedly lower. This phenomenon may be attributed to factors such as slow upward transport, chemical reaction rates, or inaccuracies in the lower boundary, warranting further detailed investigation.

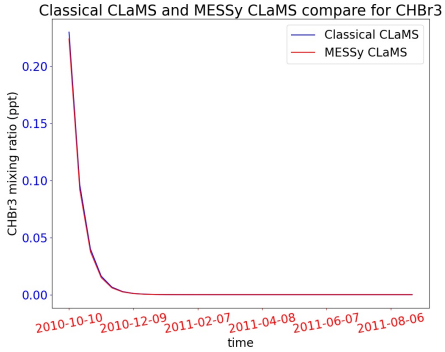

(a) $CHBr_3$

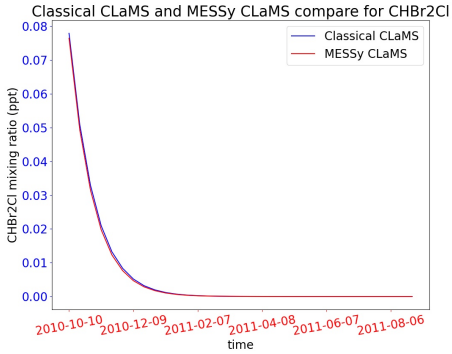

(b) $CHBr_2Cl$

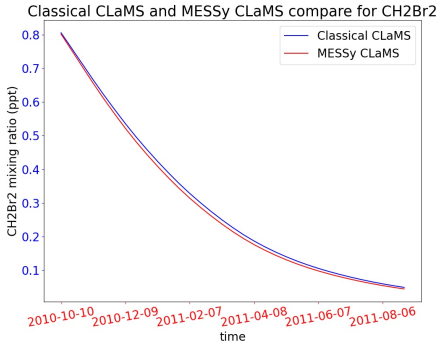

(c) CH_2Br_2

Figure 4.5: Comparison of box model simulated profile between classical CLaMS and MESSy-CLaMS at 5°N and 100 hpa pressure level, the purple line is MESSy-CLaMS simulation results, and the yellow line is the classical CLaMS simulation results.

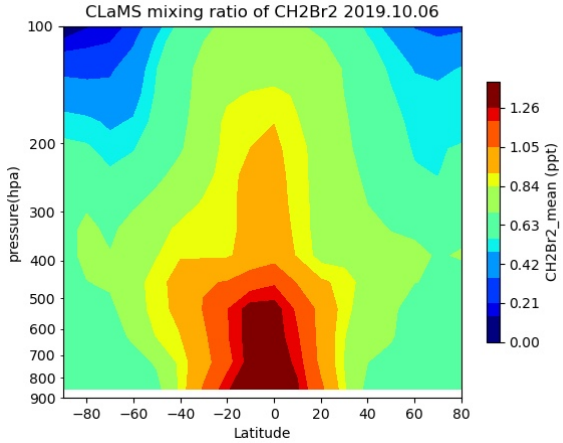

(a) CH_2Br_2

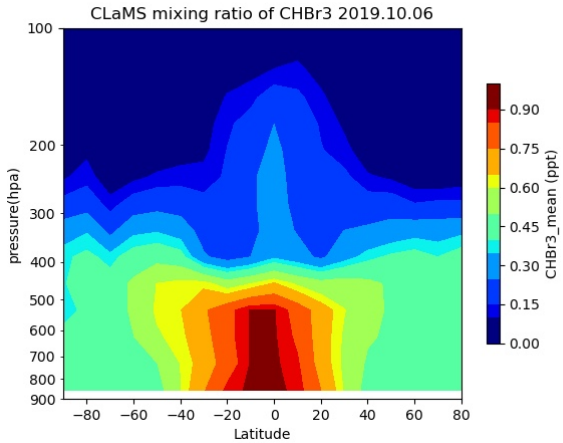

(b) $CHBr_3$

Figure 4.6: Altitude-latitude cross section of zonal mean CH_2Br_2 (**a**) and $CHBr_3$ (**b**) for MESSy-CLaMS model simulation on October 6th in 2019.

Chapter 5

Incorporation of scavenging parameterization and additional convection processes

A series of sequential 6-month global 3D MESSy-CLaMS model simulations were carried out following a 'top-down' approach. This implies that the model results were iteratively compared with observations, and the model settings, such as boundary conditions or initialization data, were adjusted accordingly in successive steps to reduce deviations and enhance the model's representation of the observations. During this process, the settings for the MESSy-CLaMS model were updated. In order to gradually optimize the surface emission distribution on a global scale, the modeled bromine-containing VSLS mixing ratios were compared with observational data in UTLS regions. Section 5.1 includes the added tropospheric HOBr/HBr sink parameterization, and the comparison of simulation results with modeling without HOBr/HBr scavenging. Section 5.2 describes the updated MESSy-CLaMS 2.0 simulation and provides details of the simulation results compared with the observational data from the 2019 SouthTRAC campaign.

5.1 HBr and HOBr scavenging

Given the success of the test simulations with the updated bromine chemistry setup, and the unavailability of climatology data from Jesswein et al. (2022) at the time of conducting the simulation, the same setup from test simulation was also used for the calculations of a global 3D chemistry simulation. For the global simulation, the initialization for the bromine-containing species is needed. This first guess lower boundary was based on observations from the 2017 WISE (Wave-driven ISentropic Exchange) campaign (Rotermund et al., 2021) (also personal discussion from Jens-Uwe Grooß), which conducted flights originating from Shannon, Ireland. These flights covered the upper troposphere and lower stratosphere (UTLS) from late summer to autumn. As shown in Figure 5.1, for CH_3Br, halons, and inorganic bromides (Br_y^{inorg}), the used lower boundary does not vary with latitude and time. While for bromine-containing VSLSs, the derived first estimate for lower boundary condition is dependent on latitude but constant in time. The latitude dependence reflects the larger observations in lower latitudes and smaller in higher latitudes (above 45°N and above 45°S), with linear interpolation between them.

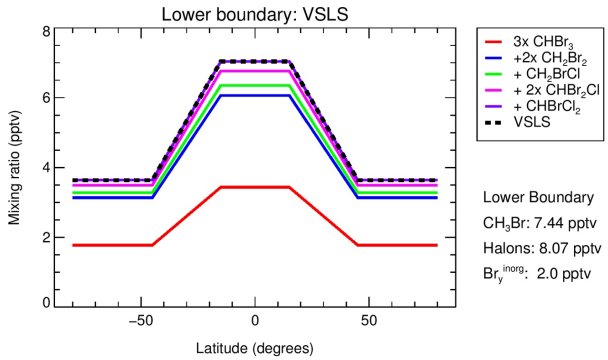

Figure 5.1: The accumulated mixing ratio of the lower boundary conditions for CH_3Br, halons, Br_y^{inorg} and brominated VSLS. The value of lower boundary for brominated VSLS are shown accumulated according to their Br atoms as a function of different latitudes. The different colours represent different VSLS species: $CHBr_3$ (red line), CH_2Br_2 (blue line), CH_2BrCl (green line), $CHBr_2Cl$ (pink line) and $CHBrCl_2$ (purple line). The dashed black line is the total bromine for all brominated VSLS.

As the total bromine consists of four significant contributors in the troposphere (Roter-

mund et al., 2021), CH_3Br, halons, brominated VSLS and inorganic bromine species, the simulated total bromine was divided into four groups. The values of bromine within each group were shown accumulated according to their Br atoms. The correlations between the mixing ratios of the four groups of brominated species and N_2O were used to derive the initialization value and investigate the simulated discrepancy in chemistry. Figure 5.2 shows the measured mixing ratio correlations between N_2O (ppb) and brominated species (ppt) in four groups during the WISE campaign in fall 2017 (Rotermund et al., personal communication, 2021).

To illustrate the differences between simulations and observations, the initialization is consistent with the correlation of the WISE observations. The N_2O-total bromine relationships for the initialization on the first day are shown in Figure 5.3a, which are consistent with the observations, as shown in Figure 5.2. Based on the simulation results for July 20, 2019, as depicted in Figure 5.3b, the correlations between N_2O and inorganic bromine components exhibit rapid breakdown. For instance, at a concentration of 320 ppb N_2O, the initial mixing ratio of Br_y^{inorg} was approximately 4.1 ppt on the first day. After 50 days, the mean mixing ratio significantly increased to 5.33$\pm$0.46 ppt, suggesting a notable discrepancy between the tropospheric conversion of Br_y^{inorg} and the observed values.

The discrepancy of Br_y^{inorg} between simulation and observation is likely due to the lack of sink processes for the soluble inorganic bromine HOBr and HBr in the troposphere, i.e., scavenging in water and ice clouds for HBr and HOBr in the troposphere. To verify this hypothesis, the chemistry scheme was enhanced with a parameterization for liquid washout and ice uptake. This addition facilitated the scavenging chemistry of Br_y^{inorg} by introducing cloud liquid water content (CLWC) and cloud ice water content (CIWC) to absorb and eliminate HOBr and HBr from the gas phase. The values for CLWC and CIWC were also taken from the ERA5 reanalysis data provided by ECMWF (European Centre for Medium-Range Weather Forecasts) model. The removal of HOBr and HBr was parameterised using a hypothetical chemical sink reaction formulated as binary reaction with CLWC and CIWC, as illustrated in equations 5.1-5.4.

To derive the sink reaction rate coefficients, classical CLaMS box model was em-

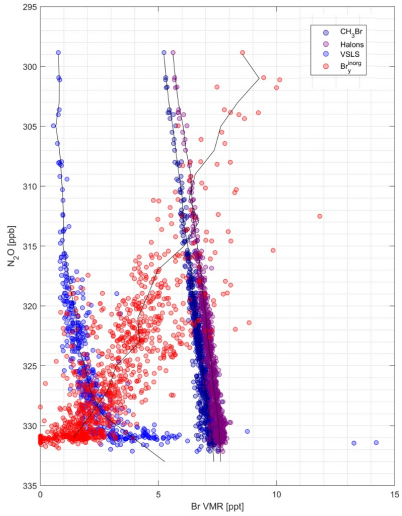

Figure 5.2: Relationship of mixing ratios between N_2O (ppb) and brominated species (ppt) in four groups during the WISE campaign in the fall of 2017. Within each group, values for all brominated species are shown accumulated according to their Br atoms: CH_3Br (dark blue circle), halons (purple circle), brominated VSLS (light blue circle) and inorganic bromine (red circle). The black line is the mean mixing ratio for each group. This figure is derived from Rotermund et al. (2021).

ployed to asses the reduction of Br_y^{inorg} (include HBr, HOBr, Br, BrO, $BrONO_2$, BrCl and Br_2). The initial estimation of the order of magnitude for the inorganic bromine reaction rate was based on the HBr reaction. The assumption was made that 1 ppt of HBr could deplete to 0.5 ppt per day. Considering the initial mixing ratio of HBr as 1 ppt, the CLWC as $1*10^{-5}$ (convertible to $1*10^{14}$ cm^{-3}), and with the total number density (TND) as $1*10^{19}$ cm^{-3}, the formulation for the HBr depletion rate is expressed as follows:

$$\mathrm{d[HBr]/dt = k\,[HBr]\,[CLWC]}$$

$$0.5*10^{-12} \times \mathrm{TND/1\,day} = \mathrm{k} \times 1*10^{-12} \times \mathrm{TND} \times 1*10^{14}\,\mathrm{cm}^{-3}$$

$$\mathrm{k} = 0.5/(86400\,\mathrm{s} \times 1*10^{14}\mathrm{cm}^{-3}) = 5.79*10^{-20}\,\mathrm{cm}^3\mathrm{s}^{-1}$$

Given the HBr and HOBr are unlikely to decrease so rapidly, the calculated sink reaction rate coefficient (k) $5.79*10^{-20}$ cm^3 s^{-1} should be regarded as an upper limit. Subsequent to this criterion, a series of tests with varying reaction rate coefficient values were

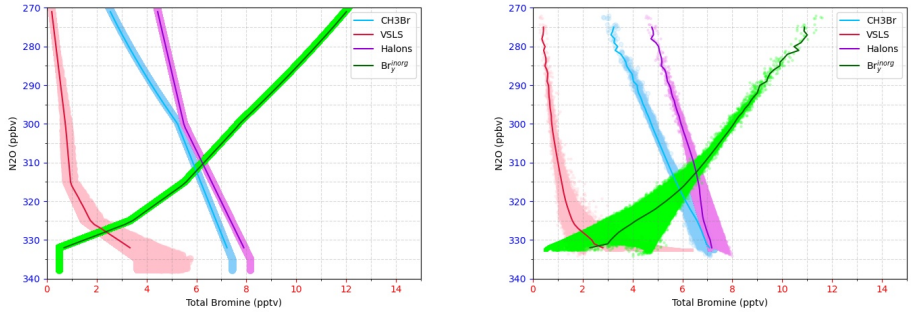

(a) Total bromine on 1 May 2019

(b) Total bromine on 20 July 2019

Figure 5.3: Relationship of mixing ratios between N_2O (ppbv) and brominated species (ppt) in four different groups from CLaMS 1.0 model simulation. Within each group, all brominated species are summed up according to their Br atomicity: CH_3Br (blue), halons (purple), brominated VSLS (pink) and inorganic bromine (green). The solid line is the mean mixing ratio for each group. The results are shown for the initial time on 1 May (**a**) and for 20 July (**b**).

performed within the classical CLaMS box model, employing a single air parcel from May 1st to June 22nd. These tests aimed to discern the impact of the reaction rate coefficient on the mixing ratios of inorganic bromine in the troposphere. Following multiple tests, the reaction rate coefficients were fine-tuned to $1.2 * 10^{-20}$ cm^3 s^{-1}. The comparison of simulation results with different coefficient rates is illustrated in Figure A.1. This modification resulted in the anticipated depletion of Br_y^{inorg}, offering the precise representation of the removal processes.

$$\mathrm{CLWC} + \mathrm{HBr} \rightarrow \mathrm{CLWC} \tag{5.1}$$

$$\mathrm{CIWC} + \mathrm{HBr} \rightarrow \mathrm{CIWC} \tag{5.2}$$

$$\mathrm{CLWC} + \mathrm{HOBr} \rightarrow \mathrm{CLWC} \tag{5.3}$$

$$\mathrm{CIWC} + \mathrm{HOBr} \rightarrow \mathrm{CIWC} \tag{5.4}$$

Following the implementation of the Br_y^{inorg} removal scheme in the MESSy-CLaMS 1.0 model, updated simulations were performed and compared with previous simulations. After three months of simulations, the mean mixing ratio versus potential temperature

at 40°-60°N as a vertical coordinate in Figure 5.4a shows that near tropopause region (with potential temperatures in the range of 340-380 K), Br_y^{inorg} is lower in the parameterized simulation (green dashed line) than in the previous simulation (black solid line). For instance, at a potential temperature of 338 K, the mixing ratio of Br_y^{inorg} in simulations with and without the HBr and HOBr sink is 3.25 ppt and 4.67 ppt, respectively. Compared to Figure 5.3b, the similar figure on the same day's simulation (shown in Figure 5.4b), shows the new simulated averaged correlations between Br_y^{inorg} and N_2O (the solid green lines). For example, at a N_2O mixing ratio of 320 ppb, the mean mixing ratio of Br_y^{inorg} is 4.34±0.93 ppt. Although this value is notably lower than the simulation without the scavenging process (5.33±0.46 ppt), it demonstrates substantial variability and is still slightly higher than 4.1 ppt. This implies that the simulation, incorporating HBr and HOBr scavenging processes, has shown improvement somehow but not in fully satisfactory agreement with the observations (refer to Figure 5.2). This discrepancy could be attributed to various factors, including dynamic transport, lower boundary values, and chemical reactions.

Specifically regarding transport, the MESSy-CLaMS 1.0 model version has limitations in the vertical transport and the mixing within the troposphere, thereby restricting the model's ability to represent convective transport accurately. Simulations in MESSy-CLaMS 1.0 model limited the rapid ascent of brominated VSLS and Br_y^{inorg} from the lower troposphere to the upper atmosphere. This restriction could result in decreased mixing ratios of brominated VSLS in the upper atmosphere.

5.2 MESSy-CLaMS 2.0

To address concerns about inadequate representation of vertical transport in MESSy-CLaMS 1.0 model, the improved model MESSy-CLaMS 2.0, described in Section 3.1.2, was employed. The new model improved the tropospheric mixing and convective updraft in the troposphere (Konopka et al., 2019, 2022). By utilizing an otherwise identical setup to the MESSy-CLaMS 1.0 model simulation, the MESSy-CLaMS 2.0 model introduces additional convection, resulting in vertical transport occurring more rapidly and air

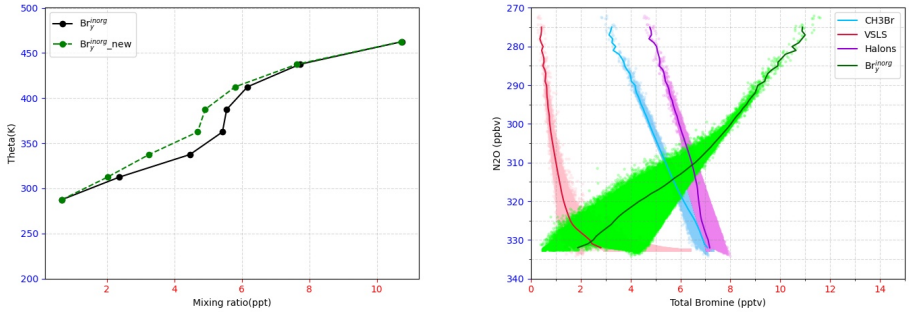

(a) (b)

Figure 5.4: Results of the simulation with Br_y^{inorg} removal reactions in CLaMS 1.0. (**a**) Comparison of CLaMS 1.0 parameterized simulation results (green line) with previous results lacking Br_y^{inorg} removal reactions (black line): average inorganic bromine mixing ratio profiles as a function of potential temperature for the 40°-60°N latitude region on August 20, 2019. (**b**) Relationship of mixing ratios between N_2O (ppb) and brominated species (ppt) across four distinct groups in parameterized simulations (with HBr/HOBr scavenging) in CLaMS 1.0 on July 20th: CH_3Br (blue), halons (purple), brominated VSLS (pink) and inorganic bromine (green).

masses becoming younger. Figure 5.5 shows the latitude-altitude cross section of zonal mean mixing ratios of long-lived CH_3Br and short-lived brominated VSLS modeled by MESSy-CLaMS 1.0 and 2.0 from August to October. In the tropical UTLS region, the average mixing ratios for CH_3Br and VSLS in CLaMS 1.0 exhibit lower values than those in CLaMS 2.0. This disparity can be attributed to the stronger and faster additional convection present in CLaMS 2.0. While in the extra-tropical region, the difference in simulation results between CLaMS 1.0 and 2.0 versions is small, as these regions are less affected by changes in the dynamics of convection transport.

The differences between the two simulations in terms of brominated VSLSs were further compared with the observational dataset based on the WISE and TACTS (Transport and Composition in the Upper Troposphere/Lowermost Stratosphere) campaigns (Keber et al., 2020). The TACTS campaign took place between August and September 2012 and covered the mid-latitudes of the Northern Hemisphere. Near the tropopause and approximately 40 K above it, the average mixing ratios of total bromine from VSLSs in both MESSy-CLaMS 1.0 and 2.0 (Figure 5.5c and Figure 5.5d) at 40°-60°N are smaller compared to observational data (as shown in Figure 5.6a). The mixing ratio of each bromi-

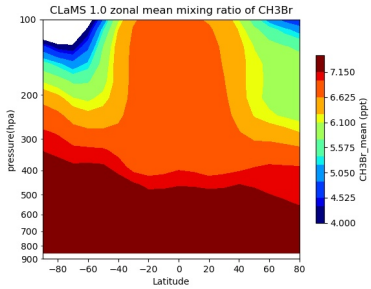

(a) CH_3Br in CLaMS 1.0

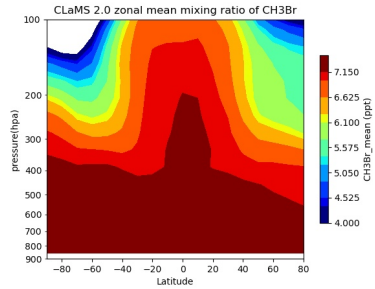

(b) CH_3Br in CLaMS 2.0

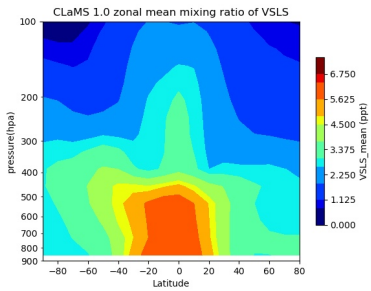

(c) VSLS in CLaMS 1.0

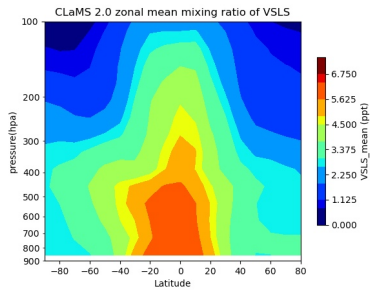

(d) VSLS in CLaMS 2.0

Figure 5.5: Altitude-latitude cross section of the zonal mean mixing ratios of CH_3Br and VSLS from August to October in MESSy-CLaMS 1.0 and 2.0. The Br species are summed up according to their Br atomicity. The left column are the simulation results in CLaMS 1.0 and right column show the simulation results in CLaMS 2.0.

nated VSLS varies with the potential temperature distance from the dynamic tropopause (derived from ERA5 data), denoted as $\Delta\theta = \theta - \theta_{\mathrm{Tropopause}}$ [K]. When compared to each of the brominated VSLS, the new simulations in MESSy-CLaMS 2.0 for each species are not in perfect agreement with observations, but both are slightly better than the earlier results in MESSy-CLaMS 1.0 and closer to the observations.

For a detailed comparison of the differences of brominated VSLS between MESSy-CLaMS 1.0 and 2.0, Table 5.1 shows the mean mixing ratios for each brominated VSLS in mid-latitudes from August to October for the two different versions of CLaMS modeled and observation data from Keber et al. (2020). The tropopause mixing ratios, delineated in Table 5.1, were derived within two distinct regions: from 10 K bin potential temperature below the tropopause to tropopause (TP) and at 40 K potential temperature above the tropopause (TP + 40 K). In these two regions, the mixing ratios of each of the brominated VSLSs in MESSy-CLaMS 2.0 show a faster increase in transport relative to the mean data in MESSy-CLaMS 1.0: the model results for CLaMS 2.0 show an increase of 0.01 ppt to 0.05 ppt within TP and 0.01 ppt within the region TP + 40 K, as compared to CLaMS 1.0. From CLaMS 1.0 to CLaMS 2.0, within TP, the simulated-to-observed ratios of $CHBr_3$, $CHBr_2Cl$ and $CHBrCl_2$ increased by 8.9%, 7.7% and 12.5%, respectively. The ratio of modeled to observed values of brominated VSLS within TP is at most 75.9% of the observed value in CLaMS 1.0, rising to 80.7% in CLaMS 2.0 (CH_2BrCl). Similarly, within TP + 40 K, the largest increase in ratios is for $CHBr_2Cl$ and $CHBr_3$, with increases of 16.7% and 9.1% from CLaMS 1.0 to CLaMS 2.0, respectively. It is evident that the simulation results in MESSy-CLaMS 2.0 are better than the previous results in MESSy-CLaMS 1.0.

After that step, various comparisons between the simulated mixing ratios of brominated VSLS in MESSy-CLaMS 2.0 and observations are displayed with respect to different latitudes and potential temperatures (shown in Figure 5.7, Figure 5.8 and Figure 5.9). Firstly, the comparison between observation data based on the autumn 2017 WISE campaign (Rotermund et al., 2021), and modeling results in CLaMS 2.0 for the summed up total bromine of CH_3Br, halons, brominated VSLS, and inorganic bromine components

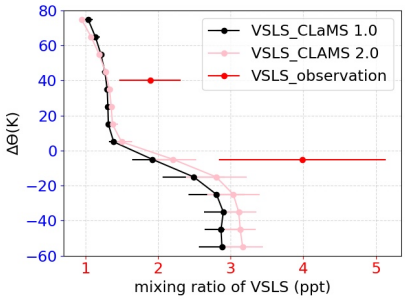

(a) Total bromine from VSLSs

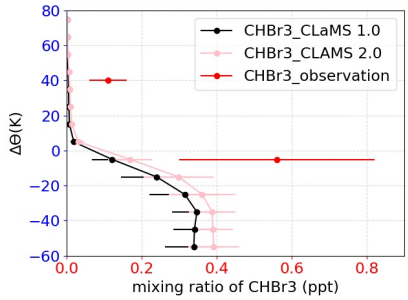

(b) $CHBr_3$

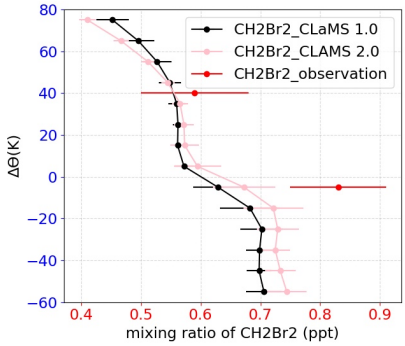

(c) CH_2Br_2

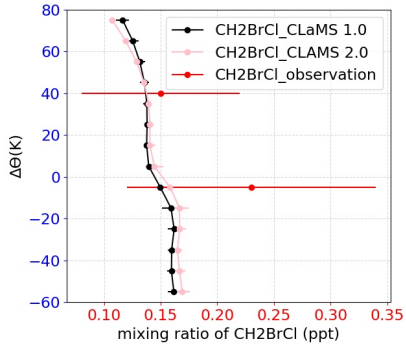

(d) CH_2BrCl

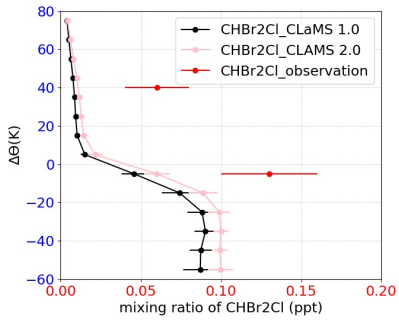

(e) $CHBr_2Cl$

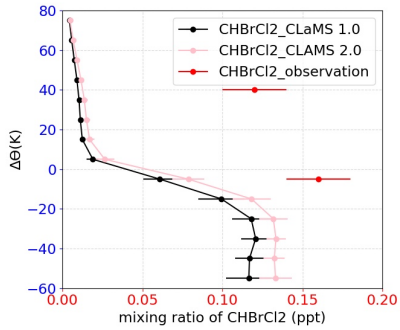

(f) $CHBrCl_2$

Figure 5.6: Simulations of brominated VSLS in CLaMS 1.0 (black line) and CLaMS 2.0 (pink line) with standard deviation compared with observation results (red line). Simulated mixing ratio has been averaged between 40°–60°N from August to October in 2019 as a function of potential temperature difference to the tropopause, $\Delta\theta = \theta - \theta_{\mathrm{Tropopause}}$ [K]. The mean observation values, along with error bars, were derived from the combined WISE and TACTS datasets, covering the latitude range of 40°-60°N during the period from August to October (Keber et al., 2020).

Averaged simulations and observations at tropopause (TP) and above (TP + 40 K)				
CLaMS 1.0	TP	Observation	TP + 40 K	Observation
$CHBr_3$	0.12 ± 0.05	0.56 ± 0.26	0.01 ± 0.00	0.11 ± 0.05
CH_2Br_2	0.63 ± 0.04	0.83 ± 0.08	0.57 ± 0.00	0.59 ± 0.09
CH_2BrCl	0.15 ± 0.01	0.23 ± 0.11	0.14 ± 0.00	0.15 ± 0.07
$CHBr_2Cl$	0.05 ± 0.10	0.13 ± 0.03	0.01 ± 0.01	0.06 ± 0.02
$CHBrCl_2$	0.06 ± 0.08	0.16 ± 0.02	0.01 ± 0.13	0.12 ± 0.02
CLaMS 2.0	TP	Observation	TP + 40 K	Observation
$CHBr_3$	0.17 ± 0.06	0.56 ± 0.26	0.02 ± 0.01	0.11 ± 0.05
CH_2Br_2	0.67 ± 0.05	0.83 ± 0.08	0.58 ± 0.03	0.59 ± 0.09
CH_2BrCl	0.16 ± 0.01	0.23 ± 0.11	0.14 ± 0.01	0.15 ± 0.07
$CHBr_2Cl$	0.06 ± 0.01	0.13 ± 0.03	0.02 ± 0.00	0.06 ± 0.02
$CHBrCl_2$	0.08 ± 0.01	0.16 ± 0.02	0.02 ± 0.00	0.12 ± 0.02

Table 5.1: Comparison with observed data on VSLS. Two different CLaMS versions (CLaMS 1.0 and CLaMS 2.0) simulated the mixing ratio of each brominated VSLS species from 10 K bin below tropopause (TP) to tropopause and 40 K above the tropopause (TP + 40 K), at latitudes of 40°-60°N from August to October in 2019. The observational data is from Keber et al. (2020), which combines WISE and TACTS datasets for the same latitude range and time period. All the values showing in the CLaMS part represent mean values ± standard deviation.

as a function of $\Delta\theta$, is shown in Figure 5.7. The mean total bromine in the upper troposphere and lower stratosphere (UTLS) region (between $\Delta\theta$ = -50 and 80 K) shows the simulation results in MESSy-CLaMS 2.0 are lower than the observational values obtained from the 2017 WISE campaign. For example, within $\Delta\theta$ = 0±5 K region, the averaged total bromine mixing ratio for the added brominated VSLSs are about 2 ppt less than the observational values.

To ensure consistency and avoid discrepancies due to variations in observation years (Keber et al., 2020), the simulation results in CLaMS 2.0 were compared with GhOST measurements collected during the SouthTRAC campaign in 2019, a time period encompassed by the model's simulation period. SouthTRAC is a measurement campaign

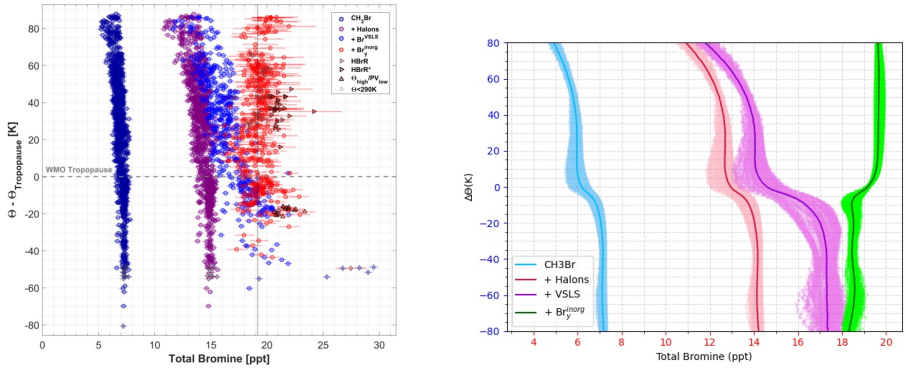

(a) (b)

Figure 5.7: Inferred total bromine as a function of potential temperature difference to the tropopause (TP), $\Delta\theta = \theta - \theta_{\text{Tropopause}}$ [K]. The brominated species are separated into four groups (CH_3Br, halons, brominated VSLSs and Br_y^{inorg}), which each group summed according to their atomicity. (**a**) The measurement data during WISE campaign in 2017 from Rotermund et al. (2021). (**b**) The simulation results in MESSy-CLaMS 2.0.

with the German aircraft HALO taking place in Argentina, which has been introduced in Section 3.2.1. To get a clearer picture of the overall trend in the simulation results, the one-to-one comparison between simulation results and GhOST observations at different latitudes is shown in Figure 5.8. The red line in the figure is a one-to-one correspondence line, and ideally, the data points should lie on this line, i.e., the simulation results are in perfect agreement with the observations. Then, to better examine the relationship between simulation results and observations, the best-fit line using linear regression was calculated, depicted as a solid green line in the figures. The linear regression estimation employed the ordinary least squares method. The coefficient of determination, denoted as R^2, is also presented in Figure 5.8, offering a quantitative indicator for the comparison.

The correlation analysis in Figure 5.8a reveals that the R^2 value for CH_2Br_2 is 0.616. The correlations between simulation results and observations exhibit some inconsistency, with the majority of data points symmetrically distributed on either side of the best-fit line. However, the presence of outliers, particularly those exceeding observational data in the Northern Hemisphere (NH), impact the overall correlation. In contrast, the simulated mixing ratios for $CHBr_3$ and $CHBr_2Cl$ are considerably lower than the GhOST measurement data, with R^2 values of 0.520 and 0.550, respectively. This indicates a notable discrep-

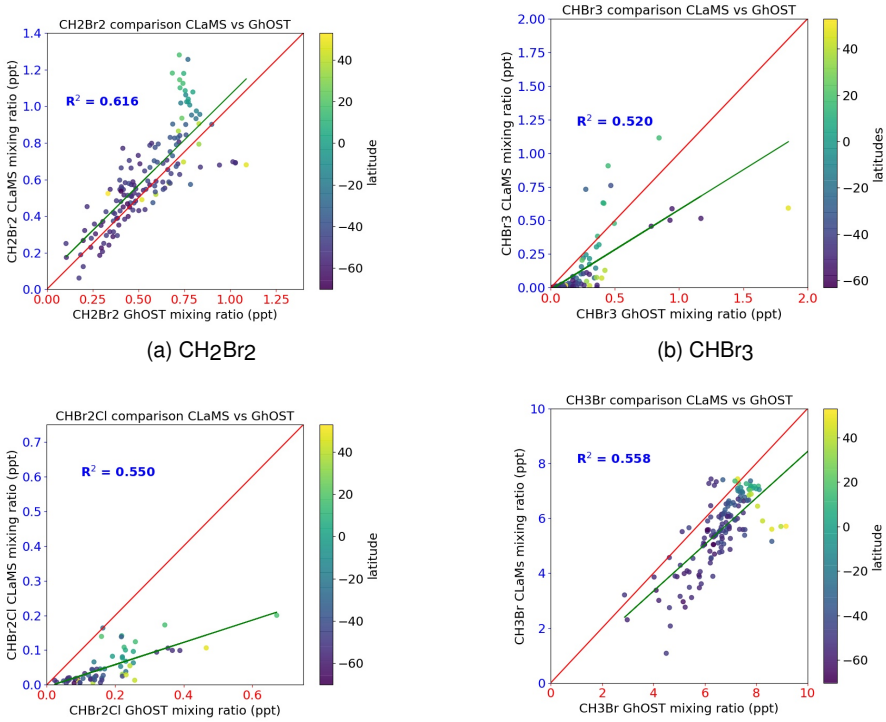

(a) CH_2Br_2 (b) $CHBr_3$

(c) $CHBr_2Cl$ (d) CH_3Br

Figure 5.8: One-by-one comparison of relationships between CLaMS 2.0 simulation and GhOST measurement data for the period from September to mid-November in 2019. The color code in the figures represents the latitude of observations, ranging from 48°N to 70°S. The red line is one-by-one line and green line through data points is the best-fit line.

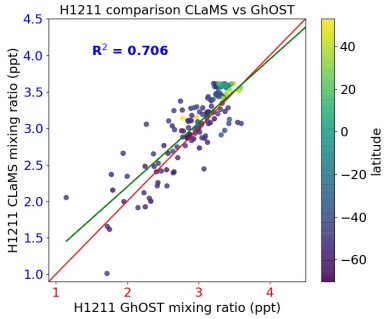

(e) H1211

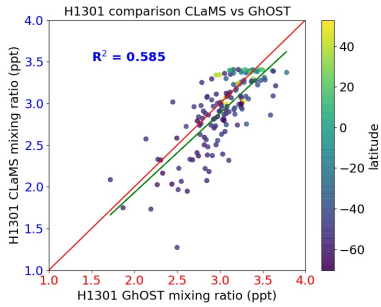

(f) H1301

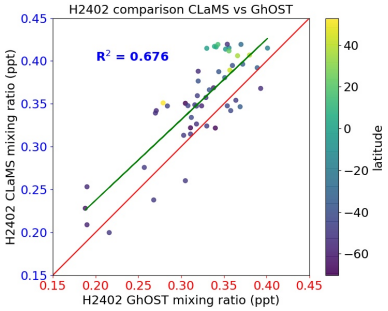

(g) H2402

Figure 5.8: (Cont.)

ancy between the model and observations for these species. For the long-lived species CH_3Br, the mixing ratios generally trend slightly lower than observations, resulting in an R^2 value of 0.558. In the case of halons, the coefficient of determination values for H2402, H1211, and H1301 are 0.676, 0.706, and 0.585, respectively. While the correlations are relatively higher for halons compared to other species, there are still variations that warrant attention. The observed disparities between simulation and observation across various brominated species highlight the necessity for a detailed comparison, given the lack of knowledge on the specific reasons behind these observed differences.

To delineate the disparity in detail, the CLaMS simulation results are compared with measurements across different vertical ranges. Figure 5.9 illustrates the mixing ratios of each brominated species for CLaMS simulation results and GhOST measurement data as a function of latitude. The data are represented by red circles and blue triangles, respectively, with two distinct altitude ranges considered: below the tropopause (325–350 K) and near the tropopause (350–375 K). For the very short-lived species $CHBr_3$ and $CHBr_2Cl$, the difference between simulation and observations is larger near the tropopause region than below it. Specifically, the absolute deviation between model simulation and observation (CLaMS-GhOST/GhOST) during the first three transfer flight latitude bands (30°S to 60°N) below the tropopause shows much lower values of about 23.8% and 34.9%, respectively. In contrast, near the tropopause the difference increases to about 56.1% and 74.3%, respectively. For latitude bands 30°S to 60°S, the absolute deviation in both layers is notably high, exceeding 80%. Concerning CH_2Br_2, the absolute deviation between 30°S to 60°S below the tropopause is approximately 2.67%, while at the higher near tropopause region, it is about 15.4%. For long-lived species such as CH_3Br, H1211, H2402, and H1301, the absolute deviation is much lower than that for the shorter-lifetime species. The mean deviation for H1211 and H1301 below tropopause and in the tropopause region is only about 0.19% and 4.07%, and 4.58% and 3.74%, respectively. Additionally, for CH_3Br and H2402, the mean deviation is also as low as about 18.55% and 2.46% below the tropopause, and 15.88% and 11.16% near the tropopause region, respectively.

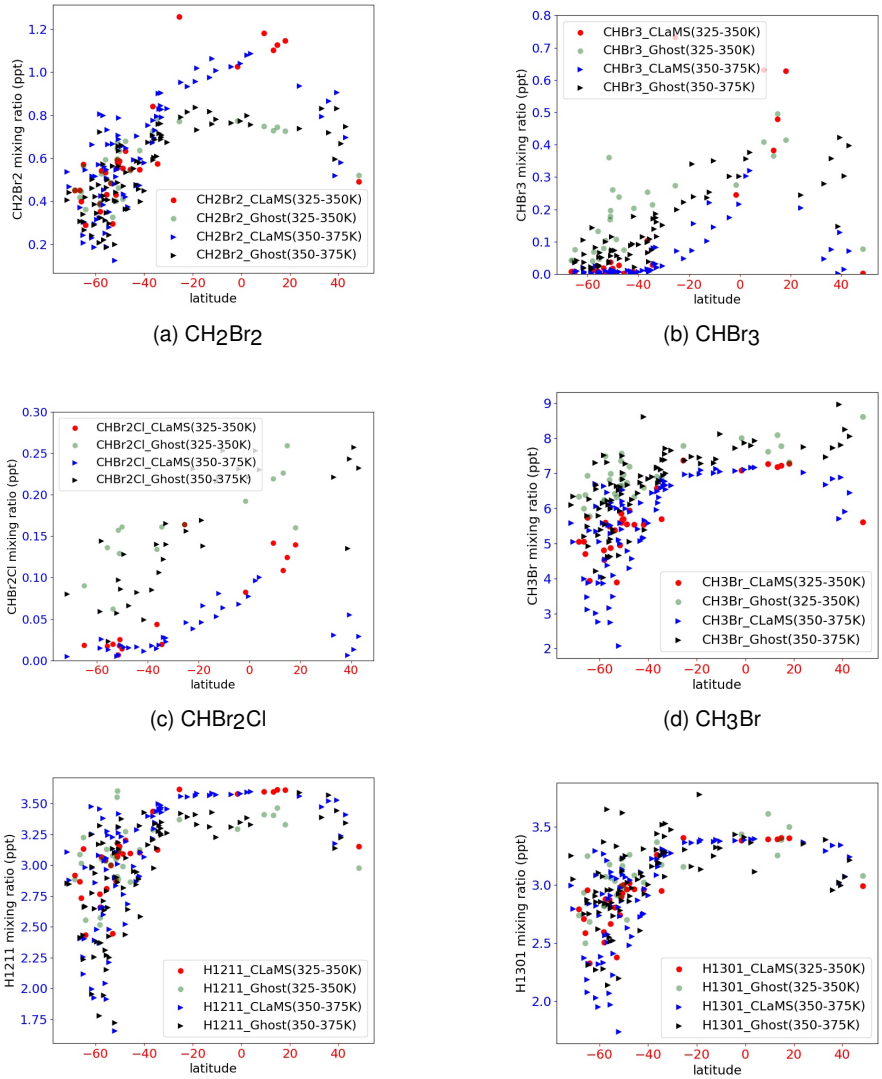

(a) CH_2Br_2 (b) $CHBr_3$

(c) $CHBr_2Cl$ (d) CH_3Br

(e) H1211 (f) H1301

Figure 5.9: Mixing ratios (ppt) from simulation results of CLaMS 2.0 and GhOST measurements from the SouthTRAC campaign as a function of latitude. The brominated species include short-lived CH_2Br_2, $CHBr_3$, $CHBr_2Cl$ and long-lived CH_3Br, H1301, H1211 and H2402. The available data points are separated into two different potential temperature ranges: CLaMS results in 325-350 K (red circles), GhOST data in 325-350 K (yellow circles), CLaMS results in 350-375 K (blue triangles) and GhOST data in 350-375 K (black triangles).

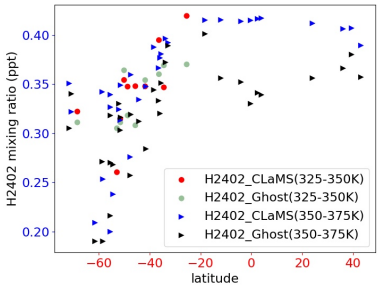

(g) H2402

Figure 5.9: (Cont.)

Since the deviation below the tropopause is lower than near the tropopause region (especially for shorter-lifetime species), a need for further optimization of upward transport processes can be suggested. It is also noteworthy that the shorter-lifetime species, $CHBr_3$ and $CHBr_2Cl$, which are more susceptible to source region influences, exhibit much higher deviations than longer-lifetime species. This discrepancy is most likely attributed to the oversimplified lower boundary conditions employed in the model. In contrast, actual lower boundary conditions are more intricate, and previous investigations into surface emission sources have shown significant differences between scenarios, which vary in continental, oceanic, and latitudinal geographical distribution (Warwick et al., 2006; Liang et al., 2010; Ordóñez et al., 2012). To test this hypothesis, the optimization of lower boundary conditions is imperative, and the subsequent chapters will present new simulation results.

Chapter 6

Optimization of the VSLS lower boundary

After incorporating the parameterization for the tropospheric sink of HOBr and HBr by cloud uptake, and accounting for the tropospheric mixing and convective updraft in the MESSy-CLaMS 2.0 model in the previous chapter, the differences between observations and the simulations suggest deficiencies in the used lower boundary. In this setting, changes were made to the lower boundary conditions, as detailed below. Section 6.1 illustrated the simulation with zonal symmetric lower boundary condition varying with season. In Section 6.2, model simulation was conducted with regionally resolved, seasonally varying lower boundary conditions. Moreover, the simulation in Section 6.3 incorporated the regionally resolved lower boundary with monthly dependence.

6.1 Zonally symmetric boundary with seasonal dependence

In the previous chapter, simulations that utilized lower boundary conditions, which were latitude-dependent and invariant with time, did not align well with the observations. For this reason, the simulations in this chapter involve time-dependent lower boundary conditions. The first lower boundary condition implemented in the model in this chapter is both zonally symmetric and seasonal dependent, derived from observations using climatology

data obtained from the American ATom and HIPPO campaigns (Jesswein et al., 2022). Further details regarding the climatology data from observations have been provided in Section 3.2.2.

The lower boundary values for halons are uniform across all latitudes, as derived from Meinshausen et al. (2020). For $CHBr_3$ and CH_2Br_2, the seasonal-dependent lower boundary data were obtained from climatology data at a pressure range of 729-800 hPa (Jesswein et al., 2022), corresponding to the lowest CLaMS model level with the hybrid potential temperature range (ζ) from 0 to about 140 K. To reduce noise associated with latitude, smoothing was applied at intervals of every 3 latitude values (30°). The seasonal distributions of $CHBrCl_2$ and $CHBr_2Cl$ were calculated based on the four ATom missions and assigned to the following four seasons: DJF (December, January and February), MAM (March, April and May), JJA (June, July and August), and SON (September, October and November). The value for CH_2BrCl was set to be 1.4 times that of $CHBrCl_2$, which was motivated by WISE GhOST data. Regarding CH_3Br, as its distribution from the ATom campaigns showed similarity across all seasons, the latitudinal mean lower boundary was calculated as the average of the four seasons. Furthermore, the smoothing values were weighted based on the total area of each 5° latitude range. Considering that with lower boundary value of 7.44 ppt, the majority of previous simulation results are lower than observations (as present in Figure 5.8d), the constructed zonally symmetric lower boundary was adjusted by increasing one ppt.

Based on data from Jesswein et al. (2022), Figure 6.1 depicts the lower boundary mixing ratios for the brominated very short-lived substances (VSLS) (CH_2Br_2, $CHBr_3$, CH_2BrCl, $CHBrCl_2$, $CHBr_2Cl$), and CH_3Br at different latitudes. The latitudes are binned in 20° intervals, ranging from 80°S to 80°N. The lower boundaries were compiled for four seasons: DJF (blue line); MAM (red line); JJA (green line); SON (black line). The distributions of the lower boundary for the brominated VSLS exhibit a general hemispheric symmetry in SON, with a weakening in the tropical region. In DJF, the lower boundary for both brominated VSLS is quite similar, decreasing from high to middle latitudes in the Southern Hemisphere (SH) and then increasing from about 30°S to 80°N, with values

in the Northern Hemisphere (NH) significantly higher than in the SH. The reason for this difference is the higher abundance of the coastal areas in the NH, which are considered to be important sources of brominated VSLS. As a result, the mixing ratio of these VSLS tends to be higher in the NH compared to the SH. In addition, during the winter months, decreased solar radiation and longer nights lead to reduced photolysis, which prolongs the atmospheric lifetime of VSLS, resulting in peak mixing ratios at the lower boundary in hemispheric winter. For CH_2Br_2, a clear seasonality is observed in both hemispheres, with an increased lower boundary in MAM and a decreased lower boundary in JJA from SH to NH. Similar mixing ratio distributions in MAM and JJA are observed for $CHBr_3$, with values in MAM slightly higher than in JJA.

Apart from the different lower boundary conditions, the initialization in the model remains identical with previous simulation. The values for CH_3Br, halons, and brominated VSLS were derived from correlations with N_2O of data provided by Rotermund et al. (personal communication). In contrast to previous simulations, this simulation use higher vertical ranges up to 2500 K potential temperature and more vertical levels (45 vertical levels). During the identical simulation time frame, the simulation incorporated the latitudinal averaged seasonal-dependent lower boundary as described above. The evaluation of the simulation results was performed using observations from the SouthTRAC campaign, which are presented in Figure 6.2 and Figure 6.3.

Figure 6.2 presents a one-by-one comparison between the CLaMS 2.0 simulation and SouthTRAC observations at different latitudes. For species with shorter lifetimes, such as CH_2Br_2, there were fewer outliers than in previous comparisons (Figure 5.8a), and the simulated coefficient of determination (R^2) is 0.8. This result demonstrates a better agreement compared to the simulation with a simple pattern (R^2 of 0.616) presented in Section 5.2. Similarly, for $CHBr_3$, the simulated coefficient of determination is 0.788, indicating a significantly closer agreement with the observations compared to the results presented in the previous Figure 5.8 (R^2 of 0.520). In the case of $CHBr_2Cl$, the simulation results exhibit a modest improvement with a slightly higher R^2 value of 0.571 than 0.550. However, the simulation results are still smaller than the observations. The sim-

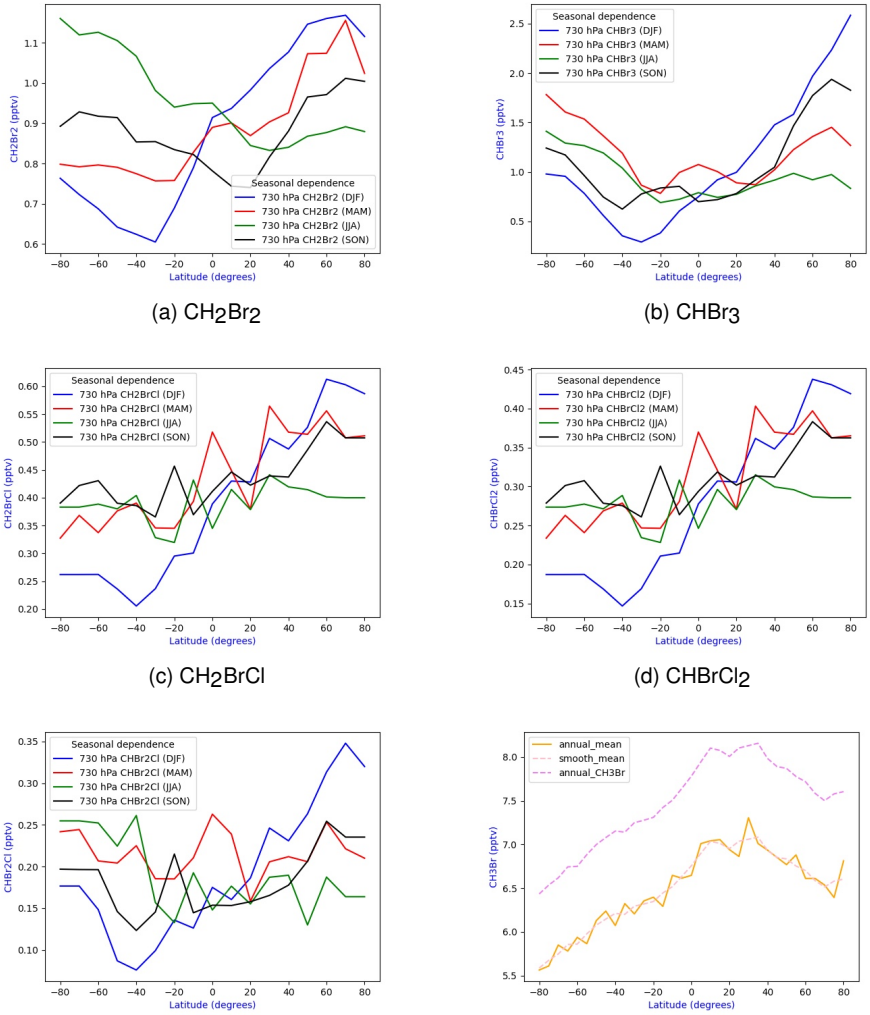

(a) CH_2Br_2 (b) $CHBr_3$

(c) CH_2BrCl (d) $CHBrCl_2$

(e) $CHBr_2Cl$ (f) CH_3Br

Figure 6.1: The seasonal-dependent zonally symmetric lower boundary for brominated VSLS, including CH_2Br_2, $CHBr_3$, $CHBr_2Cl$, CH_2BrCl and $CHBrCl_2$. Averaged mixing ratios of the lower boundary are displayed as a function of different latitudes from 80°S to 80°N. The lower boundary was shown in four different seasons: DJF (December, January and February) in the blue line, MAM (March, April and May) in the red line, JJA (June, July and August) in the green line, SON (September, October and November) in black line (Jesswein et al., 2022). The lower boundary of CH_3Br, calculated as the annual mean value plus one ppt, is indicated by the pink dashed line. The orange solid line is the annual mean value, and the orange dashed line is the weighted average smoothed value.

ulation results for longer lifetime species, CH_3Br and H1211, with R^2 values of 0.586 and 0.716, respectively, demonstrate slightly better agreement with the observed GhOST data than previous simulation shown in Figure 5.8, where R^2 values were 0.558 and 0.706, respectively. Given its longer lifetime, the lower boundary conditions for H1211 are relatively constant, while those of CH_3Br are more complex and vary with latitude. Consequently, simulating H1211 is comparatively easier, leading to a higher R^2 value compared to CH_3Br. However, for H1301 and H2402, the new simulations do not show improvement.

To conduct a detailed comparison of the relative difference between modeled (red circle) and GhOST data (blue circle), the mixing ratios of the modeled and observed results were displayed as a function of latitude in Figure 6.3. The mean relative difference ((CLaMS-GhOST)/GhOST), along with the standard deviation, was calculated. The CH_2Br_2 mixing ratios generally exhibit good agreement with observations, with a mean relative difference of -2.5$\pm$24%. The mean deviation percentage of the first three transfer flights' latitude bands (from 30°S to 60°N) is -1.4$\pm$25%, which is smaller than -7.5$\pm$15% along the scientific flights from 30°S to 80°S. However, the modeled $CHBr_3$ and $CHBr_2Cl$ results are consistently lower than the observations. Despite achieving a higher R^2 value of 0.788, the average relative difference of $CHBr_3$ remains substantial at -68.3$\pm$39%. This discrepancy is particularly pronounced during SH latitude bands (30°S to 80°S), where the average deviation reaches -77.9$\pm$31%, indicating a significantly lower level of agreement. Similar to $CHBr_2Cl$, the mean relative difference is as high as -70.8$\pm$19%. As for CH_3Br, despite having lower R^2 values (0.586), the overall distribution pattern aligns with observations, with an averaged relative difference of -13.5$\pm$15%. Concerning H2402, the mean relative difference is 8.5$\pm$11%, while in the 30°S to 60°N latitude bands, the relative difference is 12.5$\pm$8%, indicating a slightly higher mixing ratio than observations. Both H1211 and H1301 show low relative differences, with values of 4.6$\pm$10% and -3.7$\pm$10%, respectively.

Overall, this simulation represents an improvement by employing the zonally symmetric seasonal lower boundaries with mixing ratio based on climatology data. The sim-

ulation results utilizing zonally symmetric seasonal lower boundaries exhibit enhanced concordance with observational data compared to simulations employing simplistic lower boundary conditions. However, there are still discrepancies between the simulation results and the observed data at different latitude ranges. These disparities may stem from inaccuracies in the determination of the lower boundary, chemical reaction rates, or the atmospheric transport processes. This underscores the imperative need for a comprehensive exploration of potential causative factors to further elucidate the observed discrepancies.

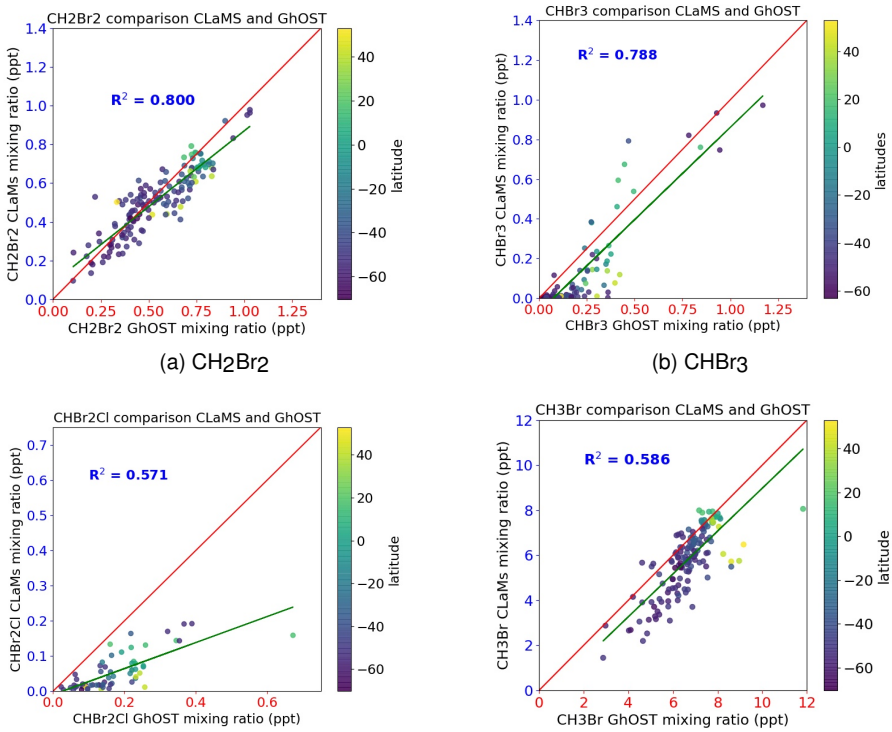

(a) CH_2Br_2 (b) $CHBr_3$

(c) $CHBr_2Cl$ (d) CH_3Br

Figure 6.2: One-by-one comparison of relationships between model simulation with new seasonal latitudinal averaged lower boundary and the GhOST measurement data from Septembre to mid-November in 2019. The color code of the figures represents the different latitude ranges from 48°N to 70°S. The red line represents the one-by-one line, and the green line is the best-fit line.

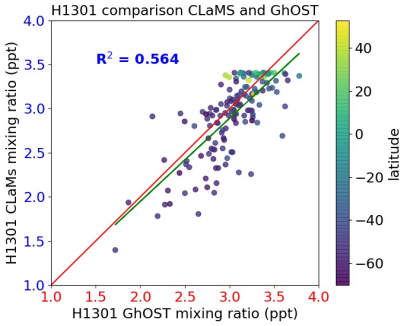

(e) H1301

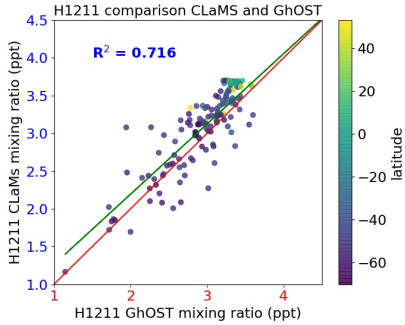

(f) H1211

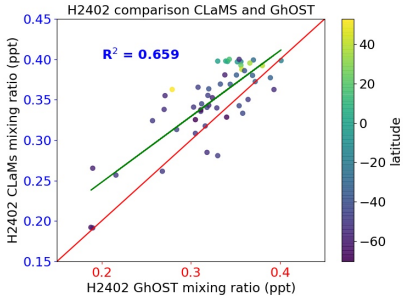

(g) H2402

Figure 6.2: (Cont.)

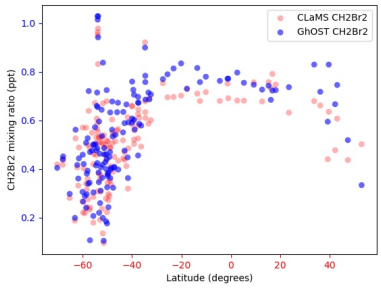

(a) CH_2Br_2

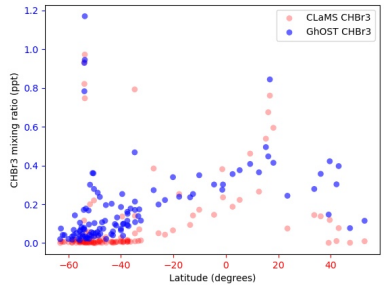

(b) $CHBr_3$

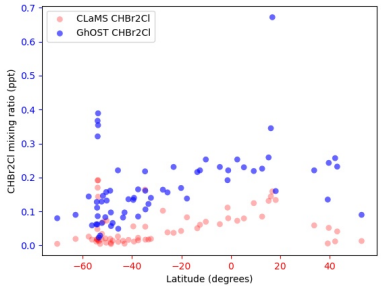

(c) $CHBr_2Cl$

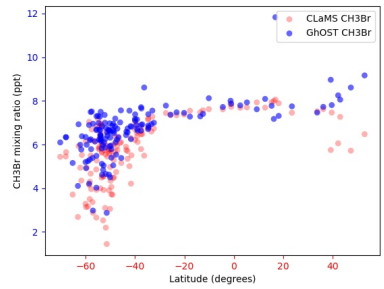

(d) CH_3Br

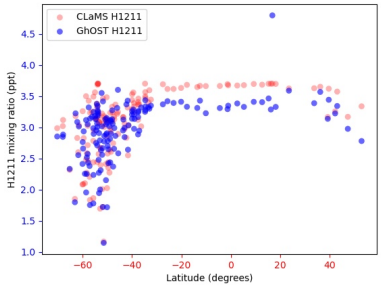

(e) H1211

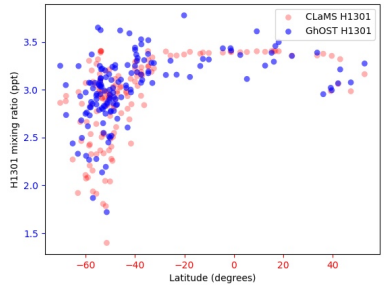

(f) H1301

Figure 6.3: Mixing ratios of different brominated species compared one-by-one between CLaMS simulation and GhOST observations at different latitudes (from 48°N to 70°S) during the SouthTRAC campaign (from September to mid-November in 2019). The pink circle represents simulated mixing ratio and blue circle represents the observation data from GhOST.

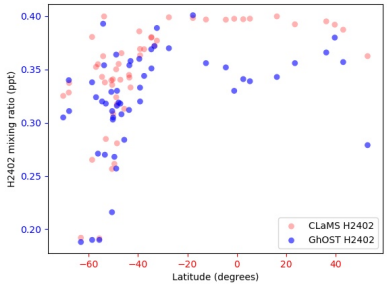

(g) H2402

Figure 6.3: (Cont.)

6.1.1 Investigation using surface origin tracers

A method utilized in this study involves the application of so-called surface origin tracers. These tracers are artificial model quantities initialized with a value of 1 in a specific source region at the surface and set to 0 elsewhere. They undergo the identical advection and mixing processes in the model as compounds. This approach enables the tracing of the origin regions of any air parcel within the model. In this context, this method was applied to investigate whether specific discrepancies between observations and the simulation may correspond to specific source regions. The values of individual surface origin tracer gives the fraction of air masses originating from the specific region, thereby indicating the distinct contributions of each source region. Here, the surface emission tracers are released within 32 pre-defined geographic locations in the boundary layer, as shown in Figure 6.4a (Vogel et al., 2015; Lauther et al., 2022). Moreover, the representative name of each emission tracer is listed in Figure 6.4b.

A simulation for surface origin tracer was conducted using the MESSy-CLaMS 2.0 model, employing meteorological data, horizontal, and vertical resolutions identical to those in the previous simulation. In order to investigate the proportion of transported air masses originating from various source regions within the boundary layer, these tracers were interpolated to the flight path of the first transfer flight that encompasses both the Northern and Southern Hemisphere. The first transfer flight departs from Oberpfaffenhofen (Germany) to Rio Grande (Argentina) over three consecutive flights from 6 to 9

September 2019.

To facilitate a clearer visualization of changes in the contribution from each surface origin tracer and to adjust the lower boundary values for different latitude range accordingly, Figure 6.5 displays the cumulative percentages of the nine most abundant surface origin tracers along the first transfer flight track latitudes and longitudes for potential temperatures between 340 and 360 K. With different colors denoting various surface origin tracers from different surface regions, the percentages in this figure reveal the major contributions of air masses near the tropopause originating from various source regions.

Figure 6.5, derived from CLaMS 2.0 results, indicates that the Asian region (Southeast Asia (SEA), Warm Pool (Wpool), and Bay of Bengal (BoB)), along with the Tropical Western Pacific (TWP), serve as significant sources, contributing predominantly (approximately with an average of 20%) to the tropopause region in the Southern Hemisphere (SH) and mid-latitudes in the Northern Hemisphere (NH). Additionally, in the SH, the Tropical Eastern Pacific (TEP) and Central America (CAM) also contribute relatively large portions, about 8% and 4.5%, respectively, to air masses in the mid-latitudes within the tropopause region. In the NH tropical tropopause region, the predominant fraction of air masses originates from the Northern Africa (NAF) lower boundary, contributing up to approximately 60%, as indicated in the gray portion. While other surface origin tracers make relatively smaller contributions in the tropical tropopause region (e.g., TAO (Tropical Atlantic) and TWP (Tropical Western Pacific) averagely contribute about 5.7% and 5.4%, respectively). It is noteworthy that in the CLaMS 1.0 model, the contribution of the same source region, NAF, where upward transport occurs without additional convection, contributes a smaller portion to the tropical tropopause region in the NH, as illustrated in Figure B.1. This indicates that there is more upward transport in the nearby region, potentially attributed to deep convection. For a few other surface origin tracers, where the contributions differ, the definitions vary from those in Figure 6.4; additional details are provided in Appendix B.

As explained above, the surface origin tracers are used to optimize the boundary conditions by adjusting the lower boundary mixing ratio. To achieve this, the discrepancy

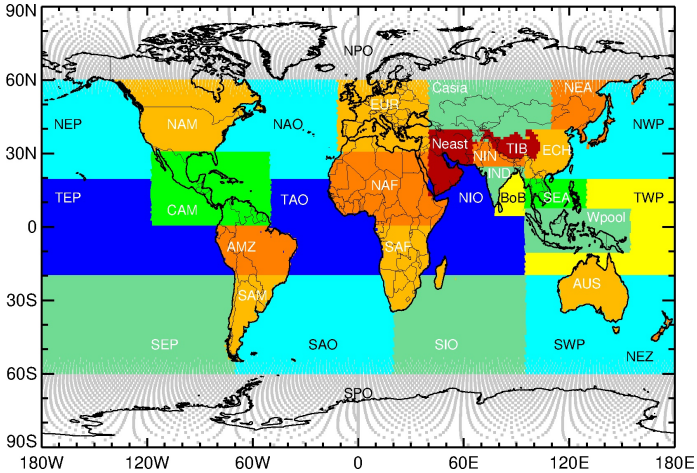

(a) Locations of surface origin tracers

NAF	Northern Africa	TAO	Tropical Atlantic Ocean	Wpool	Warm Pool
NEP	Northern Eastern Pacific	IND	Indian Subcontinent	CAM	Central America
NAM	Northern America	AMZ	Amazonia	NEZ	New Zeeland
NAO	Northern Atlantic Ocean	SIO	Southern Indian Ocean	TIB	Tibetan Plateau
EUR	Europe	BoB	Bay of Bengal	NIO	Northern Indian Ocean
Casia	Central Asia	SAM	Southern America	NIN	Northern India
NWP	Northern Western Pacific	SEA	Southeast Asia	NPO	North Polar Region
NEA	Northern Eastern Asia	SWP	Southern Western Pacific	SPO	South Polar Region
TEP	Tropical Eastern Pacific	SEP	Southern Eastern Pacific		
ECH	Eastern China	AUS	Australia		
TWP	Tropical Western Pacific	SAF	Southern Africa		
Neast	Near East	SAO	Southern Atlantic Ocean		

(b) List of emission tracers

Figure 6.4: Global geographical location of lower boundary emission sources in the CLaMS 2.0 model simulation (**a**). The list of emission tracers names corresponding to their abbreviations (**b**).

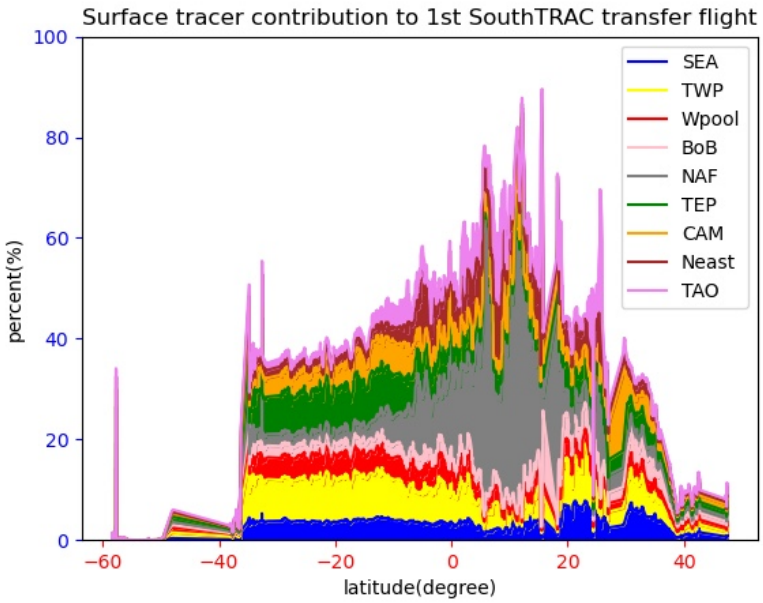

Figure 6.5: The accumulation of the abundant contributed percentages from different emission sources at different latitudes for the first transfer flight near the tropopause region (340-360 K). Different colors represent different emission tracers, and the name for each abbreviated emission tracer is listed in Figure 6.4b.

between observed and simulated mixing ratios was correlated with the different contributions from surface origin regions. Figure 6.6 displays cross-sectional latitude mixing ratios for brominated species, including $CHBr_3$, CH_2Br_2, $CHBr_2Cl$, CH_3Br, H1211, and H1301, during the first transfer flight. These data correspond to those displayed in Figure 6.5. The graph presents both simulation results (represented by pink circles) and observations from GhOST (depicted as blue circles) between 340-360 K potential temperatures.

It is evident that at the potential temperature level of 340-360 K, the differences in mixing ratios between the model and observations varied across different latitudes for each species. Several factors could contribute to these discrepancies, including inaccuracies in the estimation of the transport process, initialization values, and the distribution of the lower boundary. The initialization data were obtained through correlations with N_2O from Rotermund et al. (personal communication). To isolate a single variable, we also assume the correctness of the transport process. Given that the lower boundary setup for simulation is derived from climatology data, which is better than the previous lower boundary as shown in Figure 5.1, it is used for initialized lower boundary. Ideally, the simulation results should demonstrate good agreement with observations or, at the very least, exhibit the same deviation trend. As shown in Figure 6.6, for certain species, such as $CHBr_2Cl$, clear positive and negative biases exist, with all modeled results being lower than observations. In this case, if only considering the lower boundary, the comparison results indicate that the lower boundary values are underestimated. To optimize the simulation results, the lower boundary should be increased based on the varying latitudinal contributions from different surface origin tracers, as shown in Figure 6.5. However, for other species, the positive and negative discrepancies differ within various latitude ranges. For instance, simulated mixing ratios of CH_2Br_2 are slightly smaller than observations in both the SH tropical region and higher latitudes (about 60°S). In SH mid-latitudes (about 40°S) and the NH tropical region, a few points of mixing ratios in the model are higher than observations. Specifically, in certain latitude ranges, positive and negative discrepancies are intermixed, as observed in CH_3Br and H1301 from 40°S to 20°N, and $CHBr_3$ in the NH

tropical region. These discrepancies cannot be easily optimized by increasing or decreasing the percentage contribution of the surface origin tracer alone. Henceforth, subsequent to the removal of the less impact initialization factor, ambiguity persists regarding the two remaining causative factors contributing to these disparities, namely, whether originating from lower boundary sources or influenced by atmospheric transport.

6.1.2 Age of air selection

As previously elucidated, the discrepancies between observations and model results could arise from inaccuracies in boundary mixing ratios or the transport process, involving variations in advection and mixing. A parameter can be employed to diagnose the transport process in the model is the mean age of air (AOA), signifying the average duration taken for air parcels to traverse from the troposphere to a designated location in the stratosphere. The mean age of air was also calculated for observations using sulfur hexafluoride (SF_6) data. SF_6 is a long-lived trace gas with a measured positive growth rate in the troposphere and is commonly used to estimate the mean age of air. The SF_6 tropospheric reference data for the age of air calculation were obtained from the MLO datasets (Mauna Loa, Hawaii, USA (19.5N, 155.6W), including flask measurements and in situ measurements) provided by Wagenhäuser et al. (2023). In the following, we only consider pairs of observations and simulations of the same air mass, ensuring the age of air for both observations and modeling is less than six months. The calculation approach can be summarized with the following formula (Volk et al., 1997; Fritsch et al., 2020):

$$x(t_1) = a(t_1 - t_0)^2 + b(t_1 - t_0) + c, \tag{6.1}$$

$$\Gamma = b/(2 * a) - C_1 - \sqrt{(b/2 * a - C_1)^2 + \tau^2 - b * \tau/a} \tag{6.2}$$

Equation 6.1 is the quadratic fit to the reference time series from 2004 to 2019, $x(t_1)$ is the mixing ratio of the SF_6 at t_1, t_0 is the reference time, January 1st 2019. This calculation yields the polynomial coefficients, a = 0.003958, b = 0.36284, and c = 9.93405. Applying the observed values of SF_6 and these coefficients to the equation 6.1, we can

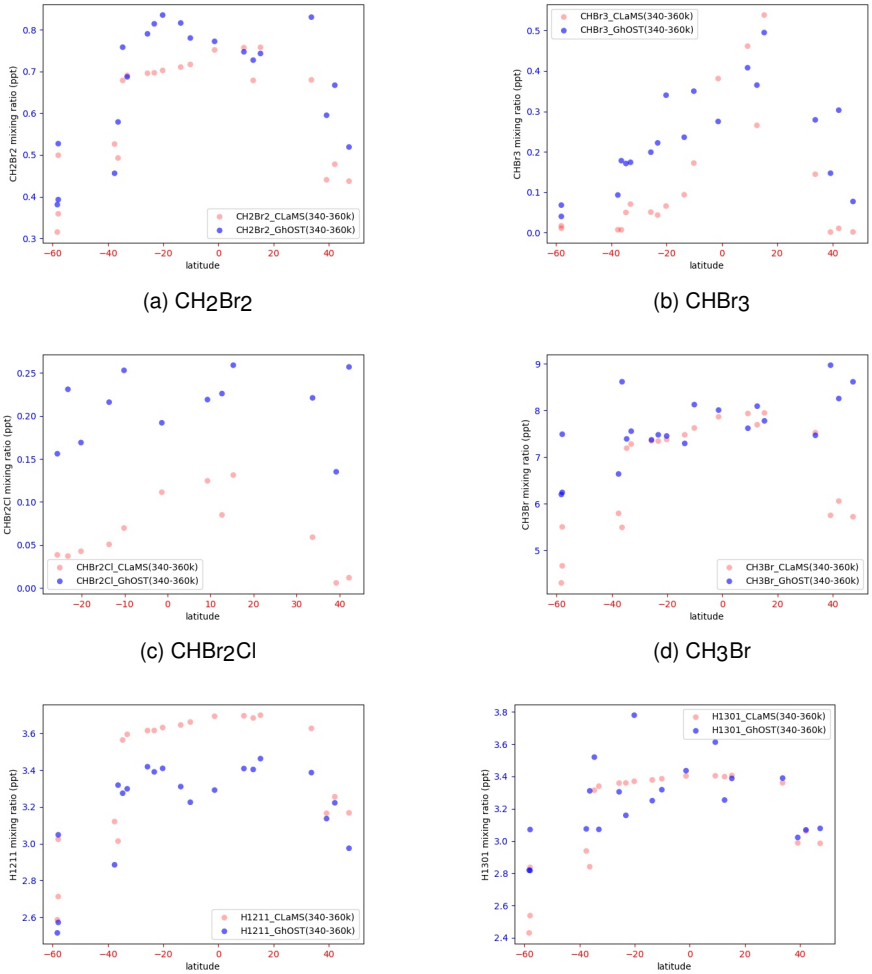

(a) CH_2Br_2 (b) $CHBr_3$

(c) $CHBr_2Cl$ (d) CH_3Br

(e) H1211 (f) H1301

Figure 6.6: The comparison of mixing ratios between CLaMS simulation and GhOST observation at different latitudes during the first transfer flight. The available observation data include $CHBr_3$, CH_2Br_2, $CHBr_2Cl$, CH_3Br, H1211 and H1301. The pink circle represents the simulation results and blue circle represents the observation data.

determine the transit time, denoted as t, from the time corresponding to the fitted function t_1 to the reference time t_0. As shown in equation 6.2, to derive the mean age of air Γ, the coefficients a, b, and c values were substituted to the formula. τ is the lag time between t and the time that observed date with the same concentration of SF_6. C_1 is the ratio of first and second moments of the age spectrum, and the value 1.25, which is somewhat based on model data, and to some degree still an uncertain parameter (Volk et al., 1997; Fritsch et al., 2020). Where the offset time $(t - t_0)$ is the time from the reference time (1 January 1980) to the simulation time.

Figure 6.7 illustrates the comparison of the calculated age of air between all South-TRAC observations and simulations from September to November. The color bar corresponds to potential temperature. The one-to-one line (red line) and the best-fit line (green line) align closely. This suggests that, for the majority of air masses, there is no noticeable systematic offset in the age of air. Nevertheless, outliers near the tropopause suggest that certain observed air masses are older than their simulated counterparts.

The age of air serves as a metric to quantify the transport process. Given the short lifetime of the very short-lived species (VSLS) being less than six months, the subsequent analysis focuses on comparisons where the age of air in both observations and simulations, as well as the age difference between them, is constrained to less than half a year. Employing this approach guarantees a closer alignment between observations and simulations concerning bromine-containing VSLS.

Surface origin tracers were employed to investigate the contributing regions of different species within the selected air masses. Considering the strong sensitivity, the age of air difference was combined with mixing ratio differences to identify the lower boundary contributions along each trajectory. The mixing ratio of the older air masses transported to the Upper Troposphere and Lower Stratosphere (UTLS) is expected to be lower due to oxidation or photolysis of the VSLS during transport. Put simply, if the modeled mixing ratio exceeds the observations, the modeled age of air is likely younger than the observed age of air. Conversely, if the modeled mixing ratio is lower than observations, the modeled age of air is expected to be older. However, there are cases where the modeled

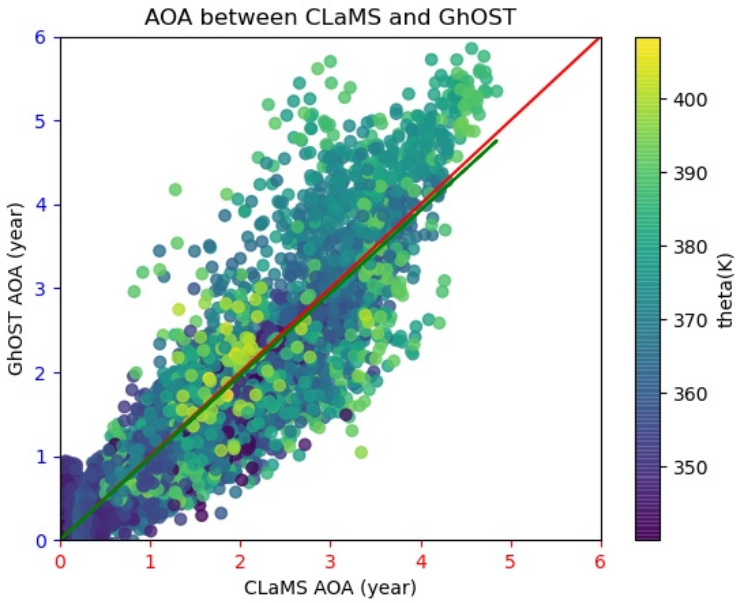

Figure 6.7: Comparison of age of air (AOA) between model simulation and GhOST observation. The color code represents different potential temperatures (theta in Kelvin), the one-by-one line shown in red, and the best-fit line in green.

age of air is younger than observed, but the mixing ratio is lower, or vice versa. These discrepancies are most likely caused by inaccuracies in estimating lower boundary conditions. In the following, we focus on the cases where the lower boundary conditions likely present a problem. Specifically, instances where the model's age of air surpasses the observed age of air, concomitant with a diminished mixing ratios relative to the observed value, are excluded. Also, exclusions encompass situations where the model's age of air is younger than the observed counterpart, accompanied by mixing ratios surpassing the observed value. Consequently, if the age of air and mixing ratios from model simulations both exceed the observed values, this discrepancy implies that the model has set the lower boundary values higher than the actual values, deviating from the expected levels. Conversely, suppose the age of air and mixing ratios from model results are both lower than the observations, implying that the lower boundary condition of the model simulation is low and should be increased appropriately. Ideally, the lower boundary for the same contributing surface region could be adjusted accordingly based on the difference in mixing ratios between the observed and modeled results.

After comparing the mixing ratio and age of air between observed and modeled values for each air parcel, our attention turns to their tracer origin. These air masses are characterized by the contribution of each source region, with dominant regions identified where contributions exceed 20%. Any bias in one of these regions is anticipated to affect all air parcels dominated by that region similarly. We analyze air parcels exhibiting differences and plot them at observation locations showing negative or positive differences in $CHBr_3$ and CH_2Br_2. Figure 6.8 shows the subset of mixing ratio difference between observation and simulations for two brominated VSLSs, CH_2Br_2 and $CHBr_3$. This subset encompasses flight trajectories that were selected with the age of air being younger than the observed values. The color code indicates the value of the mixing ratio deviation from the observed value, and the positions of the circles show the corresponding positions of the flight path. Regarding CH_2Br_2 and $CHBr_3$ originating from regions like CAM (Central America), AMZ (Amazonia), SAM (Southern America), and NIN (Northern India), the majority of the origin tracers have young air and negative mixing ratio biases, meaning the

simulation results are lower than anticipated. Such negative deviations suggest that, for these position's air parcels, the lower boundary conditions set for these surface regions within the model simulation are underestimated and need to be increased.

However, concerning specific surface emission sources, such as $CHBr_3$ originating from the SAM (Southern America) (Figure 6.8e) and CH_2Br_2 originating from the NIN (Northern India) region (Figure 6.8f), there is a scarcity of data points available, making it challenging to achieve convincing adjustments. Moreover, some air parcels originating from the same emission sources exhibit more complicated results: positive mixing ratio differences occur when the age of air is older. At the same time, negative deviations arise when the age of air is younger than the observation. For instance, as illustrated in Figure 6.9, the mixing ratios difference for $CHBr_3$ and CH_2Br_2, from air parcels originating in the NAF (Northern Africa) and the TAO (Tropical Atlantic Ocean) regions, shows both positive and negative deviations corresponding to the older and younger age of air. This suggests that in the modeling results, the mixing ratios of air masses originating from the same surface emission source vary, with some being higher and others lower compared to the observed data. As a result, the adjustment of lower boundary values in this source region should both increases and decreases at the same time, which is not feasible and would not result in a significant improvement.

Therefore, relying solely on these surface origin tracers is not sufficient to optimize and derive the best estimates of the lower boundary conditions. For enhanced precision, the surface source regions would need to be further refined into smaller subregions. However, this refinement may lead to a reduction in statistical significance, making it challenging to achieve meaningful results.

6.2 Regionally resolved boundary with seasonal dependence

Considering meaningful results could not be achieved with the surface origin tracers setup, in this section, an investigation was conducted to identify specific regions of lower boundary discrepancies by employing back-trajectories from the observation locations. In principle, each point of observation-simulation difference could be traced back to a sur-

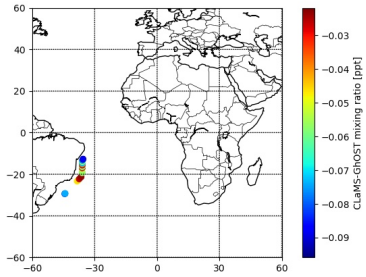

(a) $CHBr_3$ from AMZ

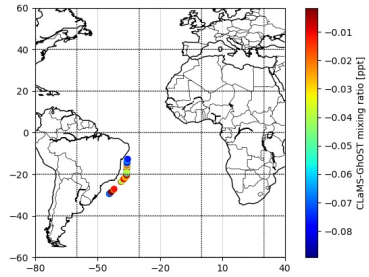

(b) CH_2Br_2 from AMZ

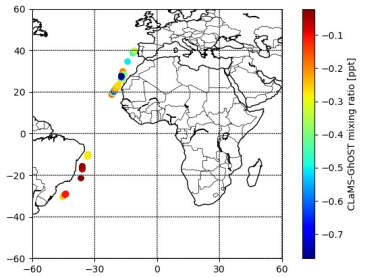

(c) $CHBr_3$ from CAM

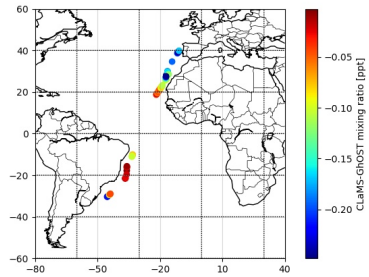

(d) CH_2Br_2 from CAM

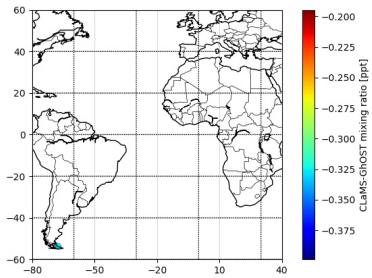

(e) $CHBr_3$ from SAM

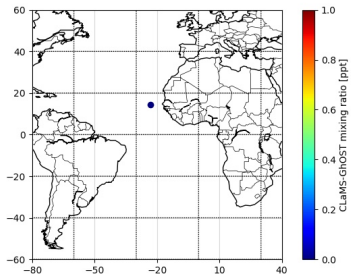

(f) CH_2Br_2 from NIN

Figure 6.8: Air masses from different emission sources with younger age of air for CLaMS simulation than that of GhOST observation: $CHBr_3$ from AMZ (Amazonia), CAM (Central America) and SAM (Southern America); CH_2Br_2 from AMZ (Amazonia), CAM (Central America), NIN (Northern India). The color code in the figure represents the difference between the mixing ratios of CLaMS and GhOST (CLaMS - GhOST in ppt).

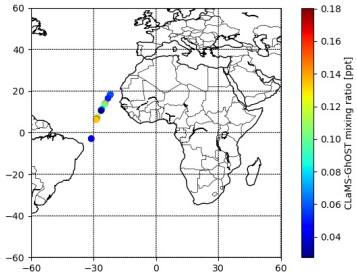

(a) Higher $CHBr_3$ from NAF

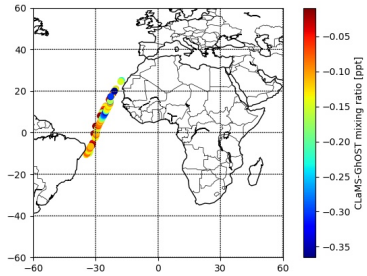

(b) Lower $CHBr_3$ from NAF

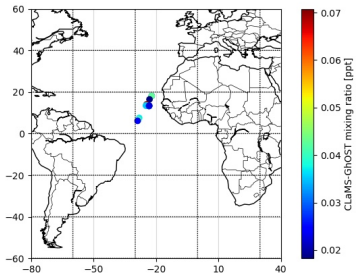

(c) Higher CH_2Br_2 from NAF

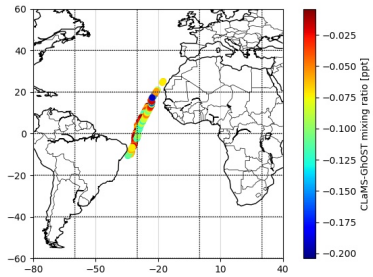

(d) Lower CH_2Br_2 from NAF

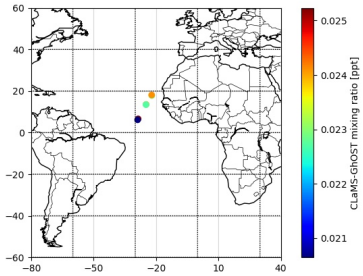

(e) Higher CH_2Br_2 from TAO

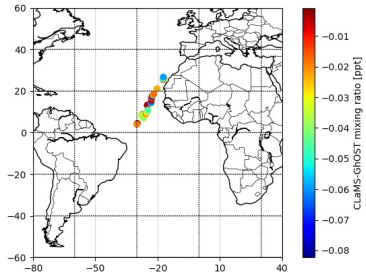

(f) Lower CH_2Br_2 from TAO

Figure 6.9: Air masses from different emission sources with both negative and positive mixing ratio difference between model and observations for $CHBr_3$ and CH_2Br_2. $CHBr_3$ from NAF (Northern Africa) with older age of air and higher mixing ratios than observations (**a**); with younger age of air and lower mixing ratios than observations (**b**). CH_2Br_2 with older age of air and higher mixing ratios than observations from NAF (Northern Africa) (**c**) and TAO (Tropical Atlantic Ocean) (**e**); with younger age of air and lower mixing ratios than observations from NAF (Northern Africa) (**d**) and TAO (Tropical Atlantic Ocean) (**f**). The color code in the figure represents the difference between the mixing ratios of CLaMS and GhOST (CLaMS - GhOST in ppt).

face location. However, for this, the possible fast updraft caused by convection needs to be taken into account. Therefore, another method was used in the following to assess the likely occurrence of deep convection by analyzing backward trajectories with Convective Available Potential Energy (CAPE) (Konopka et al., 2019). From this section on, this thesis focuses on the two most significant and influential brominated VSLS, the $CHBr_3$ and CH_2Br_2. Due to the short lifetime of these species, the calculated backward trajectory time for each flight track was limited to four months.

6.2.1 Backward trajectory analysis including convection

The parameter CAPE (convective available potential energy) derived from ERA5 reanalysis data quantifies the instability of the air. Higher CAPE values indicate greater instability, which can lead to convection. By combining backward trajectory analysis and CAPE, it becomes possible to trace air masses back to their surface locations, by locating potential regions of convective updrafts.

Once the likelihood of convection has been determined, the subsequent step involves distinguishing between weak and strong convection by assessing the anticipated altitude that the air mass is likely to reach. To accomplish this, the parameter θ_{max} (units in K) is defined that is the maximum potential temperature that air masses could attain, reflecting their convective energy. The calculation equation from Konopka et al. (2019) for θ_{max} is shown as follows:

$$\theta_{max} = \theta + (L_v * SH * \theta)/(c_p * temp) \tag{6.3}$$

Where θ represents the potential temperature of the air parcels at the lower boundary. The parameters L_v and c_p obtained from Konopka et al. (2019) represent the specific latent heat for evaporation (with a value of L_v=$2.26 * 10^6 Jkg^{-1}$), and the specific heat at constant pressure (c_p=$1005J/(Kg)$ in dry air), respectively. SH is the specific humidity of air parcels at the lower boundary and $temp$ represents the temperature in air parcels at the lower boundary, approximating the saturation temperature here. This equation represents the maximum convection energy, with the parameter θ_{max} calculated based on the presence of water vapor within the air mass in the boundary layer. These water vapor

during condensation process release latent heat, enabling the air masses to ascend from the lower boundary layer to the upper atmosphere.

Therefore, starting from each observation point, backward trajectories were calculated using the TRAJ module of CLaMS model and driven by wind field of ERA5 reanalysis data. Each air parcel was then traced back along the backward trajectory to the lower boundary layer by up to four months. To assess the possibility of deep convection, the applied threshold value of CAPE is set to 3000 J/Kg (Hoffmann et al., 2023), i.e., the CAPE of the air mass exceeds 3000 J/Kg. And the θ_{max} value should be higher than the potential temperature of the trajectory height. For example, as shown in Figure 6.10a and Figure 6.10b, the illuminated areas in these two plots represent areas where the CAPE value and θ_{max} are high enough. Within the area characterized by high values of both parameters, the air parcels have the potential to ascend to higher altitudes and be transported along the trajectory to the observation location.

At the same time, along the calculated backward trajectory, air parcels that do not undergo deep convection were traced back to their sources at the lower boundary, where ζ is less than 140 K, corresponding to the lowest level of the used CLaMS model setup. This method successfully traced approximately one-third of the observed air masses back to lower boundary sources, including both deep convection and long-range transport within a four-month period. The remaining two-thirds of the air masses persisted in the atmosphere above the lower boundary layer.

Given the assumption of a consistent difference in mixing ratios between CLaMS and GhOST observations (expressed as a percentage of GhOST observations) during the transport process, the lower boundary conditions can be adapted in accordance with this identical percentage difference in mixing ratios. Figure 6.11a and 6.11b show the global distribution of the mixing ratio percentage difference for $CHBr_3$ and CH_2Br_2 within the lower boundary layer. Circles in the figure indicate air masses experiencing deep convection, and triangles indicate air masses affected only by long-range transport.

Due to the existence of two different transport pathways, the contribution of air masses containing $CHBr_3$ and CH_2Br_2 from various lower boundary sources to the upper troposphere-

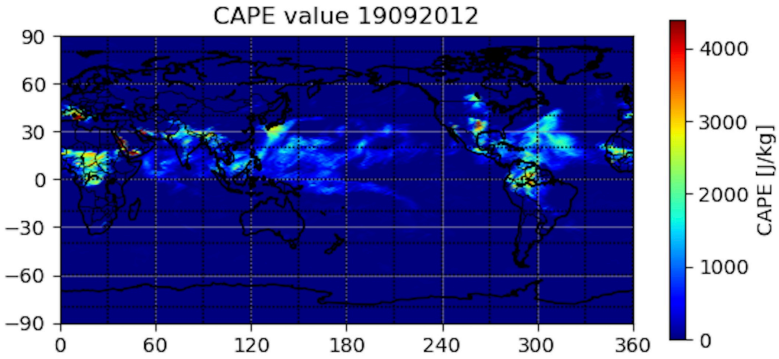

(a) CAPE

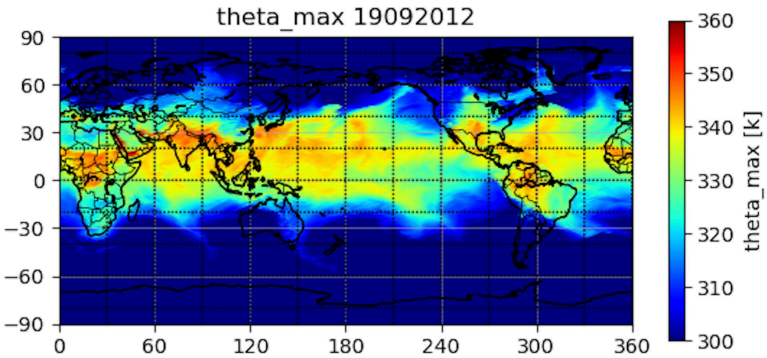

(b) θ_{max}

Figure 6.10: The global regions susceptible to deep convection. The parameter values utilized on September 20th, 2019, encompassing CAPE (convective available potential energy in J/kg) (**a**), derived from ECMWF ERA5 reanalysis data, and the calculated θ_{max} (maximum potential temperature the air masses could attain in K) (**b**).

lower stratosphere (UTLS) exhibits variability. About 42% of the composition of CH_2Br_2 and $CHBr_3$ is attributed to deep convection, while approximately 58% is contributed by long-range transport. When considering different source regions, the majority of air masses in the lower boundary sources are from the tropics (30°N to 30°S), consistent with the region characterized by biologically active and efficient transport. It is noteworthy that, concerning CH_2Br_2 and $CHBr_3$, despite the observations occurring in the Southern Hemisphere, a significant fraction of the air masses in the UTLS region can be traced back to the Asian region, most probably due to the influence of the Asian monsoon (Randel et al., 2010; Ploeger et al., 2017).

Therefore, to further adjust the lower boundary values, an examination of the deviation percentage in the figure reveals that the lower boundary mixing ratio for $CHBr_3$ in the Asian region, along with the Tropical Pacific region, is anticipated to undergo a substantial increase. Specifically, air masses originating from the Tropical Pacific (including TEP and TWP), Southeast Asia (SEA), and the Bay of Bengal (BoB) exhibit a notable negative deviation, which primarily contributes to the underestimation of the lower boundary. However, across tropical land areas and the tropical Atlantic Ocean (ranging from 120°W to 60°E), the mixing ratio deviations display a mixture of negative and positive values. In this situation, achieving precise adaptation solely based on the specific mixing ratio deviations of the air masses and their complicated distributions is challenging. Therefore, refinement of the lower boundary source regions becomes essential.

In summary, for young air masses (less than 4 months old) containing CH_2Br_2 and $CHBr_3$, particularly in the end of monsoon season in September/October 2019, approximately 42% of these air masses undergo transportation through deep convection from lower boundary sources to the Upper Troposphere and Lower Stratosphere (UTLS) region. Among them, about one-third originate from lower boundary sources in southern Asia and Northern African continent. The modeling results emphasize the significant influence of two primary deep convective source regions, namely southern Asia and continental Northern Africa, on the bromine chemical composition of the UTLS region over the Southern Pacific and Southern Atlantic Oceans. Considering to achieve further adap-

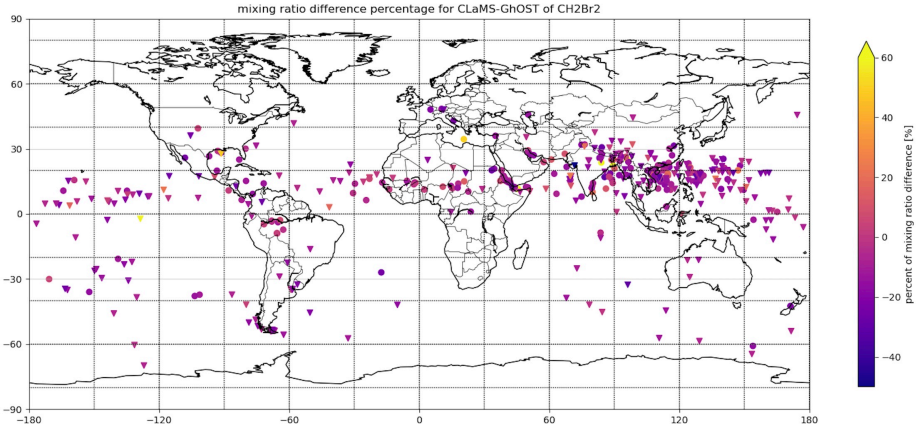

(a) CH_2Br_2

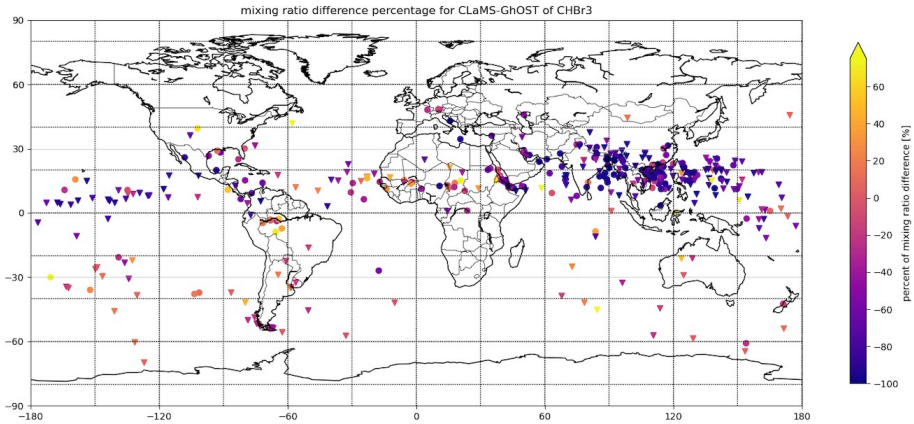

(b) $CHBr_3$

Figure 6.11: The global distribution of air parcels for CH_2Br_2 (**a**) and $CHBr_3$ (**b**) traced back to lower boundary layer, including air parcels by long-range transport (triangles) and by deep convection (circles). The color code represent the relative difference between CLaMS simulation versus GhOST observations ((CLaMS-GhOST)/GhOST).

tation, the lower boundary geographic refinement needs to be applied and introduced in the following section.

6.2.2 Construction of a regionally resolved boundary

In the preliminary iteration of global lower boundary adaptation, the new boundary is defined by the previous partitioning of origin tracers, as illustrated in Figure 6.4. For each region displayed in Figure 6.4, the lower boundary mixing ratio was adjusted by a scaling factor that derived from observation. Initially, the relative difference between the observed and simulated upper atmospheric mixing ratio was calculated for each air parcel, and identified their origin sources at the lower boundary. Subsequently, if we assume that the relative difference between observation and simulation remains consistent down to ground level, we then scaled up the lower boundary mixing ratio using this relative difference.

Given the restricted traced-back time of 4 months, air parcels were positioned in the boundary layer from May to October, depending on the specific date. Since there was no data available for the springtime, regional lower boundary values were constructed according to the values outlined in Section 6.1. For sparsely located air parcels from October to January of the following year, in regions lacking data points, mixing ratios were also calculated by referencing the seasonal lower boundary values from Section 6.1. These calculated air parcels were then categorized into four distinct time period: from 15 January to 15 April, from 15 April to 15 July, from 15 July to 15 October, and from 15 October to 15 January of the following year. During each time period, for every distinct region, the median air parcel mixing ratio within that geographical area was calculated, representing the lower boundary values for their respective regions.

Due to the significant variations in mixing ratios among air parcels in specific regions and the absence of adequately comparable data in certain areas, some of the surface regions used before (Figure 6.4) were separated into further sub-regions. Specifically, due to the limited number of air parcels in the back trajectory map and the shared regional characteristics of Northern Asian regions, including NIN (Northern India), TIB (Tibetan

Plateau), and ECH (Eastern China), these three areas were combined into a new region to minimize errors, as shown in Figure 6.12 (purple region). Additionally, at the southern end of SAM (Southern America), the coastal region with distinctly concentrated air parcels has been specifically delineated, shown as pink region in Figure 6.12.

Figure 6.13 and Figure 6.14 illustrate the global maps of mixing ratios distribution of CH_2Br_2 and $CHBr_3$ in four different seasons, constructed using the method described before. Similar to the lower boundary derived from zonally symmetric observational data illustrated in Appendix C by Jesswein et al. (2022), there is discernible seasonality in the lower boundary of both CH_2Br_2 and $CHBr_3$. The mixing ratios of CH_2Br_2 from mid-January to mid-July are higher in the mid- and low latitudes of the Northern Hemisphere (NH), compared to the corresponding latitude bands in the Southern Hemisphere (SH). Conversely, between mid-July and mid-January of the following year, there is a general decrease in mixing ratios within the Northern mid- and low latitudes, with the highest mixing ratios distributed across mid-latitude oceans (e.g., South Australia Ocean (SAO) and the Southwest Pacific Ocean (SPO)) and on some continents (Southern America (SAM)) in the SH. Regarding $CHBr_3$, the global distribution of mixing ratios clearly exhibits seasonality across both oceanic and continental regions, with lower values from mid-January to mid-April and from mid-October to mid-January in the following year of the following year, and higher values occurring from mid-April to mid-October. This seasonality suggests that the release of $CHBr_3$, mainly by macroalgae, reaches a maximum in summer is most likely due to enhanced light stimulation.

In addition to seasonality, the estimated lower boundary for $CHBr_3$ also displays dependence on the source region. Mixing ratios in specific areas notably exhibit significantly high values within the latitude range of 20°S to 40°N, encompassing parts of the Asian region and the Pacific Ocean. The variability in regional dependence may result from differing transport pathways in distinct regions. Air parcels undergoing longer-range transport and having a longer tracing back time to the ground demonstrate elevated mixing ratios. However, some regions exhibit anomalously high values, particularly pronounced during the summer. For instance, during the summer, mixing ratios in the Bay of Ben-

gal (BoB), the combined region of Northern India, Tibetan Plateau, and Eastern China (NIN+TIB+ECH), as well as the Near East (Neast) region, experience significant elevations, reaching values as high as 10.89 ppt, 8.90 ppt, and 7.37 ppt, respectively. These much higher-than-expected mixing ratios are a result of scaling up the differences to the surface sources using the previously mentioned method. Therefore, there may be some scaled-up differences, potentially attributed to transport errors in the trajectory or unconsidered mixing. This indicates a limitation in the calculation process when the backward trajectory time is much longer than the species' lifetime. As there are no indications of $CHBr_3$ observations of this magnitude, the so-constructed boundary seems not realistic.

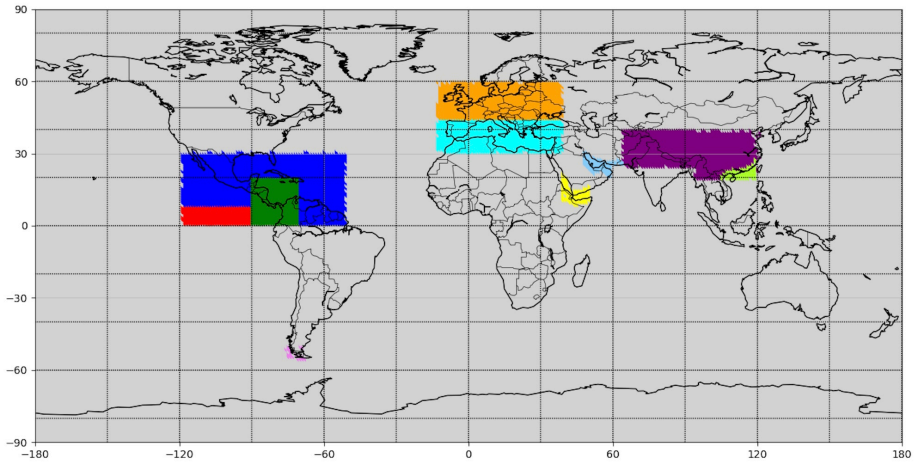

Figure 6.12: The refined global geographical distribution of lower boundary sources, delineating distinctive sections within Central America (CAM) into three segments (blue, red, and green); Europe into two parts (orange and cyan); and consolidating the Tibetan Plateau (TIB), Northern India (NIN), and Eastern China (ECH) into a unified zone (purple). Additionally, distinct regions are designated for coastline 1 (pink), coastline 2 (light blue), coastline 3 (yellow), and coastline 4 (light green).

Nevertheless, a six-month simulation was carried out employing the aforementioned seasonal lower boundary from May to November 2019 to facilitate further adaptation. The simulation results were compared with GhOST observations for a detailed one-by-one comparison, as depicted in Figure 6.15. These figures present scatter plots depicting the relationships between the CLaMS simulation results and GhOST observations for the

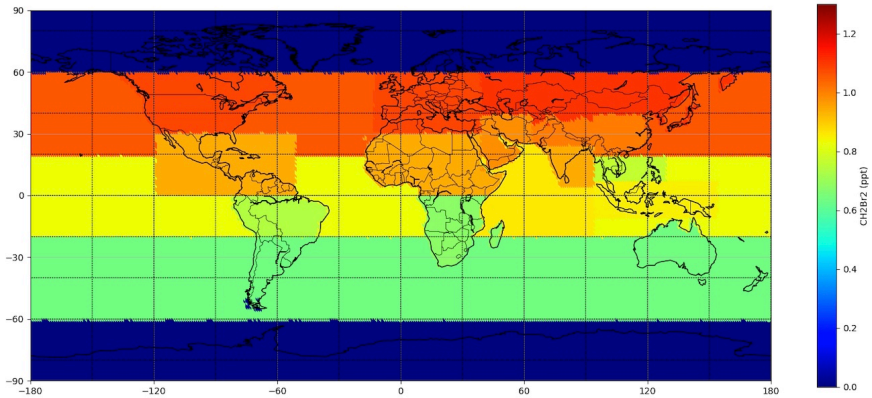

(a) CH_2Br_2 from mid-January to mid-April

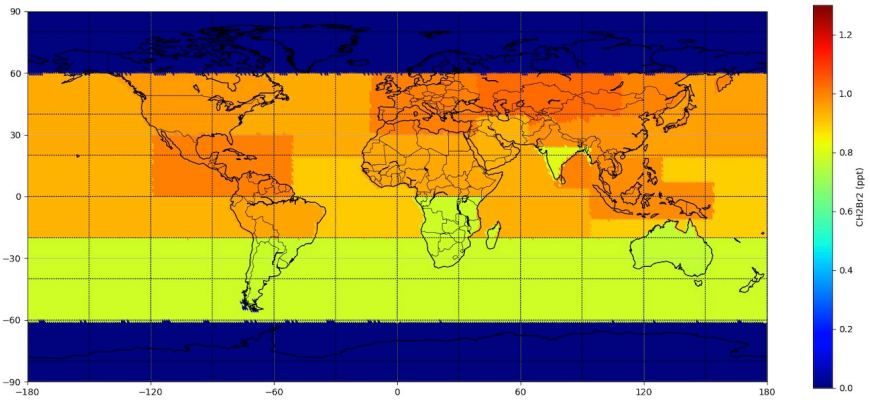

(b) CH_2Br_2 from mid-April to mid-July

Figure 6.13: Global distributions of lower boundary conditions for CH_2Br_2 in four different time period: (**a**) from mid-January to mid-April; (**b**) from mid-April to mid-July; (**c**) from mid-July to mid-October; (**d**) from mid-October to mid-January.

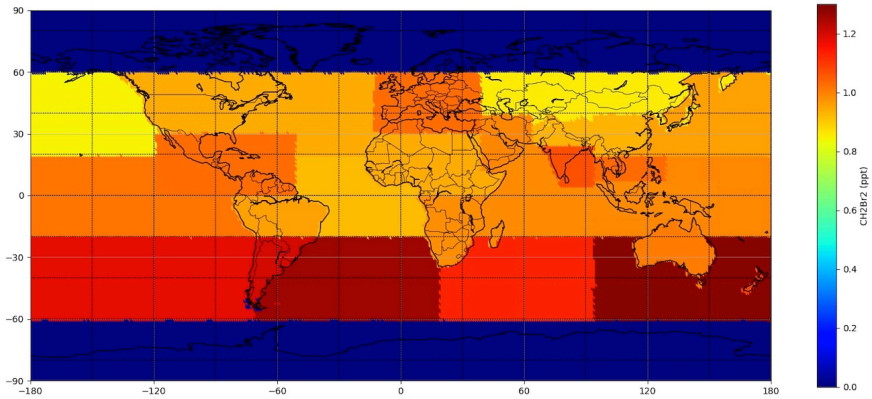

(c) CH_2Br_2 from mid-July to mid-October

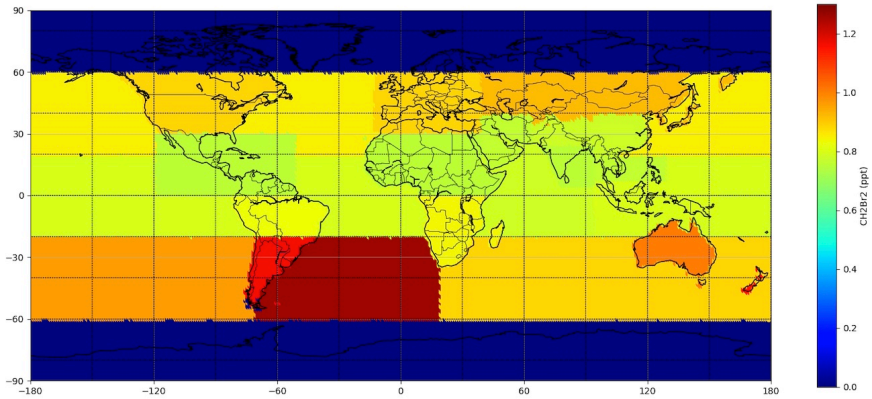

(d) CH_2Br_2 from mid-October to mid-January

Figure 6.13: (Cont.)

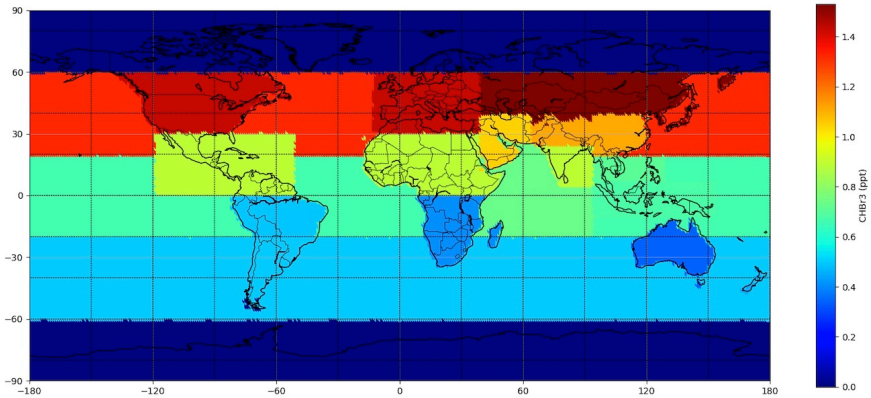

(a) CHBr3 from mid-January to mid-April

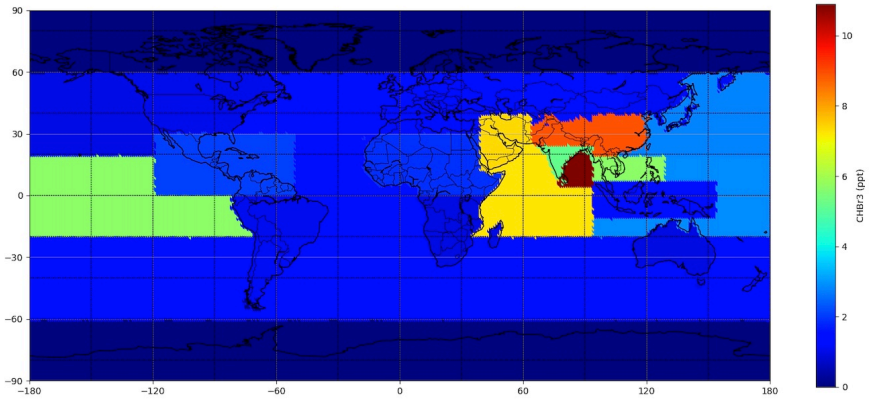

(b) CHBr3 from mid-April to mid-July

Figure 6.14: Same to Fig. 6.13, but for CHBr3. The scale of the four colour bars is different. Specifically, from mid-April to mid-July and from mid-April to mid-July, the scale of the mixing ratio is above 10 ppt and 4 ppt respectively.

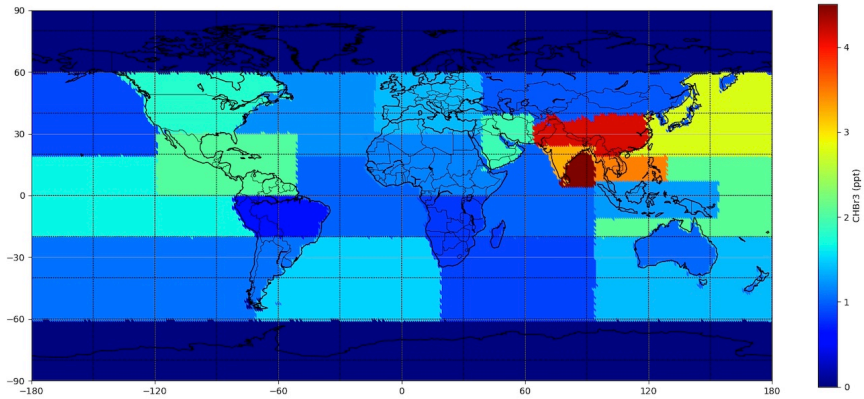

(c) CHBr3 from mid-April to mid-July

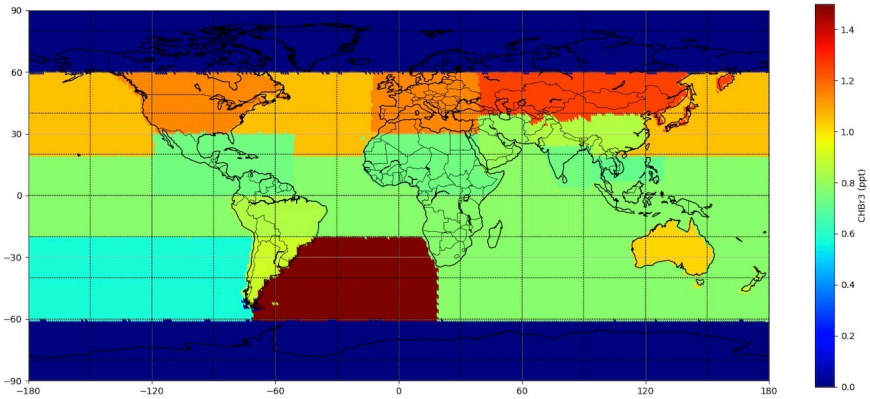

(d) CHBr3 from mid-October to mid-January

Figure 6.14: (Cont.)

mixing ratios of $CHBr_3$ and CH_2Br_2 at different latitudes.

In the comparative data set covering the period from September to November 2019, the correlation between the modeled and observed CH_2Br_2 (highlighted by the green best-fit line) is assessed against the 1:1 reference line (indicated by the red line), yielding a calculated coefficient of determination of 0.655. This value is smaller than the previously calculated 0.8 in a simulation with zonally symmetric lower boundary, suggesting that the seasonal dependent regionally resolved lower boundary does not perform better than the zonally symmetric lower boundary, contrary to expectations. Moreover, the average relative difference is 2.8±34%, which is larger than the relative difference of 2.5±24% in the previous simulation. This indicates good agreement but not an improvement over the previous simulation with zonally symmetric seasonal lower boundary. Furthermore, there is a slightly higher occurrence of data anomalies in the Southern Hemisphere (SH) (with a mean relative difference of 4.7±37%) compared to the previous results using the zonally symmetric lower boundary (where the relative difference value was -1.4±25%). This result suggests that the simulation results using this seasonal dependent regionally resolved lower boundary do not provide a more accurate representation of the global distribution in the Upper Troposphere and Lower Stratosphere (UTLS) during the SouthTRAC campaign.

For $CHBr_3$, which has a relatively short lifetime of about 1 month, it exhibits a higher sensitivity to variations in lower boundary conditions. Figure 6.15b depicts that the majority of data points fall below the 1:1 line. This positioning, along with the placement of the best-fit line beneath the 1:1 reference line, suggests that, in general, most CLaMS simulation results are smaller than the corresponding observations. This could potentially be associated with an underestimated representation of the majority of surface lower boundary conditions. Concerning the outliers positioned above the 1:1 line, their occurrence might be attributed to an overestimation of exceptionally high values in particular lower boundary regions, such as the Bay of Bengal (BoB). In comparison to the earlier simulation utilizing zonally symmetric seasonal lower boundaries (depicted in Figure 6.2b), the current coefficient of determination value is 0.641, which is smaller than the value

of 0.788 in the previous simulation with a zonally symmetric lower boundary, indicating a lower correlation. While comparing the mean relative difference, the percentage values for $CHBr_3$ simulation with a seasonal dependent regionally resolved lower boundary equal -56.5±44%, which is lower than the -68.3±39% observed in the simulation with a zonally symmetric lower boundary, indicating a better agreement. Additionally, a higher incidence of data anomalies is observed in the Southern Hemisphere (SH) (from 30°S to 80°S) with a relative difference of up to -65.5±37%, compared to the simulation results within the first three transfer flights' latitude bands (from 30°S to 60°N) with -29.6±50%. This suggests that the simulation with a seasonal dependent regionally resolved lower boundary aligns better with observations, and the fitted R^2 is influenced by anomalies, most likely occurring in the SH from 30°S to 80°S latitude bands.

To enhance the statistics in the model validation, we compare the model results with observation data. In particular, the climatology data by Jesswein et al. (2022), which incorporates data from the TOGA instrument and sampler data from the Atom mission, seems well suited. Zonal mean results for simulations and observations are provided in pressure and latitude cross sections in Figure 6.16 and 6.17. The available data were categorized by season (MAM (March, April, May), JJA (June, July, August) and SON (September, October, November)). The data were segmented into 10° latitude intervals ranging from 90°S to 80°N. In the vertical dimension, pressures were binned between 900 and 100 hPa, partitioned into 20 distinct bins. With rising altitude and correspondingly lower pressure, the bin size declines logarithmically.

Figure 6.16 and 6.17 show the distributions of CH_2Br_2 and $CHBr_3$ obtained from both the climatology data and the model simulation results with a seasonal dependent regionally resolved lower boundary. The model results for the distribution of CH_2Br_2 exhibit a general lack of agreement with the observations. In the tropopause region, there is a significant bias between model data and observations in different seasons. For example, there is an overestimation in the tropical tropopause region during MAM, with differences from observations reaching up to about 0.3 ppt, while in SON, there is an underestimation with values being up to 0.3 ppt lower. This may arise from a possible inaccurate

seasonal representation in tropical lower boundary. Also, in the lower troposphere, the observations reveal a notable increase in values during MAM and SON at high latitudes in the Northern Hemisphere (NH). However, the model fails to capture this seasonality in the NH and depicts smaller values. One could argue that the climatology data is predominantly derived from the NH, which has more coastal regions serving as the primary source of brominated VSLS and exhibits higher mixing ratios in the NH. In contrast, the model simulation is based on aircraft measurements from the SouthTRAC campaign, primarily conducted in the Southern Hemisphere, and therefore depicts smaller mixing ratios in the lower troposphere in NH. The same pattern is shown for $CHBr_3$, which model result displays smaller mixing ratios in the lower troposphere at higher latitudes in the NH during SON. During MAM and JJA, the mixing ratios for $CHBr_3$ in tropical regions exhibit higher values compared to climatology data in both the lower troposphere and the higher tropopause region. This could be attributed to the overestimation in certain tropical regions in the lower boundary.

In summary, the comparisons between the model simulations using a seasonal dependent regionally resolved lower boundary and observations from the SouthTRAC data, as well as comparisons with climatological data, indicate a lack of good agreement. The discrepancies between models and observations for $CHBr_3$ and CH_2Br_2 are likely attributed to inaccuracies in the lower boundary estimates. Specifically, accurately capturing the rapid variations in the lower boundary mixing ratios poses a significant challenge, particularly in the case of $CHBr_3$. Therefore, further iterations with shorter time intervals to optimize the lower boundary are investigated in the following.

6.3 Regionally resolved boundary with monthly dependence

Two new ideas proposed in this chapter are refining the geography of the source region on smaller scales and reducing the lower boundary time interval to a monthly dependency. Utilizing the seasonal dependent regionally resolved lower boundary, the newly refined global map has undergone improvements based on the distribution of data shown in Appendix D. It discloses the concentration of air parcels in specific areas along the coastline

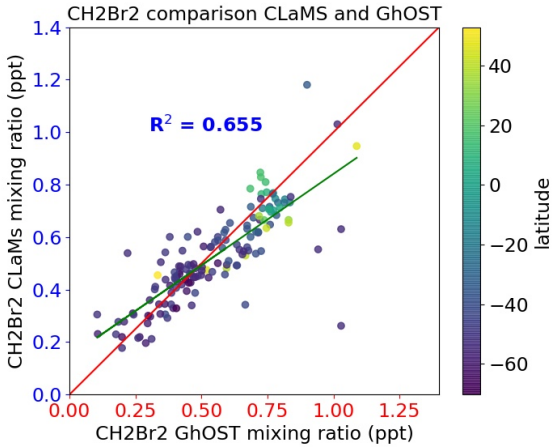

(a) CH_2Br_2 at different latitudes

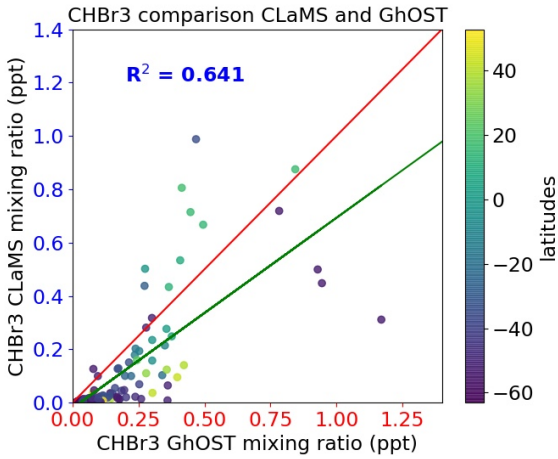

(b) $CHBr_3$ at different latitudes

Figure 6.15: Comparison of the relationships between the CLaMS model simulation with the seasonal dependent regionally resolved lower boundary and the GhOST measurements for $CHBr_3$ and CH_2Br_2 from September to mid-November in 2019. The colour code represents different latitudes from 48°N to 70°S. The red line is the 1:1 line and the green line is the best-fit line.

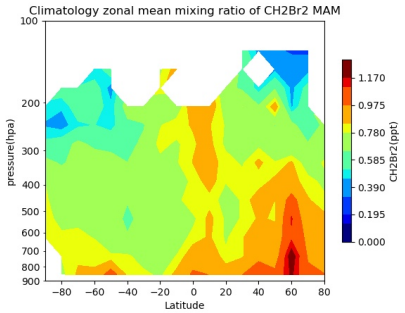

(a) observations in MAM

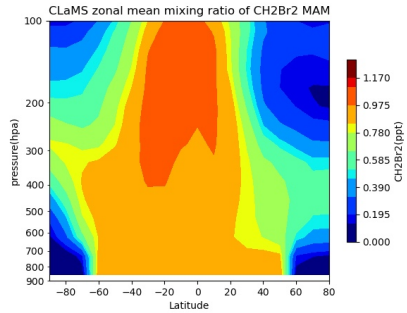

(b) simulations in MAM

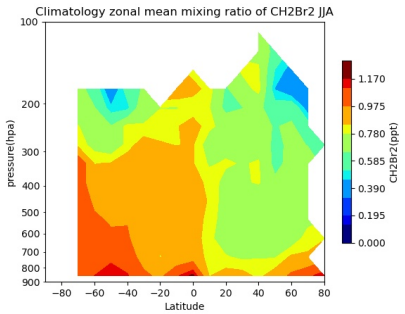

(c) observations in JJA

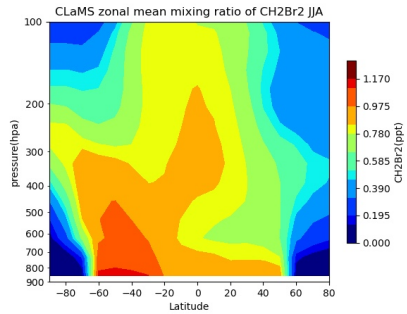

(d) simulations in JJA

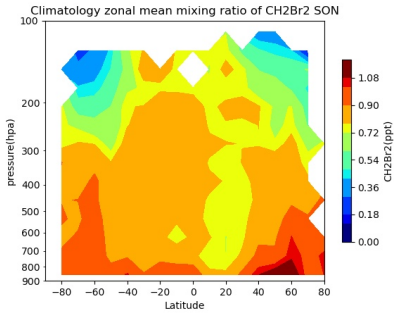

(e) observations in SON

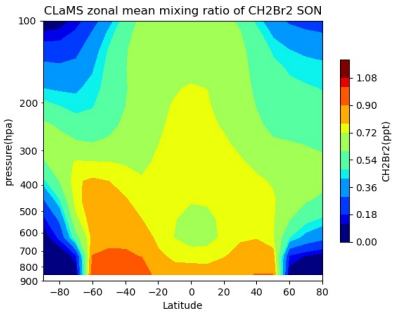

(f) simulations in SON

Figure 6.16: Altitude-latitude cross section of CH_2Br_2 simulation results with seasonal dependent regionally resolved lower boundary. The data are separated by three seasons (MAM (March, April, May); JJA (June, July, August); SON (September, October, November)) as a function of latitude and pressure. The left column (**a**, **c** and **e**) show observational climatology data. The right column (**b**, **d** and **f**) show model results in CLaMS 2.0 version with regionally resolved seasonal-dependent lower boundary. The scale of color bars in different season is different.

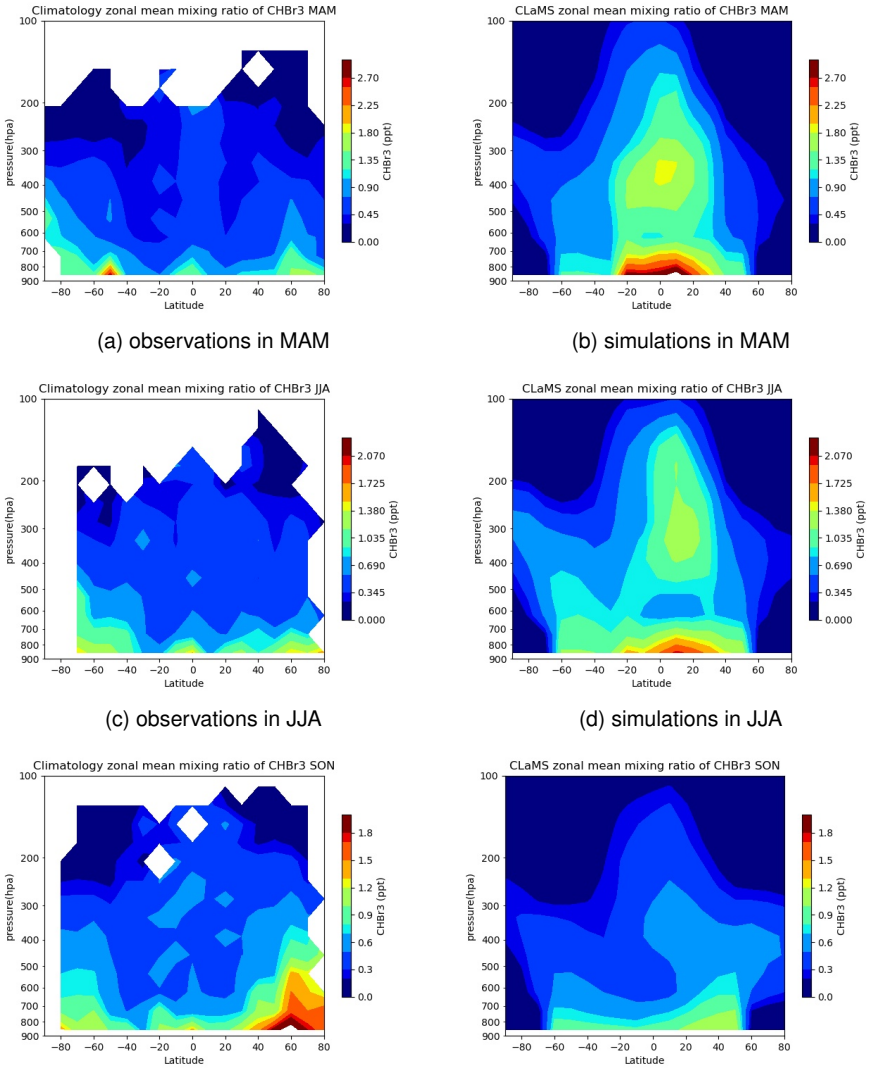

(a) observations in MAM

(b) simulations in MAM

(c) observations in JJA

(d) simulations in JJA

(e) observations in SON

(f) simulations in SON

Figure 6.17: Altitude-latitude cross section of $CHBr_3$ simulation results with seasonal dependent regionally resolved lower boundary. The data are separated by three seasons (MAM (March, April, May); JJA (June, July, August); SON (September, October, November)) as a function of latitude and pressure. The left column (**a**, **c** and **e**) show observational climatology data. The right column (**b**, **d** and **f**) show model results in CLaMS 2.0 version with regionally resolved seasonal-dependent lower boundary. The scale of color bars in different season is different.

and within the zoning of particular continental regions. To improve the simulation results, in contract to previous chapter, some of the regions were more regionally resolved. As shown in Figure 6.12, initially, the European area was subdivided into North (orange part) and South parts (cyan part). Subsequently, Central America (CAM) was further separated into three distinct segments. Additionally, alongside the previously mentioned coastline 1 at the southern end of Southern America (SAM) (shown as pink part), three new coastlines were introduced. Coastline 2 extended between the Near East region (Neast) and the Northern Indian Ocean (NIO) (shown as light blue region), coastline 3 extended between Northern Africa (NAF) and Neast (shown as yellow region), and coastline 4 stretched between Eastern China (ECH) and Southeast Asia (SEA) (shown as light green region). This new refinement should resulted in more accurate lower boundary distribution.

The new iteration of optimized lower boundary conditions for CH_2Br_2 and $CHBr_3$ was calculated based on the difference in mixing ratios between observations and previous simulations with the seasonal dependent regionally resolved lower boundary (as discussed in Section 6.2.2). Similar to previous simulation, air parcels were initially traced back to the ground, accounting for both long-range transport and deep convection within a 4-month period. Concurrently, these air parcels were categorized into individual months according to their traced back time. Subsequently, within each month, median values were calculated over different regions. However, with the shortened time interval, the number of available air parcels at the ground within each month decreased, leading to limited or no data points in certain areas, particularly during the months of January to April and December. Under these circumstances, the values of the preceding seasonal dependent regionally resolved lower boundary (as detailed in Section 6.2.2) were used. For instance, as depicted in the global distribution maps for $CHBr_3$ and CH_2Br_2 (Appendix E), the values from January to March were identical due to the absence of available traced-back data points. These values are calculated based on the previous seasonal dependent regionally resolved lower boundary. Similarly, in regions lacking data points, if the previous month has a newly optimized value, the mixing ratio for that specific region in the

current month is maintained at the same optimized value. Figure E.1 and E.2 (Appendix E) illustrate the constructed monthly dependent regionally resolved lower boundary distributions across different surface regions for CH_2Br_2 and $CHBr_3$. The colour bars in the figures represent different mixing ratios.

The constructed monthly dependent regionally resolved lower boundary distributions of CH_2Br_2 and $CHBr_3$ exhibit significant seasonal and latitudinal variations, revealing distinct emission patterns in specific geographical areas. For CH_2Br_2, the seasonal variation is similar to the climatological lower boundary data provided in Appendix C. During April to June, higher mixing ratios are observed in the Southern Hemisphere (SH) tropical region and the tropical to mid-latitudes in the Northern Hemisphere (NH) (ranging from 20°S to 60°N) compared to the mid-latitudes in the SH (20°S to 60°S). In July to September, conversely, the SH mid-latitudes have higher mixing ratios than those in the SH tropical region and NH tropical to mid-latitudes. From October to December, mid-latitudes in both hemispheres exhibit higher mixing ratios compared to those in tropical regions. Additionally, certain continental surface sources contribute significantly, such as the central part of Central America (CAM), which reaches a peak mixing ratio of 1.24 ppt during April to June. For $CHBr_3$, with its shorter lifetime and susceptibility to local sources, temporal and regional variations are more pronounced. Notably, the Asian region, including Southern Asia (SEA), the Bay of Bengal (BoB), the Indian Subcontinent (IND), and the combined region of Northern Indian Ocean, Tibetan Plateau, and Eastern China (NIN+TIB+ECH), maintains elevated mixing ratios from April to August, ranging from 5 ppt to 14 ppt. Oceanic sources in the tropical region, such as Tropical Eastern Pacific (TEP) and Northern Indian Ocean (NIO), consistently contribute high mixing ratios from April to July, peaking around 8.29 ppt and 9.21 ppt, respectively. Also, this construction reveals unrealistically high $CHBr_3$ mixing ratios in certain regions. Coastal regions, like coastlines 2, 3, and 4, also exhibit peak mixing ratios in June, reaching values of 11.29 ppt, 11.11 ppt, and 10.55 ppt, respectively. It is noteworthy that these mixing ratios are considerably higher than anticipated, indicating the necessity for additional iterations to mitigate calculation bias arising from insufficient observational data coverage across

all seasons.

Despite the mentioned deficiencies with this boundary, a simulation was conducted with CLaMS 2.0 with the same setup as the previous simulation except for the lower boundary. The model results were then compared with observations, as illustrated in Figure 6.18. The one-to-one comparison for CH_2Br_2 (shown in Figure 6.18a) reveals a striking similarity between the best-fit line (represented by the green line) and the 1:1 line (depicted in red), which indicates an even distribution of data points on both sides of the 1:1 line. In comparison to the coefficient of determination of 0.655 for the simulation with a seasonal dependent regionally resolved lower boundary and 0.8 for the simulation with a zonally symmetric seasonal lower boundary, the coefficient of determination in this simulation has increased to 0.812, indicating enhanced agreement. Furthermore, the calculated average relative difference is remarkably low, with a value of 5.3$\pm$32%, signifying a strong agreement between the model and observations. The good agreement between the SouthTRAC observations and simulation results emphasizes the effectiveness of the monthly dependent regionally resolved lower boundary conditions in accurately representing the surface distribution.

As for $CHBr_3$, the best-fit line is also close to the 1:1 line, with the majority of data points falling within this region. It is noteworthy that the coefficient of determination for the simulation with a monthly dependent regionally resolved lower boundary is 0.802, surpassing the values of 0.788 and 0.641 in the previous simulations with zonally symmetric lower boundary and seasonal dependent regionally resolved lower boundary, respectively (as depicted in Figure 6.2b and Figure 6.15b). In terms of the relative difference comparison, the simulation with a monthly dependent regionally resolved lower boundary shows a lower mean deviation of -37.3$\pm$54% compared to the previous simulation with a zonally symmetric lower boundary (-68.3$\pm$39%) and a regionally resolved lower boundary with seasonally dependence (-56.5$\pm$44%), respectively. These findings suggest an enhancement in the new simulated results with a regionally resolved lower boundary with monthly dependence. However, noteworthy outliers are observed, particularly in the Southern Hemisphere (SH) latitude bands (30°S to 80°S), where the relative difference reaches up

to -50.6±43%. This suggests a tendency for the simulation results to be lower than the observations. This potential underestimation in the lower boundary could be attributed to the scarcity of available observational data in spring and summer. The limited number of observations traceable to the surface during these specific months makes it challenging to derive statistically robust averages.

Figure 6.19 and 6.20 show the latitude-pressure cross section of CH_2Br_2 and $CHBr_3$ for the zonal mean mixing ratio of CLaMS simulation (**a**, **c** and **e**) and observations from climatology data (**b**, **d** and **f**). With the exception of the southern high latitudes (exceeding 70°S) during JJA and SON, the observational data offers a comprehensive description of the tropospheric and lower stratospheric distribution. In the case of CH_2Br_2, the model's distribution in the lower troposphere represents a better improvement compared to the simulation with regionally resolved lower boundary with seasonal dependence (depicted in Figure 6.16). However, at higher altitudes near the tropopause, the noticeable biases in comparison to observations remain pronounced in tropical regions across different seasons. For instance, during MAM, the mixing ratios near the tropopause region are significantly higher than those in the climatology data, and in SON, the mixing ratios are lower than the observations by up to 0.2 ppt.

Regarding $CHBr_3$, mixing ratios in tropical regions at lower troposphere are significantly overestimated by the model than the climatology data, reaching up to 3.3 ppt and 5.7 ppt in JJA and MAM, which are even higher than the model simulation with a seasonal dependent regionally resolved lower boundary (depicted in Figure 6.17b and Figure 6.17d). However, during SON, in high latitudes of the Northern Hemisphere (over 60°N), the model results in the lower troposphere exhibit slightly smaller values than the climatology, representing an improvement compared to the previous simulation with seasonal dependent regionally resolved lower boundary. The overestimated mixing ratios in the lower troposphere within tropical regions, as discussed earlier, are attributed to specific geographic regions with high values, necessitating further optimization. Furthermore, the model results overestimate the mixing ratio in the tropical upper troposphere and lower stratosphere (UTLS) region, resulting in a larger bias than the simulation results with

seasonal dependent regionally resolved lower boundary.

The comparison in Figure 6.18 between the model simulation and SouthTRAC observations indicates a significant improvement in the simulation results for both CH_2Br_2 and $CHBr_3$ with the new monthly dependent regionally resolved lower boundary. This agrees with the comparison between the model simulation and climatology data in SON, indicating better agreement compared to the results in other seasons (MAM and JJA), as well as the previous simulation results with seasonal dependent regionally resolved lower boundary. However, the mixing ratios of $CHBr_3$ and CH_2Br_2 in the model results for the higher troposphere and the UTLS region are inconsistent with the climatology data. Since the model simulation starts in May, the higher mixing ratio compared to the climatology in MAM may be attributed to the higher initialization values derived from the tracer correlation method. There is a noticeable decrease in composition for both $CHBr_3$ and CH_2Br_2 in the tropical UTLS region over time. Specifically, in the SON, the mixing ratio for CH_2Br_2 in the tropical UTLS region is decreased below the climatology value. For $CHBr_3$, the mixing ratio in tropical UTLS is slightly higher than in climatology. These inconsistencies with climatology could arise from various factors. On the one side, there might be an overestimation of the tropical mixing ratio at the lower boundary. On the other side, chemical effects or discrepancies in upward transport could also contribute to these discrepancies. To further explore the discrepancies in the tropical UTLS, a comparison between climatology data and simulation with a zonally symmetric seasonal lower boundary is presented in the Appendix F. With the same lower boundary as climatology, the simulated mixing ratio in the SON is lower than the climatology for both $CHBr_3$ and CH_2Br_2. This discrepancy could be attributed to either inaccurate chemical reaction rates in the simulation or an underestimation of upward transport. Furthermore, this finding suggests an overestimation of the lower boundary for $CHBr_3$.

The lower mixing ratio in high latitudes of the NH compared to the climatology is likely attributed to the 'top-down' lower boundary estimates in this thesis, derived from SouthTRAC aircraft campaigns that primarily utilized observational data from the SH. The lack of sufficient data points from the NH presents challenges in accurately capturing the dis-

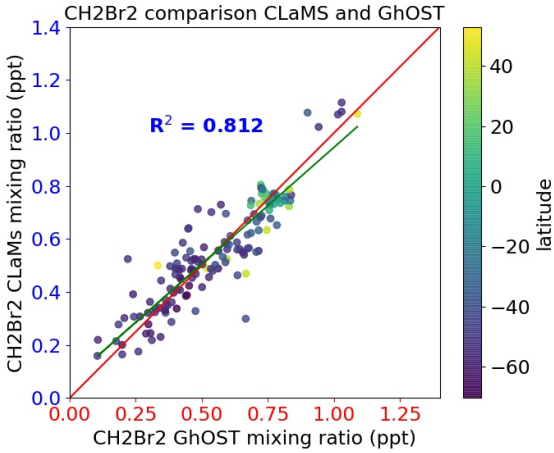

(a) CH_2Br_2 at different latitudes

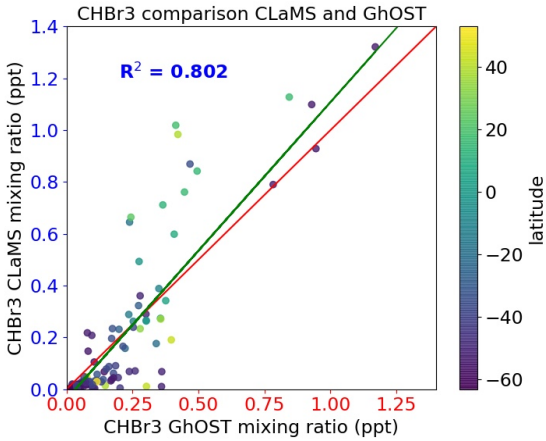

(b) $CHBr_3$ at different latitudes

Figure 6.18: Comparison between CLaMS model simulation with regionally resolved monthly-dependent lower boundary and observations from SouthTRAC campaign (from September to mid-November in 2019) at different latitudes between 48°N and 70°S. The x-coordinate is the mixing ratios of GhOST observations, and Y-axis is the mixing ratios of CLaMS simulations. The red line represents the 1:1 line, and the green line represents the best-fit line.

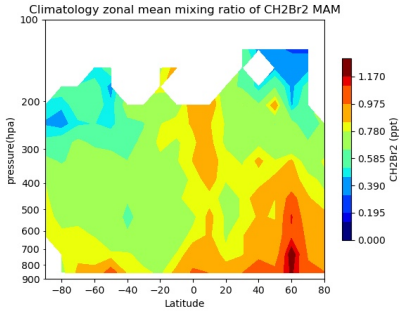

(a) observations in MAM

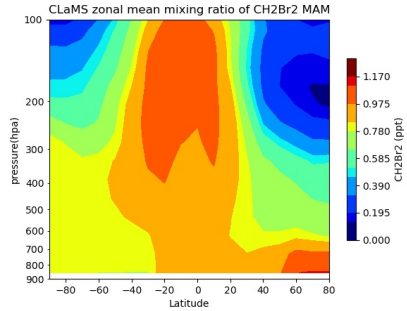

(b) simulations in MAM

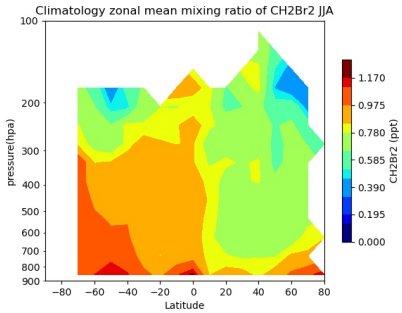

(c) observations in JJA

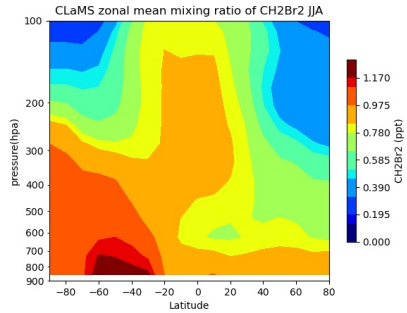

(d) simulations in JJA

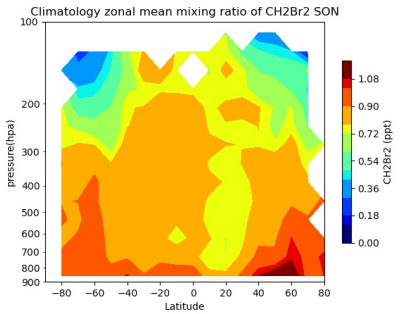

(e) observations in SON

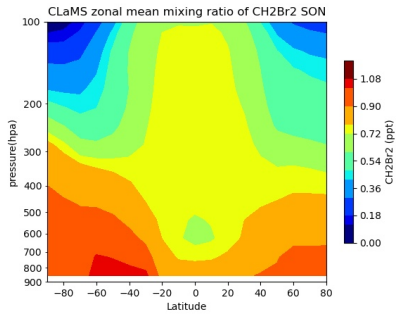

(f) simulations in SON

Figure 6.19: Altitude-latitude cross section of CH_2Br_2. The data are separated by three seasons (MAM (March, April, May); JJA (June, July, August); SON (September, October, November)) as a function of latitude and pressure. The left column (**a**, **c** and **e**) shows observational climatology data. The right column (**b**, **d** and **f**) shows the model results in CLaMS 2.0 version with a regionally resolved monthly-dependent lower boundary. The scale of color bars is different in different season.

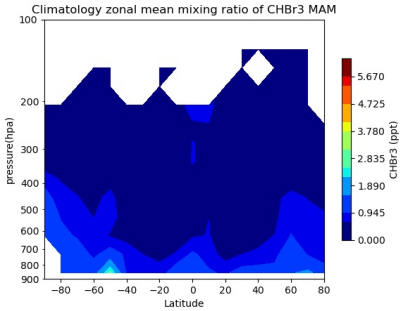

(a) observations in MAM

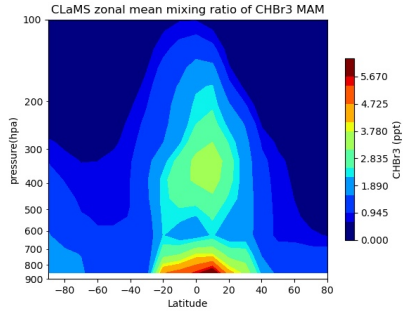

(b) simulations in MAM

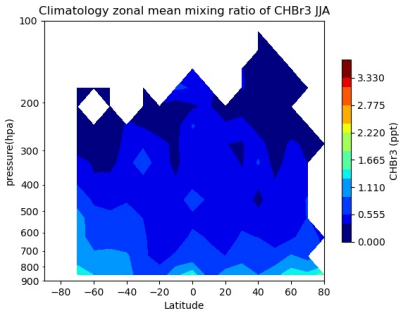

(c) observations in JJA

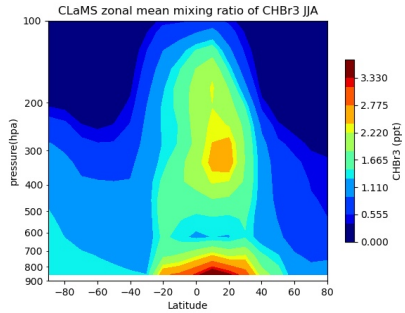

(d) simulations in JJA

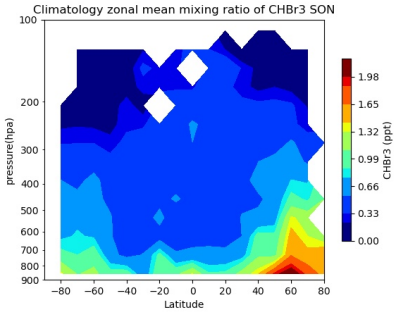

(e) observations data in SON

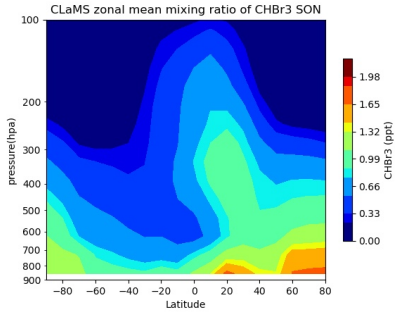

(f) simulations in SON

Figure 6.20: Altitude-latitude cross section of $CHBr_3$. The data are separated by three seasons (MAM (March, April, May); JJA (June, July, August); SON (September, October, November)) as a function of latitude and pressure. The left column (**a**, **c** and **e**) show observational climatology data. The right column (**b**, **d** and **f**) show model results in CLaMS 2.0 version with a regionally resolved monthly-dependent lower boundary. The scale of color bars is different in different season.

tribution in the NH, especially in high latitudes, where there may be possible brominated sources from sea ice. Regarding the overestimated lower boundary for $CHBr_3$, as mentioned earlier, it has a much shorter atmospheric lifetime than CH_2Br_2, leading to a more pronounced influence of specific local emissions on atmospheric distribution variability. The four-month period for back trajectory calculation, longer than the lifetime of $CHBr_3$, significantly affects the accuracy of capturing the distribution at the lower boundary level, resulting in significant overestimation and strong variability in certain regions.

In summary, even though there are some improvements in the comparison with the SouthTRAC data, this constructed boundary still contains deficiencies like the overestimation of mixing ratios in certain regions and discontinuities in time and location. From that, it can be concluded that this data set alone does not have enough statistics to derive such a detailed lower boundary. To construct a more accurate global lower boundary and ensure the distribution of brominated very short-lived substances (VSLS) doesn't have unrealistic values, it is essential to align the traced back time with the lifetime of specific species. In this case, observation data across all seasons must be incorporated for comprehensiveness. To minimize errors in calculating the better-optimized lower boundary, several additional iterations are required.

Chapter 7

Summary and outlook

The brominated very short-lived species (VSLS), with lifetimes shorter than six months, play a crucial role as a significant source of atmospheric bromine, a factor that can contribute to the depletion of stratospheric ozone. Consequently, understanding the global source distribution of these species is of paramount importance. This thesis is dedicated to the estimation of mixing ratio distribution at the global surface lower boundary, with a particular focus on two main contributors to total bromine: $CHBr_3$ and CH_2Br_2.

The chemistry scheme developed in this thesis yields a good understanding of the photochemical reaction mechanism occurring in the atmosphere. In addition to the photolysis reactions involving relevant brominated species ($CHBr_3$, CH_2Br_2, CH_3Br, CH_2BrCl, $CHBr_2Cl$, $CHBrCl_2$, H1211, H1301, H2402), reactions with hydroxyl radical (OH), chlorine radical (Cl) and oxygen radical ($O(^1D)$), have been incorporated (Section 4.1). Based on the understanding derived from this chemical scheme, the vertical distribution of mixing ratios and the locally averaged lifetime for individual species were determined by calculating scenarios involving a single air parcel as well as multiple vertically ascending air parcels within CLaMS (Chemical Lagrangian Model of the Stratosphere). The extension to the brominated species was validated by contrasting the localized lifetime of these brominated species with the global mean lifetime (as defined by the World Meteorological Organization (WMO)) (Section 4.2). Several settings of the 3-dimensional chemistry transport model MESSy-CLaMS utilizing this chemistry scheme have been tested for a

period of 6 months (from May to November 2019). This period was chosen because of the available GhOST measurements from the SouthTRAC aircraft campaign.

The first simulation was initialized using the correlation between the individual bromine-containing species and N_2O (Rotermund et al., 2021). The lower boundary for the brominated VSLS is latitude-dependent, with the highest values in the tropics and uniform poleward of 45° North and South, whereas the boundary condition for halons and CH_3Br is uniform (Section 5.2). It was observed that a disrupted relationship emerged between the inorganic bromine species and N_2O in the simulation results. This divergence was attributed to the absence of scavenging processes in water and ice clouds for soluble inorganic bromine within the troposphere (see Section 5.1). The incorporation of a parameterization for the scavenging sink of HOBr and HBr yielded better results, but discrepancies did remain. These were potentially attributed to slower vertical transport. Hence, the simulation results incorporating additional tropospheric mixing and convective updrafts within the updated model version MESSy-CLaMS 2.0 (Konopka et al., 2019) have brought the averaged mixing ratios of brominated VSLS between 40° and 60°N closer to observations during the period from August to October 2017 (Keber et al., 2020). Upon comparing these results with aircraft measurements from the SouthTRAC campaign, the remaining discrepancies were most likely due to the use of a simplified lower boundary pattern in this simulation.

In the course of this thesis work, a comprehensive climatology was made available by Jesswein et al. (2022) in which observations of multiple aircraft campaigns were consistently combined. From that climatology data, the zonally symmetric seasonal lower boundary was incorporated into the CLaMS model simulation, and the results were discussed in detail within this work. Comparing CLaMS simulations with observational data from the SouthTRAC campaign, the agreement is notably improved when using a zonally symmetric seasonal lower boundary, but certain disparities still remain.

The next idea to overcome the discrepancies was to use surface origin tracers to figure out the source regions behind the remaining differences. These tracers were employed to derive a regionally resolved boundary condition. To focus on the observations

that are influenced by recent boundary contact, the used observations were restricted to those with a mean age of air less than six months. However, for the given 32 source regions and the statistics of the SouthTRAC data, this approach did not yield conclusive results. For instance, some source regions exhibited both positive and negative offsets compared to the observations (Section 6.1).

Given these circumstances, the global seasonal lower boundary—obtained through back trajectories to determine mixing ratios for air parcels in various geographic source regions—was implemented to improve the derived lower boundary. To address missing regional values, seasonal zonally symmetric climatology data from Jesswein et al. (2022) was used to fill the gaps. This regionally resolved lower boundary with seasonal dependence is primarily focused on the two most significant brominated VSLSs: $CHBr_3$ and CH_2Br_2. Since the convective updraft of air masses is tested in the calculation of the backward trajectories, the Convective Available Potential Energy (CAPE) was used to assess the occurrence of deep convection. The results show that air parcels from two primary deep convective source regions, southern Asia and the Northern African continent, yield a significant fraction of the bromine chemical composition of UTLS region over the Southern Pacific and Southern Atlantic Oceans. Nevertheless, the expected enhancement in simulation results with a seasonal dependent regionally resolved lower boundary did not succeed as anticipated. In particular, the so-derived boundary contained unrealistically high mixing ratios of $CHBr_3$ in some source regions (Section 6.2).

To further minimize the discrepancies in atmospheric mixing ratios between simulations and observations, the smaller-scale source regions were refined, and the time interval for lower boundary conditions was shortened. Distinct mixing ratios for the lower boundary were computed for each month, with the exception of January, February, and March. Data gaps were filled using the results from the previous simulation, which employed a seasonal dependent regionally resolved lower boundary (in Section 6.2). For both the $CHBr_3$ and CH_2Br_2, the distribution of simulated atmospheric mixing ratios shows improvement compared to observational measurements during the SouthTRAC campaign in both hemispheres. Nonetheless, there remain a few outliers, particularly

notably for $CHBr_3$, which exhibit higher mixing ratios than observed measurements in the SH. In addition, when conducting a detailed comparison between observed climatology data and model simulations across three seasons, inconsistencies emerge in the mixing ratio distribution within the tropical Upper Troposphere and Lower Stratosphere (UTLS) region. Through further parallel comparison of simulations using zonally symmetric seasonal lower boundary, this discordance may stem from inaccurate chemical reaction rates or underestimations of upward transport. Furthermore, the lower boundary for $CHBr_3$ is potentially overestimated. As the derivation of the monthly lower boundary yielded unrealistically high mixing ratios of $CHBr_3$, it can be concluded that there is a need for additional observations to construct a more comprehensive lower boundary (Section 6.3).

The results of this thesis put forward several interesting topics to be explored in the future. Firstly, investigate the accurate interpretation of upward transport by adjusting the parameter settings of the MESSy-CLaMS 2.0 model. Secondly, combine different measurement data from diverse campaigns and reconcile observations for the brominated VSLSs to optimize the lower boundary. Thirdly, if a lower boundary given as mixing ratios for the bromine-containing species would not be successful, the boundary in CLaMS could be concluded from estimations of emission fluxes. However, this would require some further model development. For example, improvements to mass conservation in the Lagrangian model CLaMS would be necessary. Lastly, incorporate the previously ignored potential source from sea ice into the estimated lower boundary, based on observational data (Abrahamsson et al., 2018).

List of Figures

2.1 Atmospheric layers 8

2.2 Tropical tropopause layer transport mechanism 12

2.3 Schematic of long-lived ozone-depleting substances (ODSs) and halogenated very short-lived substances (VSLSs) 17

2.4 Bromine input to stratosphere 21

2.5 Stratospheric total bromine loading 22

3.1 Unresolved convection and vertical mixing 29

3.2 Flight tracks of the SouthTRAC campaign 31

4.1 Absorption cross section for H2402, $CHBr_3$ and CH_2BrCl 34

4.2 New chemistry scheme 35

4.3 Profiles for mixing ratios, reaction rates and lifetimes of $CHBr_3$, CH_2Br_2 and H301 37

4.4 Latitude-dependent lifetime under 100 hPa and 300 hPa 38

4.5 Comparison of box model simulation results between classical CLaMS and MESSy-CLaMS 41

4.6 Altitude-latitude cross section of $CHBr_3$ and CH_2Br_2 for MESSy-CLaMS model simulation on October 6th in 2019. 42

5.1 The fixed lower boundary conditions 44

5.2 Observational correlations between N_2O and brominated species 46

5.3 Simulation correlations between N_2O and brominated species 47

5.4 Compare the results of the simulation with the Br_y^{inorg} removal reactions and the previous simulation without these reactions. 49
5.5 Comparison of simulations in CLaMS 1.0 and 2.0 for VSLS and CH_3Br . . 50
5.6 Comparison of mean values for simulated brominated VSLS with observations 52
5.7 Inferred total bromine as a function of potential temperature difference to the tropopause (TP) 54
5.8 One-by-one comparison of relationships between CLaMS 2.0 simulation and GhOST measurement data 55
5.8 (Cont.) 56
5.9 Mixing ratio of simulation results of CLaMS 2.0 as a function of different latitudes in different vertical range 58
5.9 (Cont.) 59

6.1 Latitudinal seasonal lower boundary for brominated VSLS and CH_3Br . . . 63
6.2 One-by-one comparison of relationships between model simulation with new seasonal latitudinal averaged lower boundary and the GhOST measurement data 65
6.2 (Cont.) 66
6.3 Mixing ratio one-by-one comparison between CLaMS simulation and GhOST observation at different latitudes 67
6.3 (Cont.) 68
6.4 World map depicting the lower boundaries and list of tracer names 70
6.5 The accumulated percentage of the most abundant contributed surface origin tracers for the first transfer flight at tropopause region 71
6.6 Comparison of the mixing ratios between simulation and observations at different latitudes in first transfer flight 74
6.7 AOA comparison between simulation results and observations 76
6.8 Air masses from different emission sources with mixing ratio difference between model and observations for $CHBr_3$ and CH_2Br_2 79

6.9 Air masses from different emission sources with both negative and positive mixing ratio difference between model and observations for $CHBr_3$ and CH_2Br_2 80
6.10 CAPE and θ_{max} global maps 83
6.11 Global distribution of difference percentage in mixing ratios for CH_2Br_2 (**a**) and $CHBr_3$ (**b**) at lower boundary 85
6.12 Second version of world map depicting the lower boundaries region 88
6.13 Distributions of regionally resolved lower boundary conditions with seasonal dependence for CH_2Br_2 89
6.13 (Cont.) 90
6.14 Seasonal global distributions of lower boundary conditions for $CHBr_3$ . . . 91
6.14 (Cont.) 92
6.15 Comparison between CLaMS model and observations derived from SouthTRAC campaign at different latitudes 96
6.16 Altitude-latitude cross section of CH_2Br_2 with seasonal dependent regionally resolved lower boundary 97
6.17 Altitude-latitude cross section of $CHBr_3$ with seasonal dependent regionally resolved lower boundary 98
6.18 Comparison between CLaMS model simulation with monthly dependent regionally resolved lower boundary and observations from SouthTRAC campaign at different latitudes 104
6.19 Altitude-latitude cross section of CH_2Br_2 105
6.20 Altitude-latitude cross section of $CHBr_3$ 106

A.1 Mixing ratios of inorganic bromine (Br_y^{inorg}) at different time 134

B.1 The accumulation of the abundant contributed percentages in CLaMS 1.0 model simulation 135
B.2 Global geographical regions of lower boundary emission sources in CLaMS 1.0 model simulation. 136

C.1 CH_2Br_2 lower boundary maps of different seasons 137
C.1 (Cont.) 138
C.2 $CHBr_3$ lower boundary maps of different seasons 139
C.2 (Cont.) 140

D.1 The traced back air parcels for CH_2Br_2 at lower boundary in different months 141
D.1 (Cont.) 142
D.1 (Cont.) 143
D.2 The traced back air parcels for $CHBr_3$ at lower boundary in different months 144
D.2 (Cont.) 145
D.2 (Cont.) 146

E.1 Global maps of monthly dependent regional resolved lower boundary mixing ratios (ppt) for dibromomethane (CH_2Br_2). 148
E.1 (Cont.) 149
E.1 (Cont.) 150
E.1 (Cont.) 151
E.2 Global maps of monthly dependent regional resolved lower boundary mixing ratios (ppt) for bromoform ($CHBr_3$). 152
E.2 (Cont.) 153
E.2 (Cont.) 154
E.2 (Cont.) 155

F.1 Altitude-latitude cross section of CH_2Br_2 157
F.2 Altitude-latitude cross section of $CHBr_3$ 158

List of Tables

4.1 Comparison of local lifetime and global mean lifetime 39

5.1 Averaged simulation results at tropopause (TP) and 40 K above tropopause (TP + 40 K) with observations 53

List of abbreviations

CLaMS Chemical Lagrangian Model of the Stratosphere

UV ultraviolet

ODS ozone-depleting substances

SGs source gases

PGs product gases

VSLS Very shot-lived species

VSLSs Very shot-lived substances

3D three-dimensional

TTL Tropical Tropopause layer

BDC Brewer-Dobson circulation

CLWC cloud liquid water content

CIWC cloud ice water content

UTLS upper troposphere–lowermost stratosphere

ppt parts per trillion

ppmv parts per million by volume

CCM chemistry-climate model

Bry Inorganic bromine

WMO World Meteorological Organization

MESSy Modular Earth Submodel System

Southern Hemisphere Transport, Dynamics, and Chemistry SouthTRAC

APs air parcels

ECMWF European Centre for Medium-Range Weather Forecasts

TRAJ Trajectory module

MIX Mixing module

CHEM Chemistry module

MLS Microwave Limb Sounder

GhOST Gas Chromatograph for Observational Studies using Tracers

HALO High Altitude and Long Range Research Aircraft

GC gas chromatograph

HIPPO HIAPER Pole-to-Pole Observations

ATom Atmospheric Tomography

MS mass spectrometer

WISE Wave-Driven Entropy Exchange

TND total number density

TP tropopause

TACTS Transport and Composition in the Upper Troposphere/Lowermost Stratosphere

Bibliography

K. Abrahamsson, A. Granfors, M. Ahnoff, C. A. Cuevas, and A. Saiz-Lopez. Organic bromine compounds produced in sea ice in Antarctic winter. *Nature Communications*, 9(1):5291, Dec. 2018. doi: 10.1038/s41467-018-07062-8.

J. Aschmann. Modeling the transport of very short-lived substances into the tropical upper troposphere and lower stratosphere. *Atmospheric Chemistry and Physics*, 2009.

J. Aschmann and B.-M. Sinnhuber. Contribution of very short-lived substances to stratospheric bromine loading: Uncertainties and constraints. *Atmospheric Chemistry and Physics*, 13(3):1203–1219, 2013. ISSN 1680-7324. doi: 10.5194/acp-13-1203-2013.

J. Aschmann, B.-M. Sinnhuber, M. P. Chipperfield, and R. Hossaini. Impact of deep convection and dehydration on bromine loading in the upper troposphere and lower stratosphere. *Atmospheric Chemistry and Physics*, 11(6):2671–2687, Mar. 2011. doi: 10.5194/acp-11-2671-2011.

M. J. Ashfold, N. R. P. Harris, A. J. Manning, A. D. Robinson, N. J. Warwick, and J. A. Pyle. Estimates of tropical bromoform emissions using an inversion method. *Atmospheric Chemistry and Physics*, 14(2):979–994, 2014. ISSN 1680-7324. doi: 10.5194/acp-14-979-2014.

P. W. Barnes, C. E. Williamson, R. M. Lucas, S. A. Robinson, S. Madronich, N. D. Paul, J. F. Bornman, A. F. Bais, B. Sulzberger, S. R. Wilson, A. L. Andrady, R. L. McKenzie, P. J. Neale, A. T. Austin, G. H. Bernhard, K. R. Solomon, R. E. Neale, P. J. Young, M. Norval, L. E. Rhodes, S. Hylander, K. C. Rose, J. Longstreth, P. J. Aucamp, C. L.

Ballaré, R. M. Cory, S. D. Flint, F. R. de Gruijl, D.-P. Häder, A. M. Heikkilä, M. A. K. Jansen, K. K. Pandey, T. M. Robson, C. A. Sinclair, S.-Å. Wängberg, R. C. Worrest, S. Yazar, A. R. Young, and R. G. Zepp. Ozone depletion, ultraviolet radiation, climate change and prospects for a sustainable future. *Nature Sustainability*, 2(7):569–579, 2019. ISSN 2398-9629. doi: 10.1038/s41893-019-0314-2.

P. W. Barnes, T. M. Robson, P. J. Neale, C. E. Williamson, R. G. Zepp, S. Madronich, S. R. Wilson, A. L. Andrady, A. M. Heikkilä, G. H. Bernhard, A. F. Bais, R. E. Neale, J. F. Bornman, M. A. K. Jansen, A. R. Klekociuk, J. Martinez-Abaigar, S. A. Robinson, Q.-W. Wang, A. T. Banaszak, D.-P. Häder, S. Hylander, K. C. Rose, S.-Å. Wängberg, B. Foereid, W.-C. Hou, R. Ossola, N. D. Paul, J. E. Ukpebor, M. P. S. Andersen, J. Longstreth, T. Schikowski, K. R. Solomon, B. Sulzberger, L. S. Bruckman, K. K. Pandey, C. C. White, L. Zhu, M. Zhu, P. J. Aucamp, J. B. Liley, R. L. McKenzie, M. Berwick, S. N. Byrne, L. M. Hollestein, R. M. Lucas, C. M. Olsen, L. E. Rhodes, S. Yazar, and A. R. Young. Environmental effects of stratospheric ozone depletion, UV radiation, and interactions with climate change: UNEP Environmental Effects Assessment Panel, Update 2021. *Photochemical & Photobiological Sciences*, 21(3):275–301, 2022. ISSN 1474-9092. doi: 10.1007/s43630-022-00176-5.

J. A. Barrera, R. P. Fernandez, F. Iglesias-Suarez, C. A. Cuevas, J.-F. Lamarque, and A. Saiz-Lopez. Seasonal impact of biogenic very short-lived bromocarbons on lowermost stratospheric ozone between 60° N and 60° S during the 21st century. *Atmospheric Chemistry and Physics*, 20(13):8083–8102, July 2020. doi: 10.5194/acp-20-8083-2020.

S. Brinckmann, A. Engel, H. Bönisch, B. Quack, and E. Atlas. Short-lived brominated hydrocarbons – observations in the source regions and the tropical tropopause layer. *Atmospheric Chemistry and Physics*, 12(3):1213–1228, Feb. 2012. ISSN 1680-7324. doi: 10.5194/acp-12-1213-2012.

J. Brioude, R. W. Portmann, J. S. Daniel, O. R. Cooper, G. J. Frost, K. H. Rosenlof, C. Granier, A. R. Ravishankara, S. A. Montzka, and A. Stohl. Variations in ozone

depletion potentials of very short-lived substances with season and emission region. *Geophysical Research Letters*, 37(19), 2010. ISSN 1944-8007. doi: 10.1029/2010GL044856.

J. B. Burkholder, S. P. Sander, and J. P. D. Abbatt. *JPL Publication 19-5. Chemical Kinetics and Photochemical Data for Use in Atmospheric Studies*. National Aeronautics and Space Administration, 2015.

J. H. Butler, D. B. King, J. M. Lobert, S. A. Montzka, S. A. Yvon-Lewis, B. D. Hall, N. J. Warwick, D. J. Mondeel, M. Aydin, and J. W. Elkins. Oceanic distributions and emissions of short-lived halocarbons. *Global Biogeochemical Cycles*, 21(1), 2007. ISSN 1944-9224. doi: 10.1029/2006GB002732.

L. J. Carpenter and P. S. Liss. On temperate sources of bromoform and other reactive organic bromine gases. *Journal of Geophysical Research: Atmospheres*, 105(D16): 20539–20547, 2000. ISSN 01480227. doi: 10.1029/2000JD900242.

R. Carpenter. *WMO: Scientific Assessment of Ozone Depletion: 2014, Global Ozone Research and Monitoring Project, Report No. 55, Chapt. 1, World Meteorological Organization, Geneva, Switzerland*. World Meteorological Organization, 2014.

G. D. Carver, P. D. Brown, and O. Wild. The ASAD atmospheric chemistry integration package and chemical reaction database. *Computer Physics Communications*, 105 (2):197–215, Oct. 1997. doi: 10.1016/S0010-4655(97)00056-8.

M. P. Chipperfield, S. Bekki, S. Dhomse, N. R. P. Harris, B. Hassler, R. Hossaini, W. Steinbrecht, R. Thiéblemont, and M. Weber. Detecting recovery of the stratospheric ozone layer. *Nature*, 549(7671):211–218, Sept. 2017. doi: 10.1038/nature23681.

A. Dépée, P. Lemaitre, T. Gelain, A. Mathieu, M. Monier, and A. Flossmann. Theoretical study of aerosol particle electroscavenging by clouds. *Journal of Aerosol Science*, 135: 1–20, Sept. 2019. doi: 10.1016/j.jaerosci.2019.04.001.

M. Dorf, J. H. Butler, A. Butz, C. Camy-Peyret, M. P. Chipperfield, L. Kritten, S. A. Montzka, B. Simmes, F. Weidner, and K. Pfeilsticker. Long-term observations of stratospheric

bromine reveal slow down in growth. *Geophysical Research Letters*, 33(24), 2006. doi: 10.1029/2006GL027714.

D. C. Dowdell, G. P. Matthews, and I. Wells. An investigation into the sensitivity of the atmospheric chlorine and bromine loading using a globally averaged mass balance model. *Atmospheric Environment*, 28(12):1989–1999, July 1994. ISSN 1352-2310. doi: 10.1016/1352-2310(94)90468-5.

A. Engel, M. Rigby, and S. A. Montzka. *WMO: Scientific Assessment of Ozone Depletion: 2018*. World Meteorological Organization, Geneva, Switzerland, 2018. ISBN 978-1-73293-171-8.

A. Engel, M. Rigby, J. B. Burkholder, R. P. Fernandez, L. Froidevaux, B. D. Hall, R. Hossaini, T. Saito, M. K. Vollmer, and B. Yao. *Update on Ozone-Depleting Substances (ODSs) and Other Gases of Interest to the Montreal Protocol*. World Meteorological Organization, 2019. ISBN 978-1-73293-171-8.

S. Falk, B.-M. Sinnhuber, G. Krysztofiak, P. Jöckel, P. Graf, and S. T. Lennartz. Brominated VSLS and their influence on ozone under a changing climate. *Atmospheric Chemistry and Physics*, 17(18):11313–11329, Sept. 2017. doi: 10.5194/acp-17-11313-2017.

J. C. Farman, B. G. Gardiner, and J. D. Shanklin. Large losses of total ozone in Antarctica reveal seasonal ClOx/NOx interaction. *Nature*, 315(6016):207–210, May 1985. doi: 10.1038/315207a0.

M. T. Filus, E. L. Atlas, M. A. Navarro, E. Meneguz, D. Thomson, M. J. Ashfold, L. J. Carpenter, S. J. Andrews, and N. R. P. Harris. Transport of short-lived halocarbons to the stratosphere over the Pacific Ocean. *Atmospheric Chemistry and Physics*, 20(2): 1163–1181, Jan. 2020. doi: 10.5194/acp-20-1163-2020.

W. Frey, R. Schofield, P. Hoor, D. Kunkel, F. Ravegnani, A. Ulanovsky, S. Viciani, F. D'Amato, and T. P. Lane. The impact of overshooting deep convection on local transport and mixing in the tropical upper troposphere/lower stratosphere (UTLS).

Atmospheric Chemistry and Physics, 15(11):6467–6486, June 2015. doi: 10.5194/acp-15-6467-2015.

F. Fritsch, H. Garny, A. Engel, H. Bönisch, and R. Eichinger. Sensitivity of age of air trends to the derivation method for non-linear increasing inert SF_6. *Atmospheric Chemistry and Physics*, 20(14):8709–8725, July 2020. doi: 10.5194/acp-20-8709-2020.

S. Fueglistaler, A. E. Dessler, T. J. Dunkerton, I. Folkins, Q. Fu, and P. W. Mote. Tropical tropopause layer. *Reviews of Geophysics*, 47(1), 2009. doi: 10.1029/2008RG000267.

A. Gettelman and T. Birner. Insights into Tropical Tropopause Layer processes using global models. *Journal of Geophysical Research: Atmospheres*, 112(D23), 2007. doi: 10.1029/2007JD008945.

A. Gettelman, P. M. d. F. Forster, M. Fujiwara, Q. Fu, H. Vömel, L. K. Gohar, C. Johanson, and M. Ammerman. Radiation balance of the tropical tropopause layer. *Journal of Geophysical Research: Atmospheres*, 109(D7), 2004. doi: 10.1029/2003JD004190.

A. Gettelman, P. H. Lauritzen, M. Park, and J. E. Kay. Processes regulating short-lived species in the tropical tropopause layer. *Journal of Geophysical Research: Atmospheres*, 114(D13), 2009. ISSN 2156-2202. doi: 10.1029/2009JD011785.

N. P. Gillett and D. W. J. Thompson. Simulation of Recent Southern Hemisphere Climate Change. *Science*, 302(5643):273–275, Oct. 2003. doi: 10.1126/science.1087440.

J.-U. Grooß and J. M. I. Russell. Technical note: A stratospheric climatology for O_3, H_2O, CH_4, NO_x, HCl and HF derived from HALOE measurements. *Atmospheric Chemistry and Physics*, 5(10):2797–2807, Oct. 2005. doi: 10.5194/acp-5-2797-2005.

J.-U. Grooß. *Modelling of stratospheric chemistry based on HALOE/UARS satellite data*. Shaker, 1996.

P. Haynes and E. Shuckburgh. Effective diffusivity as a diagnostic of atmospheric transport: 2. Troposphere and lower stratosphere. *Journal of Geophysical Research: Atmospheres*, 105(D18):22795–22810, 2000. doi: 10.1029/2000JD900092.

M. I. Hegglin and T. G. Shepherd. O3-N2O correlations from the Atmospheric Chemistry Experiment: Revisiting a diagnostic of transport and chemistry in the stratosphere. *Journal of Geophysical Research: Atmospheres*, 112(D19), 2007. doi: 10.1029/2006JD008281.

H. Hersbach, B. Bell, P. Berrisford, S. Hirahara, A. Horányi, J. Muñoz-Sabater, J. Nicolas, C. Peubey, R. Radu, D. Schepers, A. Simmons, C. Soci, S. Abdalla, X. Abellan, G. Balsamo, P. Bechtold, G. Biavati, J. Bidlot, M. Bonavita, G. De Chiara, P. Dahlgren, D. Dee, M. Diamantakis, R. Dragani, J. Flemming, R. Forbes, M. Fuentes, A. Geer, L. Haimberger, S. Healy, R. J. Hogan, E. Hólm, M. Janisková, S. Keeley, P. Laloyaux, P. Lopez, C. Lupu, G. Radnoti, P. de Rosnay, I. Rozum, F. Vamborg, S. Villaume, and J.-N. Thépaut. The ERA5 global reanalysis. *Quarterly Journal of the Royal Meteorological Society*, 146(730):1999–2049, 2020. doi: 10.1002/qj.3803.

L. Hoffmann, P. Konopka, J. Clemens, and B. Vogel. Lagrangian transport simulations using the extreme convection parameterization: An assessment for the ECMWF reanalyses. *Atmospheric Chemistry and Physics*, 23(13):7589–7609, July 2023. doi: 10.5194/acp-23-7589-2023.

J. R. Holton, P. H. Haynes, M. E. McIntyre, A. R. Douglass, R. B. Rood, and L. Pfister. Stratosphere-troposphere exchange. *Reviews of Geophysics*, 33(4):403–439, 1995. doi: 10.1029/95RG02097.

P. Hoor, H. Fischer, L. Lange, J. Lelieveld, and D. Brunner. Seasonal variations of a mixing layer in the lowermost stratosphere as identified by the CO-O3 correlation from in situ measurements: SEASONAL VARIATION OF CROSS-TROPOPAUSE TRANSPORT. *Journal of Geophysical Research: Atmospheres*, 107(D5):ACL 1–1–ACL 1–11, Mar. 2002. doi: 10.1029/2000JD000289.

R. Hossaini, M. P. Chipperfield, B. M. Monge-Sanz, N. A. D. Richards, E. Atlas, and D. R. Blake. Bromoform and dibromomethane in the tropics: A 3-D model study of chemistry and transport. *Atmos. Chem. Phys.*, 2010.

R. Hossaini, M. P. Chipperfield, W. Feng, T. J. Breider, E. Atlas, S. A. Montzka, B. R. Miller, F. Moore, and J. Elkins. The contribution of natural and anthropogenic very short-lived species to stratospheric bromine. *Atmospheric Chemistry and Physics*, 12 (1):371–380, 2012. ISSN 1680-7324. doi: 10.5194/acp-12-371-2012.

R. Hossaini, M. P. Chipperfield, S. A. Montzka, A. Rap, S. Dhomse, and W. Feng. Efficiency of short-lived halogens at influencing climate through depletion of stratospheric ozone. *Nature Geoscience*, 8(3):186–190, 2015. ISSN 1752-0908. doi: 10.1038/ngeo2363.

R. Hossaini, E. Atlas, S. S. Dhomse, M. P. Chipperfield, P. F. Bernath, A. M. Fernando, J. Mühle, A. A. Leeson, S. A. Montzka, W. Feng, J. J. Harrison, P. Krummel, M. K. Vollmer, S. Reimann, S. O'Doherty, D. Young, M. Maione, J. Arduini, and C. R. Lunder. Recent Trends in Stratospheric Chlorine From Very Short-Lived Substances. *Journal of Geophysical Research: Atmospheres*, 124(4):2318–2335, Feb. 2019. ISSN 2169-897X, 2169-8996. doi: 10.1029/2018JD029400.

M. Jesswein, H. Bozem, H.-C. Lachnitt, P. Hoor, T. Wagenhäuser, T. Keber, T. Schuck, and A. Engel. Comparison of inorganic chlorine in the Antarctic and Arctic lowermost stratosphere by separate late winter aircraft measurements. *Atmospheric Chemistry and Physics*, 21(23):17225–17241, Nov. 2021. doi: 10.5194/acp-21-17225-2021.

M. Jesswein, R. P. Fernandez, L. Berná, A. Saiz-Lopez, J.-U. Grooß, R. Hossaini, E. C. Apel, R. S. Hornbrook, E. L. Atlas, D. R. Blake, S. Montzka, T. Keber, T. Schuck, T. Wagenhäuser, and A. Engel. Global seasonal distribution of CH_2Br_2 and $CHBr_3$ in the upper troposphere and lower stratosphere. *Atmospheric Chemistry and Physics*, 22 (22):15049–15070, Nov. 2022. doi: 10.5194/acp-22-15049-2022.

P. Jöckel, R. Sander, A. Kerkweg, H. Tost, and J. Lelieveld. Technical Note: The Modular Earth Submodel System (MESSy) - a new approach towards Earth System Modeling. *Atmospheric Chemistry and Physics*, 5(2):433–444, Feb. 2005. doi: 10.5194/acp-5-433-2005.

M. Kajino and M. Aikawa. A model validation study of the washout/rainout contribution of sulfate and nitrate in wet deposition compared with precipitation chemistry data in Japan. *Atmospheric Environment*, 117:124–134, Sept. 2015. doi: 10.1016/j.atmosenv.2015.06.042.

T. Keber, H. Bönisch, C. Hartick, M. Hauck, F. Lefrancois, F. Obersteiner, A. Ringsdorf, N. Schohl, T. Schuck, R. Hossaini, P. Graf, P. Jöckel, and A. Engel. Bromine from short-lived source gases in the extratropical northern hemispheric upper troposphere and lower stratosphere (UTLS). *Atmospheric Chemistry and Physics*, 20(7):4105–4132, Apr. 2020. doi: 10.5194/acp-20-4105-2020.

T. K. Koenig, S. Baidar, P. Campuzano-Jost, C. A. Cuevas, B. Dix, R. P. Fernandez, H. Guo, S. R. Hall, D. Kinnison, B. A. Nault, K. Ullmann, J. L. Jimenez, A. Saiz-Lopez, and R. Volkamer. Quantitative detection of iodine in the stratosphere. *Proceedings of the National Academy of Sciences*, 117(4):1860–1866, Jan. 2020. doi: 10.1073/pnas.1916828117.

P. Konopka, H.-M. Steinhorst, J.-U. Grooß, G. Günther, R. Müller, J. W. Elkins, H.-J. Jost, E. Richard, U. Schmidt, G. Toon, and D. S. McKenna. Mixing and ozone loss in the 1999–2000 Arctic vortex: Simulations with the three-dimensional Chemical Lagrangian Model of the Stratosphere (CLaMS). *Journal of Geophysical Research: Atmospheres*, 109(D2), 2004. doi: 10.1029/2003JD003792.

P. Konopka, G. Günther, R. Müller, F. H. S. dos Santos, C. Schiller, F. Ravegnani, A. Ulanovsky, H. Schlager, C. M. Volk, S. Viciani, L. L. Pan, D.-S. McKenna, and M. Riese. Contribution of mixing to upward transport across the tropical tropopause layer (TTL). *Atmospheric Chemistry and Physics*, 7(12):3285–3308, June 2007. doi: 10.5194/acp-7-3285-2007.

P. Konopka, M. Tao, F. Ploeger, M. Diallo, and M. Riese. Tropospheric mixing and parametrization of unresolved convective updrafts as implemented in the Chemical Lagrangian Model of the Stratosphere (CLaMS v2.0). *Geoscientific Model Development*, 12(6):2441–2462, 2019. ISSN 1991-9603. doi: 10.5194/gmd-12-2441-2019.

P. Konopka, M. Tao, M. von Hobe, L. Hoffmann, C. Kloss, F. Ravegnani, C. M. Volk, V. Lauther, A. Zahn, P. Hoor, and F. Ploeger. Tropospheric transport and unresolved convection: Numerical experiments with CLaMS 2.0/MESSy. *Geoscientific Model Development*, 15(19):7471–7487, Oct. 2022. doi: 10.5194/gmd-15-7471-2022.

U. Langematz. Stratospheric ozone: Down and up through the anthropocene. *ChemTexts*, 5(2):8, June 2019. ISSN 2199-3793. doi: 10.1007/s40828-019-0082-7.

J. C. Laube, A. Engel, H. Bonisch, T. Mobius, D. R. Worton, W. T. Sturges, K. Grunow, and U. Schmidt. Contribution of very short-lived organic substances to stratospheric chlorine and bromine in the tropics – a case study. *Atmos. Chem. Phys.*, 2008.

J. C. Laube, S. Tegtmeier, Q. Liang, and M. Rigby. *WMO: Scientific Assessment of Ozone Depletion: 2022, GAW Report No. 278, Chapt. 1, World Meteorological Organization*. World Meteorological Organization, 2022.

V. Lauther, B. Vogel, J. Wintel, A. Rau, P. Hoor, V. Bense, R. Müller, and C. M. Volk. In situ observations of CH_2Cl_2 and $CHCl_3$ show efficient transport pathways for very short-lived species into the lower stratosphere via the Asian and the North American summer monsoon. *Atmospheric Chemistry and Physics*, 22(3):2049–2077, Feb. 2022. doi: 10.5194/acp-22-2049-2022.

E. C. Leedham Elvidge, C. Hughes, F. S. L. Keng, S.-M. Phang, G. Malin, and W. T. Sturges. Emission of atmospherically significant halocarbons by naturally occurring and farmed tropical macroalgae. *Biogeosciences*, 10(6):3615–3633, 2013. ISSN 1726-4170. doi: 10.5194/bg-10-3615-2013.

C. Lemmen, R. Müller, P. Konopka, and M. Dameris. Critique of the tracer-tracer correlation technique and its potential to analyze polar ozone loss in chemistry-climate models. *Journal of Geophysical Research: Atmospheres*, 111(D18), 2006. doi: 10.1029/2006JD007298.

Q. Liang, R. S. Stolarski, S. R. Kawa, J. E. Nielsen, A. R. Douglass, J. M. Rodriguez, D. R. Blake, E. L. Atlas, and L. E. Ott. Finding the missing stratospheric Br_y: A global

modeling study of $CHBr_3$ and CH_2Br_2. *Atmospheric Chemistry and Physics*, 10(5): 2269–2286, 2010. ISSN 1680-7316. doi: 10.5194/acp-10-2269-2010.

D. S. McKenna, J.-U. Grooß, G. Günther, P. Konopka, R. Müller, G. Carver, and Y. Sasano. A new Chemical Lagrangian Model of the Stratosphere (CLaMS) 2. Formulation of chemistry scheme and initialization. *Journal of Geophysical Research: Atmospheres*, 107(D15):ACH 4–1–ACH 4–14, 2002a. doi: 10.1029/2000JD000113.

D. S. McKenna, P. Konopka, J.-U. Grooß, G. Günther, R. Müller, R. Spang, D. Offermann, and Y. Orsolini. A new Chemical Lagrangian Model of the Stratosphere (CLaMS) 1. Formulation of advection and mixing. *Journal of Geophysical Research: Atmospheres*, 107(D16):ACH 15–1–ACH 15–15, 2002b. doi: 10.1029/2000JD000114.

M. Meinshausen, Z. R. J. Nicholls, J. Lewis, M. J. Gidden, E. Vogel, M. Freund, U. Beyerle, C. Gessner, A. Nauels, N. Bauer, J. G. Canadell, J. S. Daniel, A. John, P. B. Krummel, G. Luderer, N. Meinshausen, S. A. Montzka, P. J. Rayner, S. Reimann, S. J. Smith, M. van den Berg, G. J. M. Velders, M. K. Vollmer, and R. H. J. Wang. The shared socio-economic pathway (SSP) greenhouse gas concentrations and their extensions to 2500. *Geoscientific Model Development*, 13(8):3571–3605, Aug. 2020. doi: 10.5194/gmd-13-3571-2020.

K. Mohanakumar. *Stratosphere Troposphere Interactions: An Introduction*. Springer Science & Business Media, July 2008. ISBN 978-1-4020-8217-7.

S. A. Montzka, S. Reimann, A. Engel, K. Krüger, S. O'Doherty, W. T. Sturges, D. Blake, M. Dorf, P. Fraser, L. Froidevaux, K. Jucks, K. Kreher, M. J. Kurylo, A. Mellouki, J. Miller, E. Atlas, P. Bernath, T. Blumenstock, J. H. Butler, A. Butz, B. Connor, P. Duchatelet, G. Dutton, F. Hendrick, P. B. Krummel, L. J. M. Kuijpers, E. Mahieu, A. Manning, J. Mühle, K. Pfeilsticker, B. Quack, M. Ross, R. J. Salawitch, S. Schauffler, I. J. Simpson, D. Toohey, M. K. Vollmer, T. J. Wallington, H. J. R. Wang, R. F. Weiss, M. Yamabe, Y. Yokouchi, and S. Yvon-Lewis. Ozone-Depleting Substances (ODSs) and Related Chemicals. In *Scientific Assessment of Ozone Depletion: 2010*. World Meteorological Organization, 2011.

P. W. Mote, K. H. Rosenlof, M. E. McIntyre, E. S. Carr, J. C. Gille, J. R. Holton, J. S. Kinnersley, H. C. Pumphrey, J. M. Russell III, and J. W. Waters. An atmospheric tape recorder: The imprint of tropical tropopause temperatures on stratospheric water vapor. *Journal of Geophysical Research: Atmospheres*, 101(D2):3989–4006, 1996. doi: 10.1029/95JD03422.

R. Müller, P. J. Crutzen, J.-U. Grooß, C. Bürhl, J. M. Russell, H. Gernandt, D. S. McKenna, and A. F. Tuck. Severe chemical ozone loss in the Arctic during the winter of 1995–96. *Nature*, 389(6652):709–712, Oct. 1997. doi: 10.1038/39564.

T. Narayana Rao, K. N. Uma, D. Narayana Rao, and S. Fukao. Understanding the transportation process of tropospheric air entering the stratosphere from direct vertical air motion measurements over Gadanki and Kototabang. *Geophysical Research Letters*, 35(15), 2008. doi: 10.1029/2008GL034220.

M. A. Navarro, E. L. Atlas, A. Saiz-Lopez, X. Rodriguez-Lloveras, D. E. Kinnison, J.-F. Lamarque, S. Tilmes, M. Filus, N. R. P. Harris, E. Meneguz, M. J. Ashfold, A. J. Manning, C. A. Cuevas, S. M. Schauffler, and V. Donets. Airborne measurements of organic bromine compounds in the Pacific tropical tropopause layer. *Proceedings of the National Academy of Sciences*, 112(45):13789–13793, Nov. 2015. doi: 10.1073/pnas.1511463112.

J. E. Nielsen and A. R. Douglass. A simulation of bromoform's contribution to stratospheric bromine. *Journal of Geophysical Research: Atmospheres*, 106(D8):8089–8100, 2001. ISSN 2156-2202. doi: 10.1029/2000JD900767.

C. Ordóñez, J.-F. Lamarque, S. Tilmes, D. E. Kinnison, E. L. Atlas, D. R. Blake, G. Sousa Santos, G. Brasseur, and A. Saiz-Lopez. Bromine and iodine chemistry in a global chemistry-climate model: Description and evaluation of very short-lived oceanic sources. *Atmospheric Chemistry and Physics*, 12(3):1423–1447, Feb. 2012. ISSN 1680-7324. doi: 10.5194/acp-12-1423-2012.

L. L. Pan, L. C. Paulik, S. B. Honomichl, L. A. Munchak, J. Bian, H. B. Selkirk, and

H. Vömel. Identification of the tropical tropopause transition layer using the ozone-water vapor relationship. *Journal of Geophysical Research: Atmospheres*, 119(6): 3586–3599, 2014. doi: 10.1002/2013JD020558.

I. Pisso, P. H. Haynes, and K. S. Law. Emission location dependent ozone depletion potentials for very short-lived halogenated species. *Atmospheric Chemistry and Physics*, 10(24):12025–12036, 2010. ISSN 1680-7324. doi: 10.5194/acp-10-12025-2010.

F. Ploeger, P. Konopka, G. Günther, J.-U. Grooß, and R. Müller. Impact of the vertical velocity scheme on modeling transport in the tropical tropopause layer. *Journal of Geophysical Research: Atmospheres*, 115(D3), 2010. doi: 10.1029/2009JD012023.

F. Ploeger, P. Konopka, K. Walker, and M. Riese. Quantifying pollution transport from the Asian monsoon anticyclone into the lower stratosphere. *Atmospheric Chemistry and Physics*, 17(11):7055–7066, June 2017. doi: 10.5194/acp-17-7055-2017.

L. M. Polvani, M. Previdi, M. R. England, G. Chiodo, and K. L. Smith. Substantial twentieth-century Arctic warming caused by ozone-depleting substances. *Nature Climate Change*, 10(2):130–133, Feb. 2020. ISSN 1758-6798. doi: 10.1038/s41558-019-0677-4.

L. Poshyvailo. *Lagrangian Simulation of Stratospheric Water Vapour: Impact of Large-Scale Circulation and Small-Scale Transport Processes*. PhD thesis, Wuppertal University, 2020.

B. Quack and D. W. R. Wallace. Air-sea flux of bromoform: Controls, rates, and implications. *Global Biogeochemical Cycles*, 17(1), 2003. ISSN 1944-9224. doi: 10.1029/2002GB001890.

W. J. Randel, M. Park, L. Emmons, D. Kinnison, P. Bernath, K. A. Walker, C. Boone, and H. Pumphrey. Asian Monsoon Transport of Pollution to the Stratosphere. *Science*, 328 (5978):611–613, Apr. 2010. doi: 10.1126/science.1182274.

R. C. Rhew. Sources and sinks of methyl bromide and methyl chloride in the tallgrass prairie: Applying a stable isotope tracer technique over highly variable gross fluxes.

Journal of Geophysical Research: Biogeosciences, 116(G3), 2011. ISSN 2156-2202. doi: 10.1029/2011JG001704.

M. Riese, F. Ploeger, A. Rap, B. Vogel, P. Konopka, M. Dameris, and P. Forster. Impact of uncertainties in atmospheric mixing on simulated UTLS composition and related radiative effects. *Journal of Geophysical Research: Atmospheres*, 117(D16), 2012. doi: 10.1029/2012JD017751.

T. Röckmann, J.-U. Grooß, and R. Müller. The impact of anthropogenic chlorine emissions, stratospheric ozone change and chemical feedbacks on stratospheric water. *Atmospheric Chemistry and Physics*, 4(3):693–699, 2004. ISSN 1680-7316. doi: 10.5194/acp-4-693-2004.

M. K. Rotermund, V. Bense, M. P. Chipperfield, A. Engel, J.-U. Grooß, P. Hoor, T. Hüneke, T. Keber, F. Kluge, B. Schreiner, T. Schuck, B. Vogel, A. Zahn, and K. Pfeilsticker. Organic and inorganic bromine measurements around the extratropical tropopause and lowermost stratosphere: Insights into the transport pathways and total bromine. *Atmospheric Chemistry and Physics*, 21(20):15375–15407, 2021. ISSN 1680-7324. doi: 10.5194/acp-21-15375-2021.

A. Saiz-Lopez, S. Baidar, C. A. Cuevas, T. K. Koenig, R. P. Fernandez, B. Dix, D. E. Kinnison, J.-F. Lamarque, X. Rodriguez-Lloveras, T. L. Campos, and R. Volkamer. Injection of iodine to the stratosphere. *Geophysical Research Letters*, 42(16):6852–6859, 2015. ISSN 1944-8007. doi: 10.1002/2015GL064796.

R. J. Salawitch, D. K. Weisenstein, L. J. Kovalenko, C. E. Sioris, P. O. Wennberg, K. Chance, M. K. W. Ko, and C. A. McLinden. Sensitivity of ozone to bromine in the lower stratosphere. *Geophysical Research Letters*, 32(5), 2005. doi: 10.1029/2004GL021504.

M. L. Salby. *Fundamentals of Atmospheric Physics*. Elsevier, May 1996. ISBN 978-0-08-053215-8.

M. R. Sargent, J. B. Smith, D. S. Sayres, and J. G. Anderson. The roles of deep convection and extratropical mixing in the tropical tropopause layer: An in situ measurement perspective. *Journal of Geophysical Research: Atmospheres*, 119(21):12,355–12,371, 2014. doi: 10.1002/2014JD022157.

V. Sinha. *Measurement of Volatile Organic Compounds and Total Reactivity in the Atmosphere*. PhD thesis, Gutenberg University in Mainz, Mar. 2023.

B.-M. Sinnhuber and I. Folkins. Estimating the contribution of bromoform to stratospheric bromine and its relation to dehydration in the tropical tropopause layer. *Atmospheric Chemistry and Physics*, 6(12):4755–4761, Oct. 2006. doi: 10.5194/acp-6-4755-2006.

S. Solomon. Stratospheric ozone depletion: A review of concepts and history. *Reviews of Geophysics*, 37(3):275–316, 1999. ISSN 1944-9208. doi: 10.1029/1999RG900008.

X. Tang, H. Zhang, and M. Shao. *Atmospheric Environmental Chemistry*. Advanced educated publisher, 2006.

S. Tilmes, R. Müller, J.-U. Grooß, and J. M. Russell III. Ozone loss and chlorine activation in the Arctic winters 1991-2003 derived with the tracer-tracer correlations. *Atmospheric Chemistry and Physics*, 4(8):2181–2213, Nov. 2004. doi: 10.5194/acp-4-2181-2004.

B. Vogel, G. Günther, R. Müller, J.-U. Grooß, and M. Riese. Impact of different Asian source regions on the composition of the Asian monsoon anticyclone and of the extratropical lowermost stratosphere. *Atmospheric Chemistry and Physics*, 15(23):13699–13716, Dec. 2015. doi: 10.5194/acp-15-13699-2015.

C. M. Volk, J. W. Elkins, D. W. Fahey, G. S. Dutton, J. M. Gilligan, M. Loewenstein, J. R. Podolske, K. R. Chan, and M. R. Gunson. Evaluation of source gas lifetimes from stratospheric observations. *Journal of Geophysical Research: Atmospheres*, 102 (D21):25543–25564, 1997. doi: 10.1029/97JD02215.

T. Wagenhäuser, M. Jesswein, T. Keber, T. Schuck, and A. Engel. Mean age from observations in the lowermost stratosphere: An improved method and interhemispheric

differences. *Atmospheric Chemistry and Physics*, 23(7):3887–3903, Apr. 2023. doi: 10.5194/acp-23-3887-2023.

S. Wang, D. Kinnison, S. A. Montzka, E. C. Apel, R. S. Hornbrook, A. J. Hills, D. R. Blake, B. Barletta, S. Meinardi, C. Sweeney, F. Moore, M. Long, A. Saiz-Lopez, R. P. Fernandez, S. Tilmes, L. K. Emmons, and J.-F. Lamarque. Ocean Biogeochemistry Control on the Marine Emissions of Brominated Very Short-Lived Ozone-Depleting Substances: A Machine-Learning Approach. *Journal of Geophysical Research: Atmospheres*, 124 (22):12319–12339, 2019. ISSN 2169-897X, 2169-8996. doi: 10.1029/2019JD031288.

N. J. Warwick, J. A. Pyle, G. D. Carver, X. Yang, N. H. Savage, F. M. O'Connor, and R. A. Cox. Global modeling of biogenic bromocarbons. *Journal of Geophysical Research*, 111(D24):D24305, 2006. ISSN 0148-0227. doi: 10.1029/2006JD007264.

Y. Yokouchi, T. Saito, and H. Mukai. Long-term high-frequency measurements of dibromomethane in the atmosphere at algae-rich and algae-poor coastal sites. *Journal of Atmospheric Chemistry*, 75(2):171–180, 2018. ISSN 1573-0662. doi: 10.1007/s10874-017-9370-z.

F. Ziska, B. Quack, K. Abrahamsson, S. D. Archer, E. Atlas, T. Bell, J. H. Butler, L. J. Carpenter, C. E. Jones, N. R. P. Harris, H. Hepach, K. G. Heumann, C. Hughes, J. Kuss, K. Krüger, P. Liss, R. M. Moore, A. Orlikowska, S. Raimund, C. E. Reeves, W. Reifenhäuser, A. D. Robinson, C. Schall, T. Tanhua, S. Tegtmeier, S. Turner, L. Wang, D. Wallace, J. Williams, H. Yamamoto, S. Yvon-Lewis, and Y. Yokouchi. Global sea-to-air flux climatology for bromoform, dibromomethane and methyl iodide. *Atmospheric Chemistry and Physics*, 13(17):8915–8934, 2013. ISSN 1680-7324. doi: 10.5194/acp-13-8915-2013.

Appendix A

Incorporated washout reactions

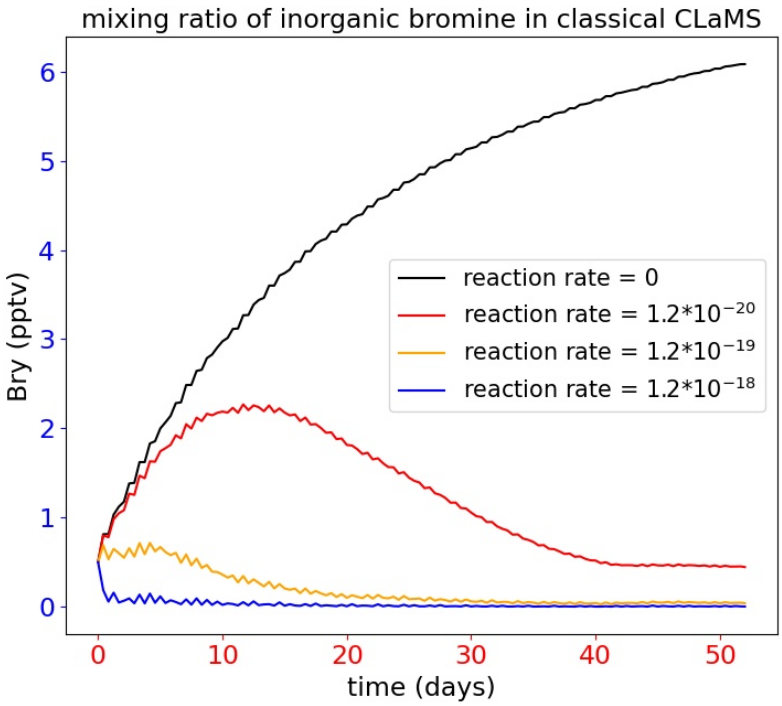

Figure A.1: Mixing ratios of inorganic bromine (Br_y^{inorg}) in the CLaMS box model simulation, with varying reaction rate coefficients for HBr scavenging reactions (described in Section 5.1), as a function of time.

Appendix B

Surface origin tracers contribution in MESSy CLaMS 1.0

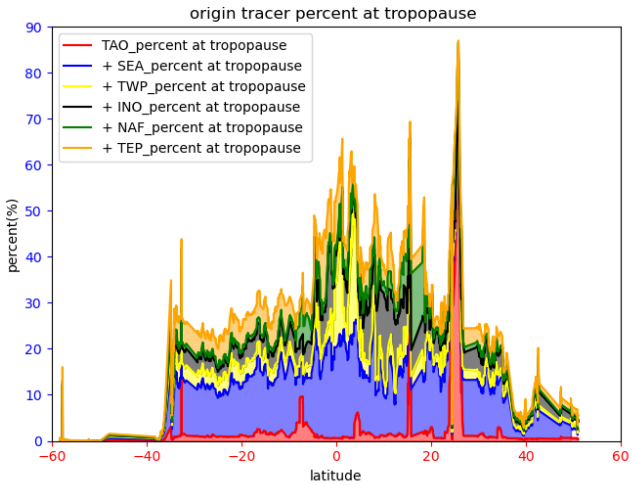

Figure B.1: The accumulation of the abundant contributed percentages from different emission sources at different latitudes for the first transfer flight near the tropopause region (340-360K) in CLaMS 1.0 model. Different colors represent different emission tracers.

Note: the region Southeastern Asia (SEA) include warm pool, which is different with label SEA in 6.5. The Tropical Western Pacific (TWP) is also different with that in 6.5.

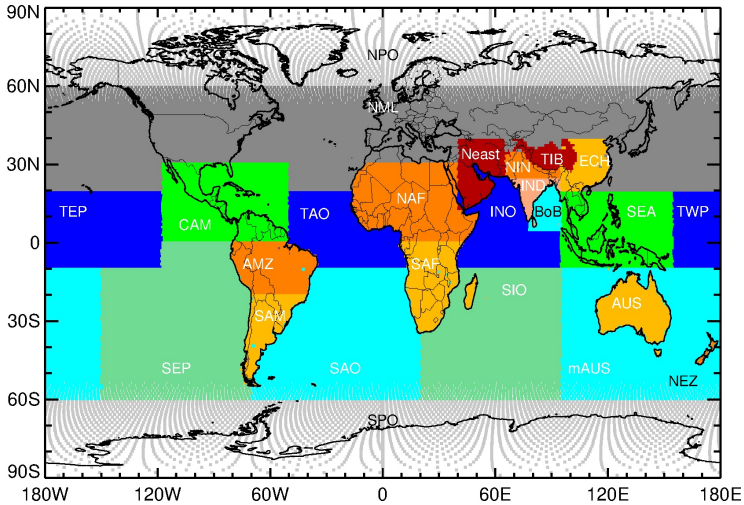

Figure B.2: Global geographical regions of lower boundary emission sources in CLaMS 1.0 model simulation.

Appendix C

Seasonal lower boundary map adapted from climatology

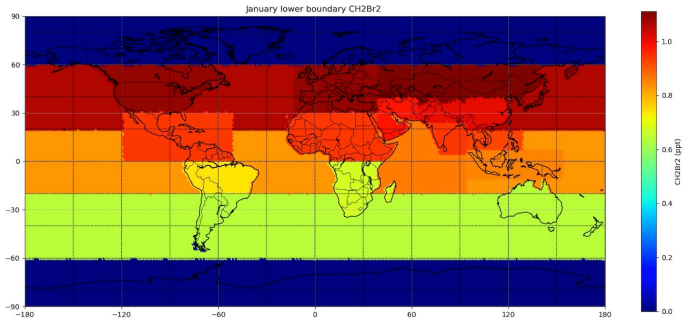

(a) January to March for CH_2Br_2

Figure C.1: CH_2Br_2 lower boundary maps of different seasons

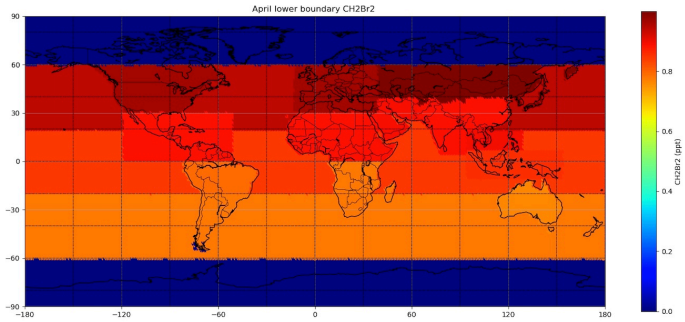

(b) April for CH_2Br_2

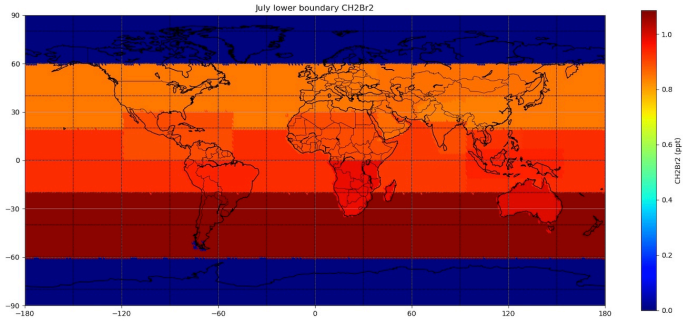

(c) July CH_2Br_2

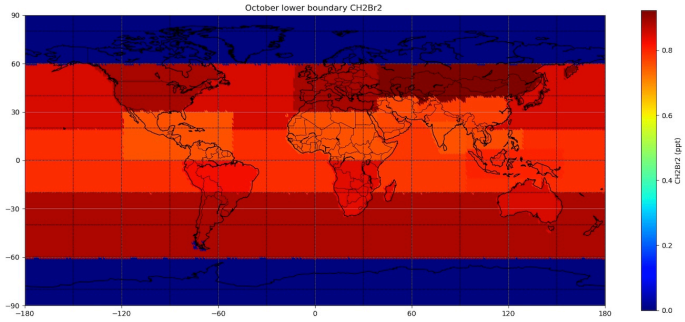

(d) October CH_2Br_2

Figure C.1: (Cont.)

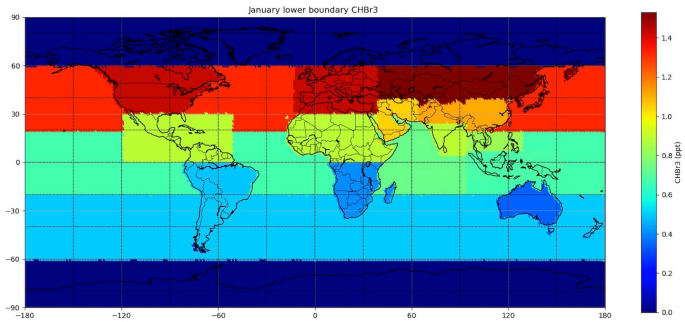

(a) January $CHBr_3$

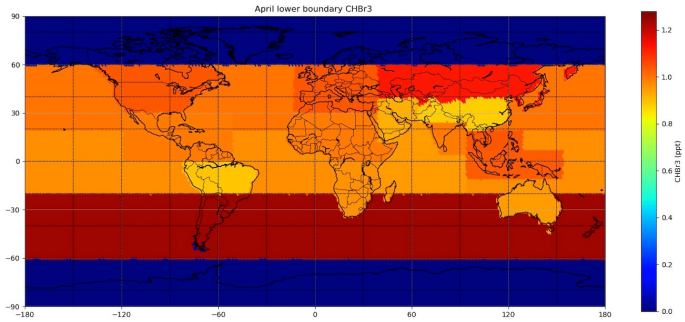

(b) April $CHBr_3$

Figure C.2: $CHBr_3$ lower boundary maps of different seasons

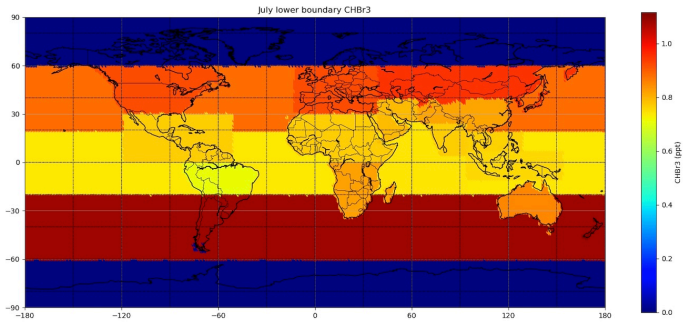

(c) July $CHBr_3$

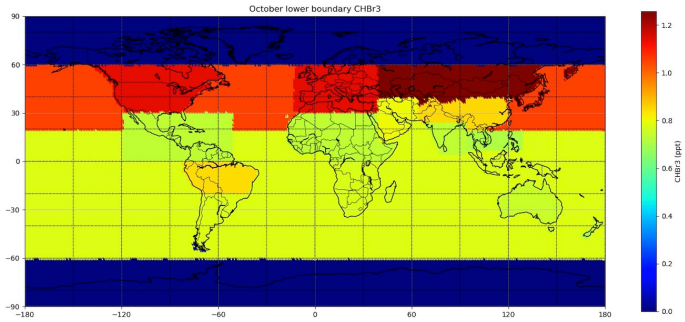

(d) October $CHBr_3$

Figure C.2: (Cont.)

Appendix D

Distribution of air parcels at lower boundary in different months

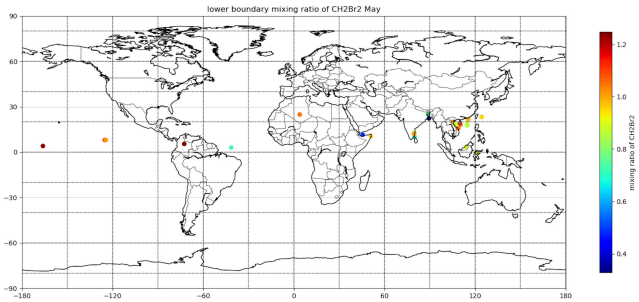

(a) CH_2Br_2 May

Figure D.1: The traced back air parcels for CH_2Br_2 at lower boundary in different months.

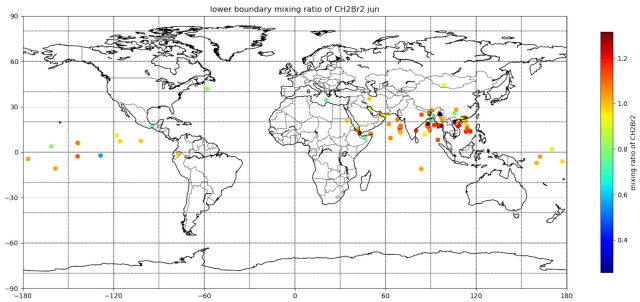

(b) CH_2Br_2 Jun

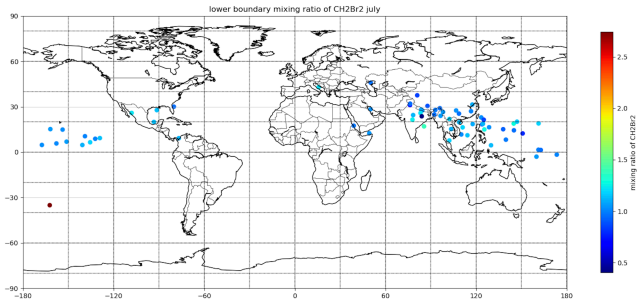

(c) CH_2Br_2 July

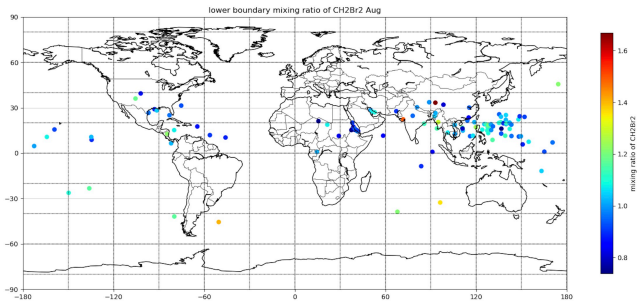

(d) CH_2Br_2 Aug

Figure D.1: (Cont.)

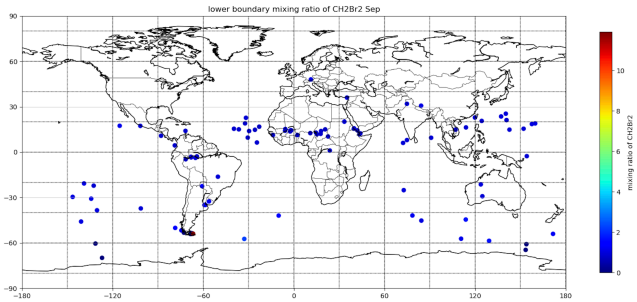

(e) CH_2Br_2 Sep

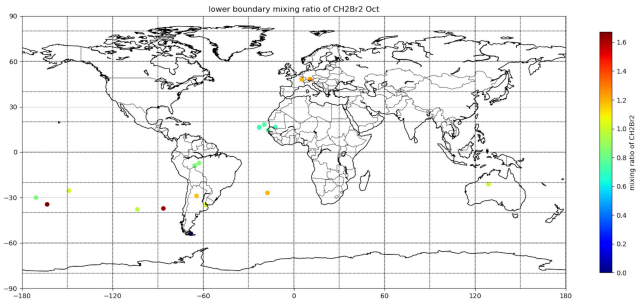

(f) CH_2Br_2 Oct

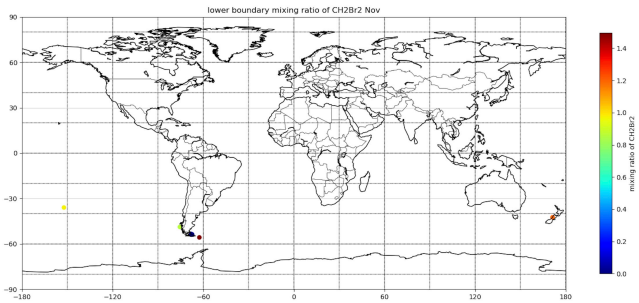

(g) CH_2Br_2 Nov

Figure D.1: (Cont.)

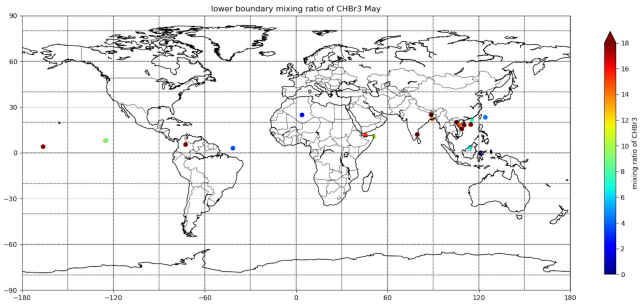

(a) $CHBr_3$ May

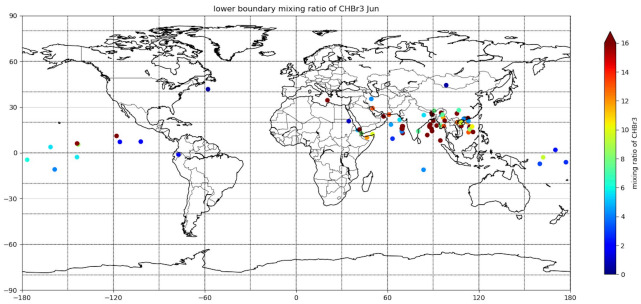

(b) $CHBr_3$ Jun

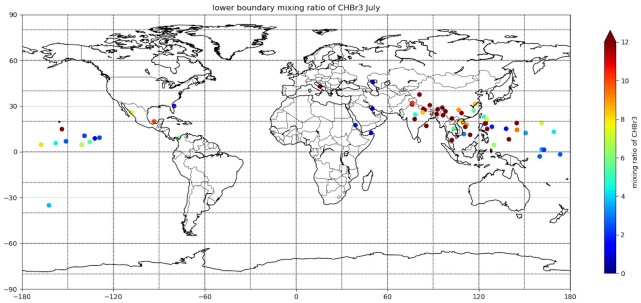

(c) $CHBr_3$ July

Figure D.2: The traced back air parcels for $CHBr_3$ at lower boundary in different months.

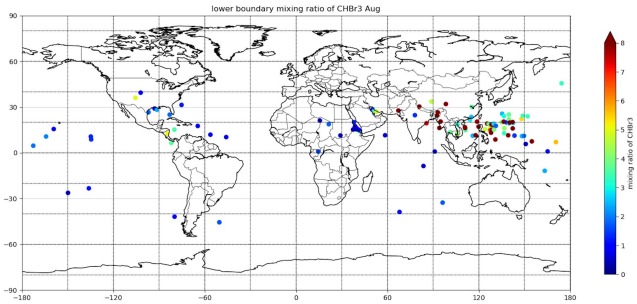

(d) $CHBr_3$ Aug

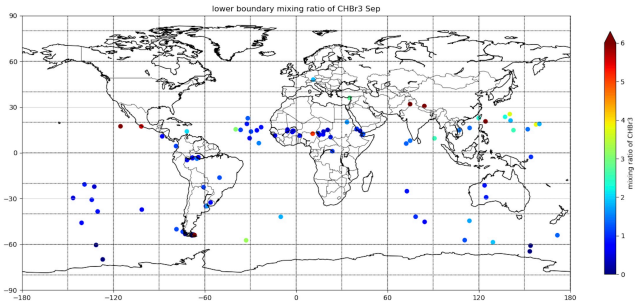

(e) $CHBr_3$ Sep

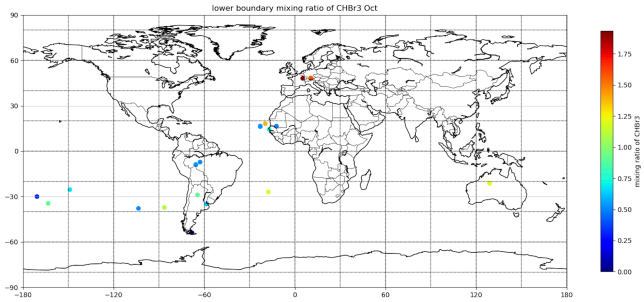

(f) $CHBr_3$ Oct

Figure D.2: (Cont.)

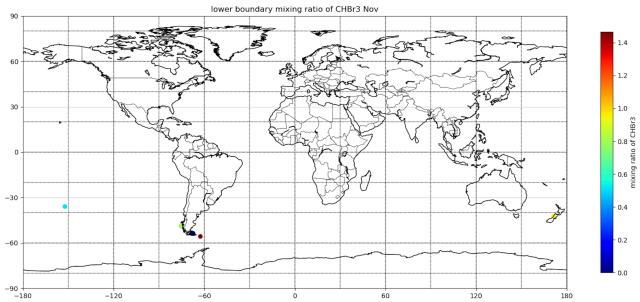

(g) $CHBr_3$ Nov

Figure D.2: (Cont.)

Appendix E

Monthly dependent regionally resolved lower boundary maps

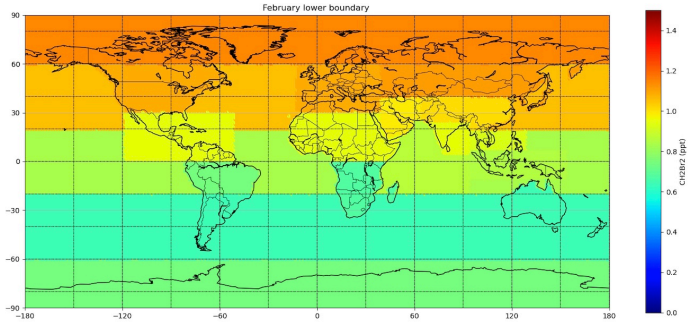

(a) CH_2Br_2 from January to March

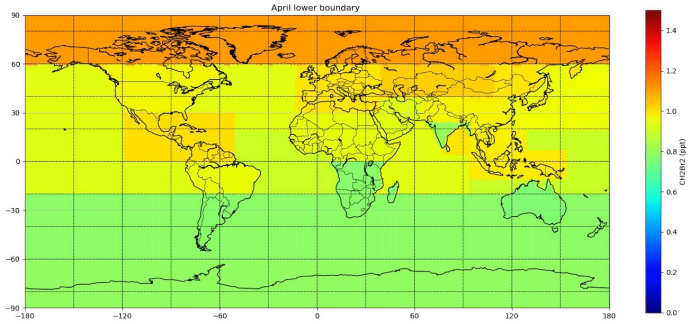

(b) CH_2Br_2 in April

Figure E.1: Global maps of monthly dependent lower boundary mixing ratios (ppt) for dibromomethane (CH_2Br_2) from January to December (**a** to **J**).

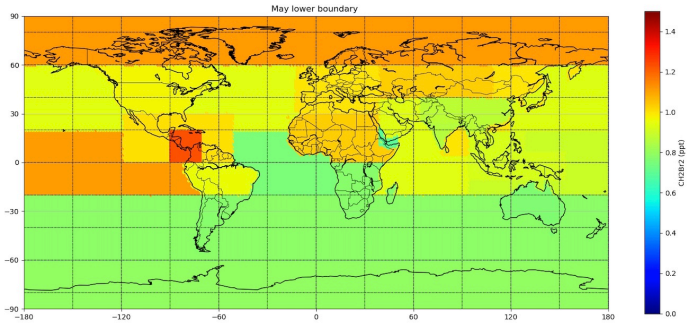

(c) CH_2Br_2 in May

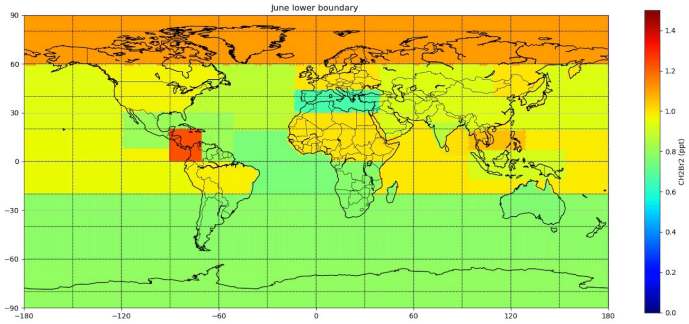

(d) CH_2Br_2 in June

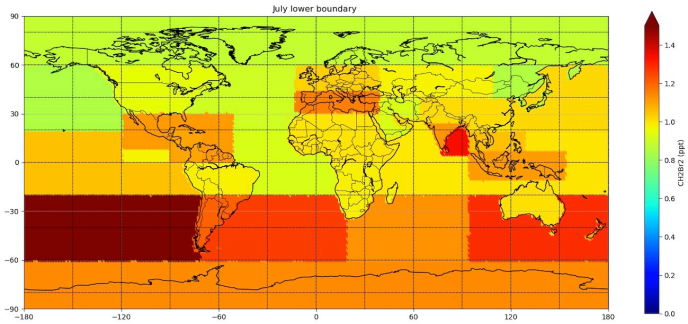

(e) CH_2Br_2 in July

Figure E.1: (Cont.)

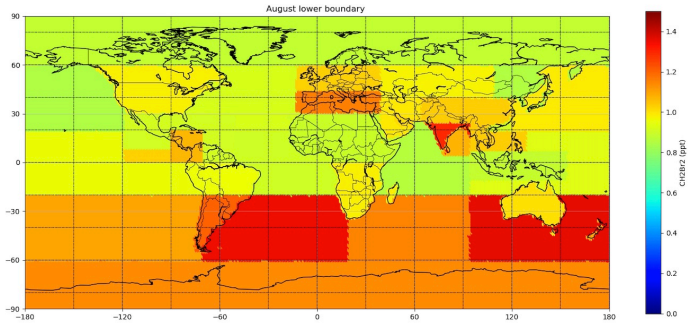

(f) CH_2Br_2 in August

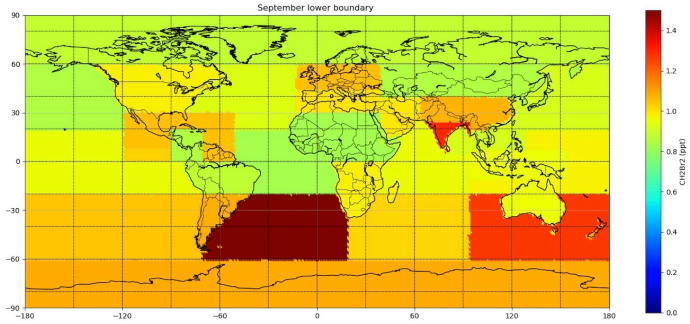

(g) CH_2Br_2 in September

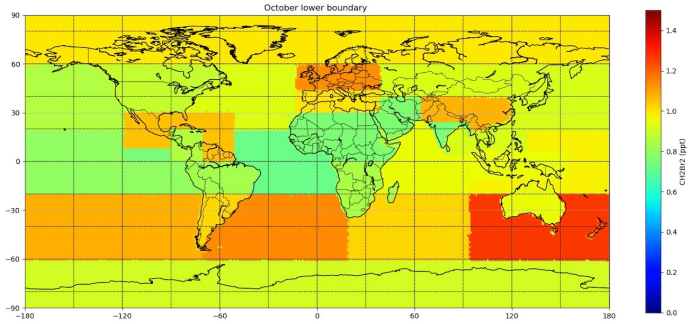

(h) CH_2Br_2 in October

Figure E.1: (Cont.)

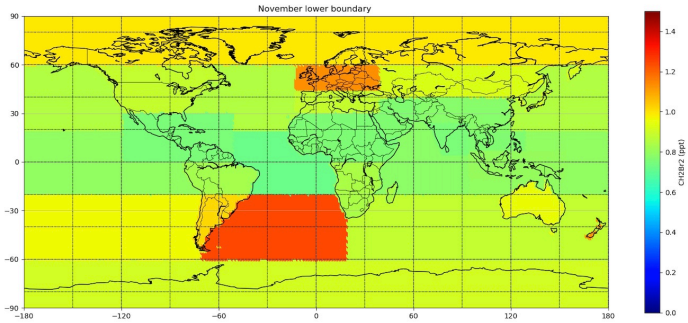

(i) CH_2Br_2 in November

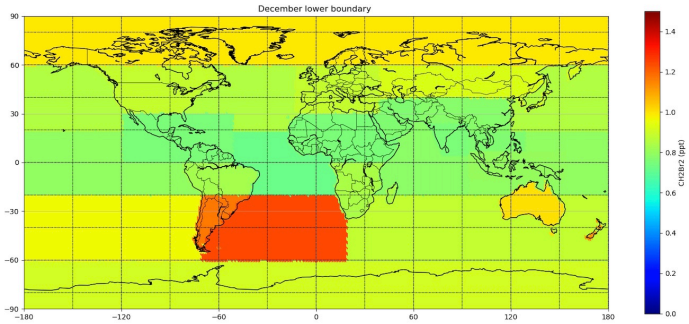

(j) CH_2Br_2 in December

Figure E.1: (Cont.)

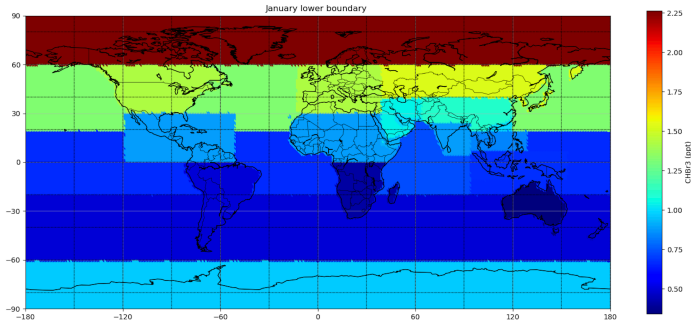

(a) CHBr3 from January to March

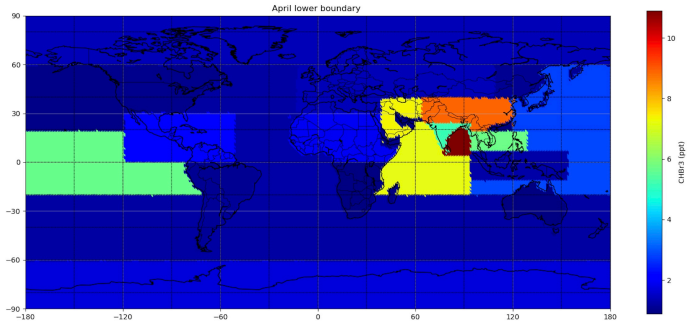

(b) CHBr3 in April

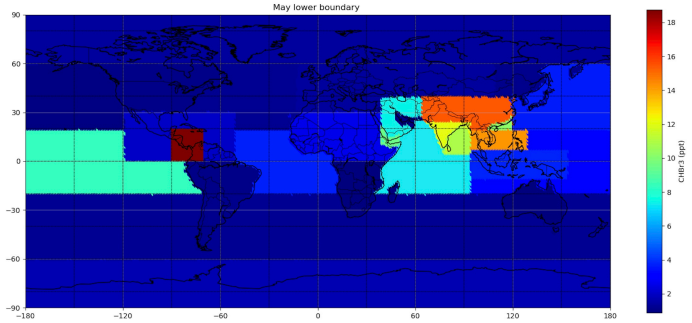

(c) CHBr3 in May

Figure E.2: Global maps of monthly dependent lower boundary mixing ratios (ppt) for bromoform (CHBr3) from January to December (**a** to **J**). The scale of the color bars is different in the different months. Specifically, in May and June, the scale of mixing ratio is above 18 ppt and 16 ppt, respectively.

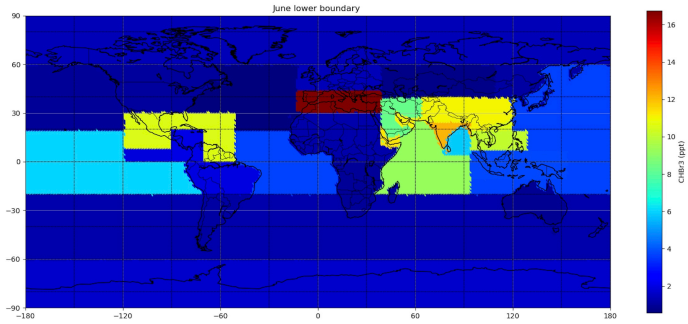

(d) $CHBr_3$ in June

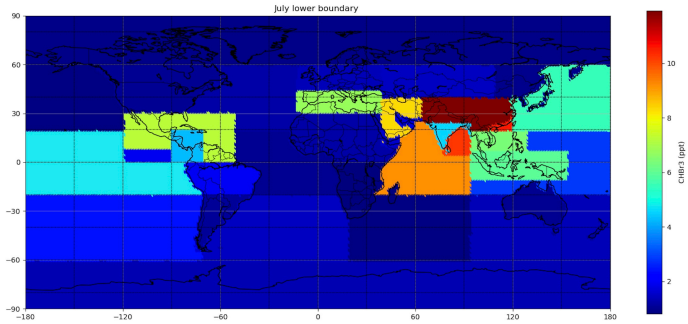

(e) $CHBr_3$ in July

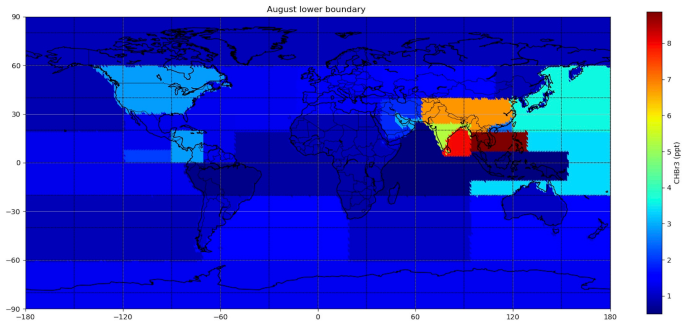

(f) $CHBr_3$ in August

Figure E.2: (Cont.)

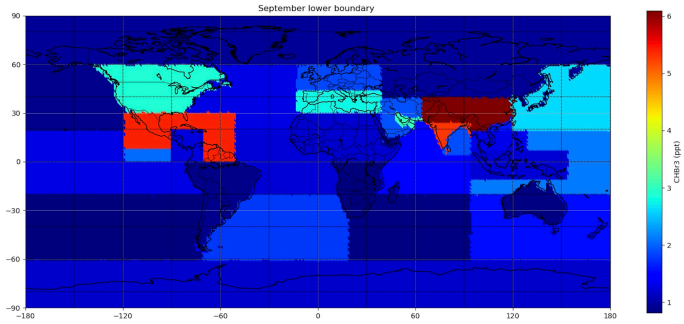

(g) $CHBr_3$ in September

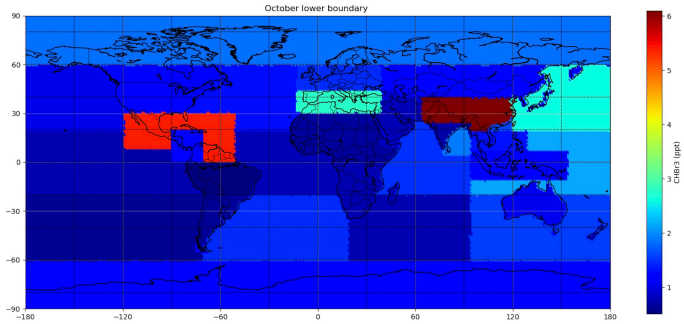

(h) $CHBr_3$ in October

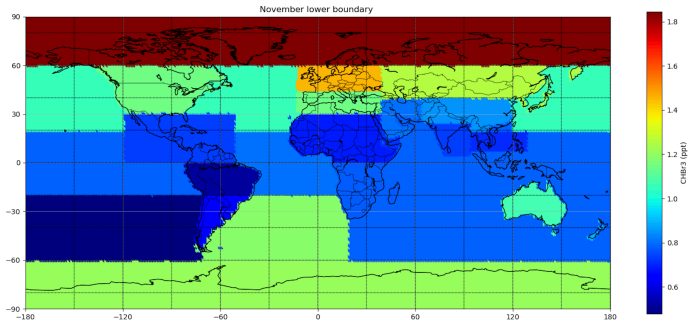

(i) $CHBr_3$ in November

Figure E.2: (Cont.)

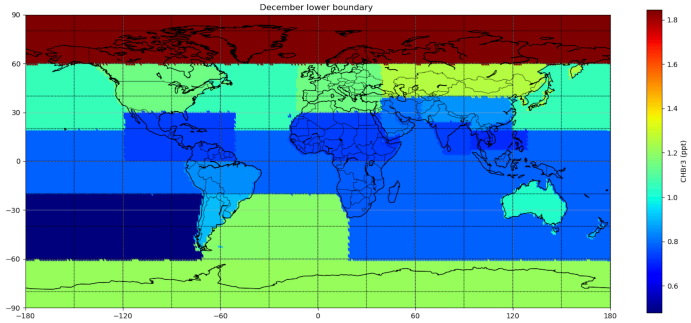

(j) $CHBr_3$ in December

Figure E.2: (Cont.)

Appendix F

Comparison with altitude-latitude cross section between climatology data and simulation with a zonally symmetric seasonal lower boundary

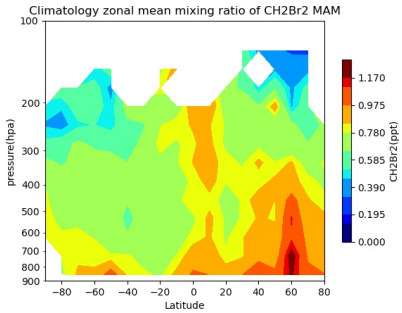

(a) observations in MAM

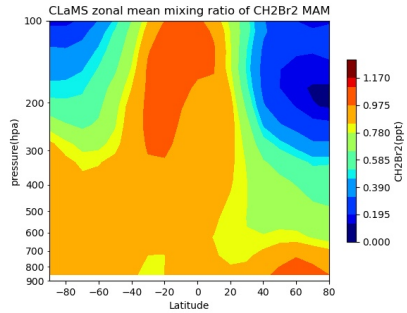

(b) simulations in MAM

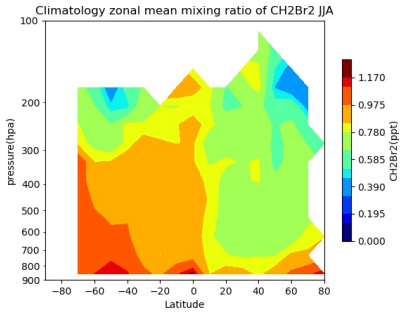

(c) observations in JJA

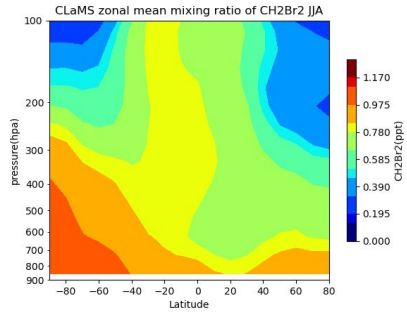

(d) simulations in JJA

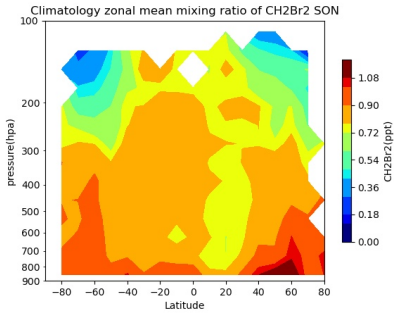

(e) observations in SON

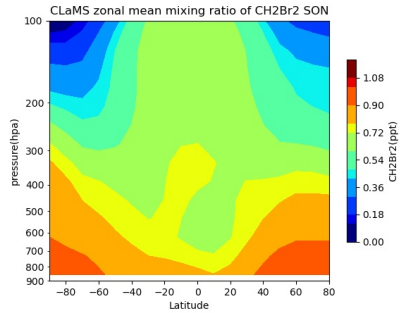

(f) simulations in SON

Figure F.1: Altitude-latitude cross section of CH_2Br_2. The data are separated by three seasons (MAM (March, April, May); JJA (June, July, August); SON (September, October, November)) as a function of latitude and pressure. The left column (**a**, **c** and **e**) show observational climatology data. The right column (**b**, **d** and **f**) show model results of CLaMS 2.0 version with zonally symmetric seasonal lower boundary.

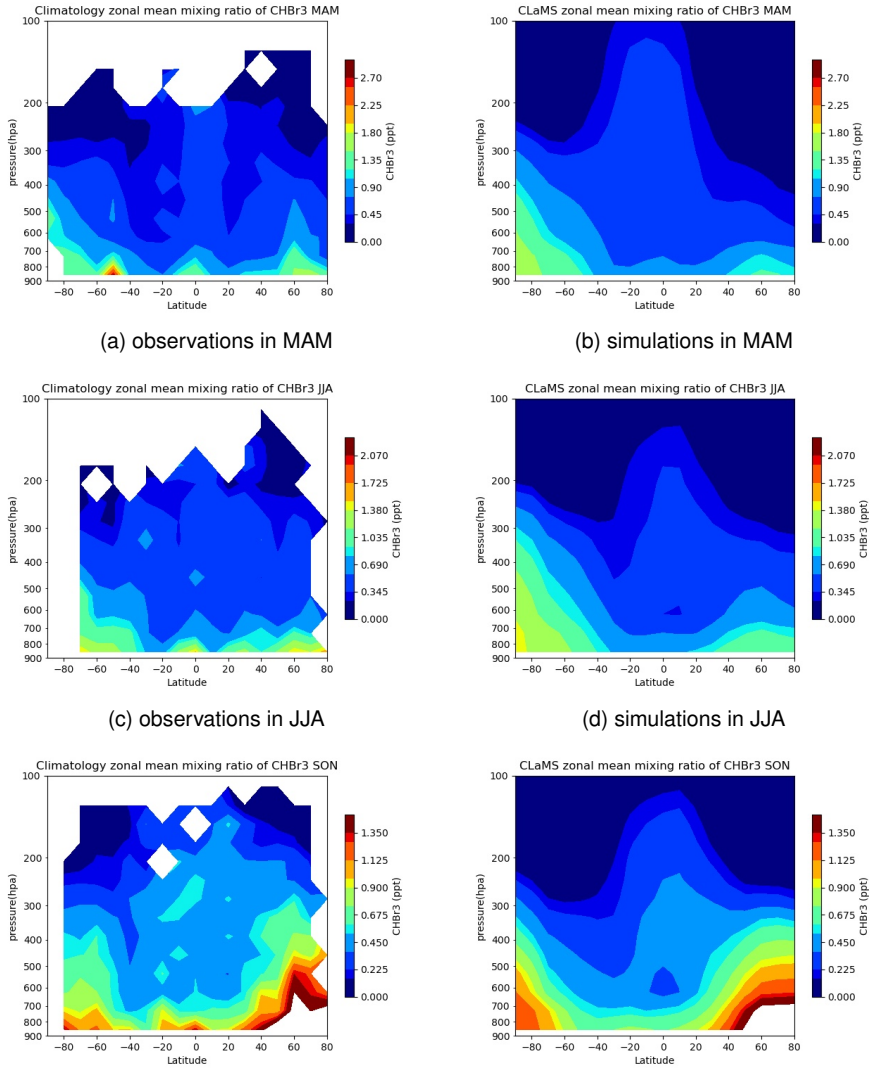

(a) observations in MAM

(b) simulations in MAM

(c) observations in JJA

(d) simulations in JJA

(e) observations in SON

(f) simulations in SON

Figure F.2: Altitude-latitude cross section of $CHBr_3$. The data are separated by three seasons (MAM (March, April, May); JJA (June, July, August); SON (September, October, November)) as a function of latitude and pressure. The left column (**a**, **c** and **e**) show observational climatology data. The right column (**b**, **d** and **f**) show model results of CLaMS 2.0 version with zonally symmetric seasonal lower boundary.

Acknowledgments

Foremost, I would like to express my gratitude to Prof. Dr. Martin Riese, Prof. Dr. Michaela Imelda Hegglin, Dr. Rolf Müller, Dr. Jens-Uwe Grooß and Dr. Bärbel Vogel for providing me with the opportunity to embark on and complete my doctoral journey at the IEK-7 institute. Additionally, I am thankful for the support from the SCI-HI project, which not only allowed me to advance my scientific career in Germany but also provided a rich cultural experience.

A special note of thanks goes to P.D. Dr. Paul Konopka, Dr. Bärbel Vogel, and Dr. Johannes Laube for engaging scientific discussions and invaluable assistance. I also extend my appreciation to Nicole Thomas for her consistent technical support throughout my work with CLaMS and to Verena Alishahi for her patience in addressing my technical queries.

Particularly, my deepest gratitude goes to my scientific advisor, Dr. Jens-uwe Grooß, whose patient guidance, extensive knowledge, and motivational support have not only acquainted me with model simulation but have been indispensable in interpreting the results. Without his help and guidance, this work would not have been possible. I am equally grateful to my Ph.D. supervisor, Dr. Rolf Müller, for his remarkable support and valuable advice, both in scientific and personal matters. I aspire to approach my future work with the same enthusiasm, sincerity, and creativity demonstrated by Jens-Uwe and Rolf.

A special mention to my office mate, Dr. Gebhard Günther, for his assistance with technical issues and for sharing interesting insights about life. I extend my thanks to colleagues in the same project, Dr. Meike Rotermund and Markus Jesswein, for their

contributions to engaging group discussions and providing support with observational data.

In addition, my gratitude extends to the entire IEK-7 team and colleagues. It has been a pleasure meeting each one of you, sharing delightful lunches, and enjoying relaxing coffee breaks. Being part of IEK-7 has filled me with pride, and the collective efforts of the institute's individuals have made my time in Jülich intellectually stimulating and emotionally memorable. I extend my appreciation to the members of my thesis committee, Dr. Rolf Müller, Prof. Dr. Felix Plöger, Prof. Dr. Thorsten Benter, and Dr. Jens-Uwe Grooß, for their proofreading and thoughtful reviews.

Special thanks to my family, relatives and all the friends for their unwavering support and understanding during the challenging phases of this academic journey. Their encouragement has been a constant source of strength. To everyone who contributed to this endeavor, thank you sincerely for your invaluable support.

Band / Volume 625
On a multi-spectral method for measuring aerosol properties, suitable for operation on iagos passenger aircraft
P. Weber (2024), ca 123 pp
ISBN: 978-3-95806-746-2

Band / Volume 626
Modellierung der flächendifferenzierten Grundwasserneubildung für Schleswig-Holstein
Endbericht
I. McNamara, B. Tetzlaff, T. Wolters, F. Wendland (2024), 96 pp
ISBN: 978-3-95806-748-6

Band / Volume 627
Modeling orographic gravity waves from source to termination to improve parameterization schemes in climate models
S. Rhode (2024), xii, ii, 138 pp
ISBN: 978-3-95806-750-9

Band / Volume 628
Abscheidung kolumnarer Wärmedämmschichten mittels Suspensionsplasmaspritzen (SPS) und Plasma Spray – Physical Vapor Deposition (PS-PVD) Prozess
J. Joeris (2024), vii, 133 pp
ISBN: 978-3-95806-752-3

Band / Volume 629
Structure and properties of electrochemical interfaces from first principles simulations
R. Tesch (2024), xvi, 161 pp
ISBN: 978-3-95806-753-0

Band / Volume 630
Elucidation of Barocaloric Effect in Spin Crossover Compounds
H. Shahed (2024), x, 261 pp
ISBN: 978-3-95806-758-5

Band / Volume 631
Computational Investigation of Solvation Phenomena at Metal-Electrolyte Interfaces
O. Cheong (2024), xvii, 142 pp
ISBN: 978-3-95806-759-2

Band / Volume 632
Senkung zukünftiger Stickoxid- und Partikelemissionen in Nordrhein-Westfalen durch den Einsatz alternativer Energieträger und Antriebe
J. L. Breuer (2024), vii, 339 pp
ISBN: 978-3-95806-760-8

Band / Volume 633
Development of Model-Based Correction Methods for Temperature-Dependent Electromagnetic Induction (EMI) Measurement Errors in Soil Conductivity Estimations
T. M. Tchantcho Amin (2024), xx, 100 pp
ISBN: 978-3-95806-761-5

Band / Volume 634
Investigation and implementation of improved and degradation-tolerant fuel electrodes for solid oxide cells
A. Schwiers (2024), VI, 163, XIII pp
ISBN: 978-3-95806-762-2

Band / Volume 635
In Situ Time Calibration for Stationary Multichannel GPR Monitoring Systems
L. Steinbeck (2024), xvi, 98, xxxi pp
ISBN: 978-3-95806-767-7

Band / Volume 636
Erneuerbares Methanol als Ausgangsstoff für die Bereitstellung von flüssigen Kraftstoffen für den Transportsektor
F. Schorn (2024), VI, 275 pp
ISBN: 978-3-95806-769-1

Band / Volume 637
Investigation of Lower Boundary Conditions of Brominated Very Short-lived Species (VSLS)
S. Zheng (2024), 2, iii, 160 pp
ISBN: 978-3-95806-770-7

Weitere ***Schriften des Verlags im Forschungszentrum Jülich*** unter
http://wwwzb1.fz-juelich.de/verlagextern1/index.asp

Energie & Umwelt / Energy & Environment
Band / Volume 637
ISBN 978-3-95806-770-7

Mitglied der Helmholtz-Gemeinschaft

JÜLICH
Forschungszentrum